

# **Applications of Chalcogen bonding**

by

**Thomas Fellowes**

ORCID: 0000-0002-6389-6049

A thesis submitted in total fulfillment for the  
degree of Doctor of Philosophy

in the  
Faculty of Science  
School of Chemistry and Bio21 Institute  
**THE UNIVERSITY OF MELBOURNE**

December 2020



# **Contents**



# **List of Figures**



# **List of Tables**



# Abbreviations

**LAH** List Abbreviations Here



# Constants

Speed of Light  $c = 2.997\,924\,58 \times 10^8 \text{ ms}^{-1}$  (exact)



# Symbols

$a$  distance m  
 $P$  power W (Js<sup>-1</sup>)

$\omega$  angular frequency rads<sup>-1</sup>



# Chapter 1

## Introduction

The importance of non-bonding interactions in our world simply cannot be overstated. While we may think of the more familiar covalent and ionic bonds as the core of chemistry, more often than not it is non-bonding interactions that dictate the nature of substances, from bulk properties such as tensile strength, to microscopic phenomena like protein-ligand interactions.

At a fundamental level, all non-bonding interactions (indeed, conventional bonding too) are attributable to the electrostatic force. However, it is more convenient to broadly categorise interactions based on strength and structural motifs that are common to each class. Such classes include dispersion forces, dipole-dipole interactions, and H-bonding. In the 19th century, it became apparent that these classes paint an incomplete picture of intermolecular bonding. As part of their investigation into solvent effects on the colour of iodine solutions in 1949, Bensei and Hildebrand invoked the concept of “charge-transfer” complexes to explain the association of molecular iodine with nucleophilic solvent molecules.<sup>Benesi1949</sup> Although the electrophilic nature of molecular halogens was already well appreciated with respect to reactivity, this appears to be the first acknowledgement that this understanding could be applied to ground state complexes. In support of this, Hassel and Hvolslef elucidated the structure of a 1:1 complex of molecular bromine and 1,4-dioxane in 1954, and observed an unusually strong interaction between the two molecules.<sup>Hassel1954</sup> The crystal was comprised of long chains of monomers (figure [Figure 1.1](#)), exhibiting a very short O...Br contact (2.71Å, the sum of the VDW radii is 3.37Å), and a slightly lengthened Br-Br bond (2.31Å vs 2.28Å in gaseous bromine).

In the subsequent years, a wide variety of names and labels were applied to the “charge-transfer” phenomenon, including “lock and key”, “donor-acceptor”, and “filling of antibonding orbitals”, as summarised in Bent’s excellent 1968 review.<sup>Bent1968</sup> The term “halogen bonding” (X-bonding) only gained widespread acceptance in 1983 after the publication of the review of Dumas, Gomel,

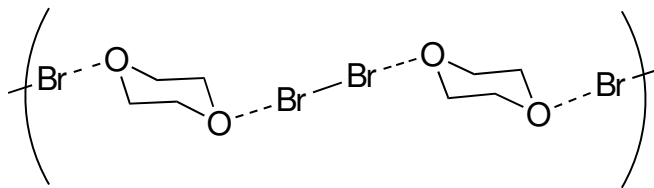


FIGURE 1.1: Long chains of molecular bromine and 1,4-dioxane, observed by Hassel and Hvoslef.

and Guerin.<sup>Dumas1983</sup> The term deliberately evokes similarity to the better known concept of hydrogen bonding, as the two phenomena are of comparable strength and, importantly, directionality. In 1998 Anthony C. Legon again used the term to describe the attractive interaction between halogens and Lewis bases in prereactive complexes, harking back to the original understanding of electrophilic halogens as a primarily reactive phenomenon.<sup>Legon1998, Legon1999</sup> In the following years, the potential of X-bonding was more fully recognised, with applications in supramolecular chemistry and self-assembly,<sup>Corradi2000, Metrangolo2008, Priimagi2013</sup> catalysis and bond activation,<sup>Walter2011, Soloshonok2017, Takagi2017</sup> and molecular sensing and recognition.<sup>Cornes2017, VargasJentzsch2013, Borissov2017</sup>

From X-bonding grew the related concepts of chalcogen (Ch-), pnicogen (Pn-), and tetrel bonding (T-bonding), as the electrophilic nature of these elements was discovered.<sup>Murray2007</sup> Similar applications have also been found for these classes of noncovalent interactions, Ch-bonding in particular.<sup>Fanfrlik2014, Garrett2016, Ho2016, Wonner2017, Mitchell2017, Benz2017, Biot2017, Ho2017</sup>

## 1.1 Chalcogen Bonding

Ch-bonding is the attractive interaction between a Lewis base and a chalcogen atom bearing an electron withdrawing substituent. The terminology of Ch-bonding partners is perhaps counterintuitive, as donors and acceptors are named by analogy with H-bonded equivalents. Note this is contrary to the formal flow of electron density; Ch-bond *donors* bear vacant *acceptor* orbitals, while Ch-bond *acceptors* are *donors* of electron density. For the purposes of this report, “donor” will refer to the Lewis acidic chalcogen species.

### 1.1.1 Mechanisms

As was briefly discussed in the introduction, all intermolecular (and indeed *intramolecular*) forces are manifestations of the electromagnetic force. Nonetheless, it is more convenient to categorise energetic contributions to any given interaction as orbital, electrostatic, or dispersion mediated, as there are marked differences in strength and directionality between

them. Historically, X- and Ch-bond interactions were understood to be primarily due to orbital overlap and resulting charge transfer. Evidence for this included the lengthening of the X-X bond corresponding to increased occupation of the  $\sigma^*$ (X-X) orbital due to the incoming lone pair (this was observed in Hassel and Hvoslef's original work<sup>Hassel1954</sup>). Characteristic charge transfer bands are also observed in the UV-vis spectra of halogen solutions.<sup>Blackstock1987</sup>

Such evidence of orbital contributions is not, however, common to all systems displaying X- or Ch-bond interactions. The iodoperfluoroalkanes and arenes studied by Resnati et al show no charge transfer bands in UV-vis spectra, yet are exceptionally strong X-bond donors.<sup>Yan2014</sup> Jane Murray and Peter Politzer have advocated for an alternative, primarily electrostatic explanation of X- and Ch-bond interactions.<sup>Murray2008, Murray2009</sup> They propose that a positively charged  $\sigma$ -hole is generated along the extension of a  $\sigma$  bond to an electron withdrawing substituent, due to polarisation of the bonding orbital. This also adequately explains the strength and directionality of these interactions.

An interpretation which has not attracted as much attention is that of dispersion forces.

While the varying contributions from each of these factors can be dissected computationally via perturbation methods, experimental evidence is surprisingly sparse. Pascoe, Ling and Cockroft, however, devised an elegant experiment to quantitatively determine energetic contributions.<sup>Pascoe2017</sup>  $^{19}\text{F}$  NMR was used to determine the relative populations of two conformors of a "molecular balance", one bearing a Ch-bond interaction, one not. Interaction energies were thus derived, and found to be more or less invariant with respect to the solvent. This appeared to rule out electrostatic contributions, as solvent dipole moment and bulk polarisability would otherwise have a large effect on the position of the equilibrium. These results also suggest that dispersion plays only a minor role, for similar reasons.

DFT was used to further probe the dispersion contribution. Free energies were calculated using functionals which both did, and did not include dispersion corrections, and the values compared to the experimental results. The non-dispersion corrected B3LYP functional gave superior correlation with experiment than did either M06-2X and  $\omega\text{B97-D}$ , both of which include dispersion. This provided additional evidence that, in the systems studied, the major contributor to the interaction is orbital overlap and charge transfer.

Although current evidence points towards these interactions being primarily orbital related, the electrostatic " $\sigma$ -hole" terminology of Politzer and Murray has stuck, and the term is now used to encompass the whole gamut of X- Ch- Pn- and T-bonding interactions.

## 1.2 Applications of Ch-Bonding

Ch-bonding, and by extension, all  $\sigma$ -hole interactions can theoretically be applied to any formal Lewis acid-base system. They are especially attractive as a *hydrophobic* complement to H-bonding interactions, which are generally considered to be *hydrophilic*. The following are brief summaries of existing applications in the literature.

### 1.2.1 Materials

The major applications of  $\sigma$ -hole interactions have so far been in the realm of crystal engineering. Early work by Corradi et al showed that halogen bonding was able to outcompete H-bonding in the formation of supramolecular architectures.<sup>Corradi2000</sup> A review by Metrangolo summarised the forms that are accessible using X-bonding to direct crystal growth.<sup>Metrangolo2008</sup> 1D, 2D, and 3D architectures are able to be generated using appropriate X-bond donors, and these show potential in the design of liquid crystals, organic semiconductors and paramagnetic materials. A more recent review by the same group described applications in anion transport, and luminescent and photoresponsive crystals.<sup>Priimagi2013</sup> The group of Stefan Matile has further explored anion transport, and has published a review comparing X-bonding with other hydrophobic interactions such as anion- $\pi$  and anion-macrodipole interactions.<sup>VargasJentzsch2013</sup>

Ch-bonding, too, has been investigated with respect to materials chemistry. Fanfrlik et al demonstrated the importance of Ch-bonding on the crystal packing of thiaboranes.<sup>Fanfrlik2014</sup> They found that the sulfur-based  $\sigma$ -hole was sufficiently strong to interact with the weakly basic  $\pi$  electrons of a phenyl group, with contacts as short as 3.2Å being observed.

In 2016, Ho et al published their work into tellurium-based Ch-bonding.<sup>Ho2016</sup> Their scaffolds are based on an iso-tellurazole N-oxide, which reversibly forms macrocyclic structures that persist in both gas and solution phase. The macrocycles were found to coordinate  $\text{Pd}_2^+$ . This is particularly interesting, as the tellurium atoms are simultaneously behaving as a Lewis acid and base. The authors point out that such soft macrocycles are quite rare, and their work could facilitate further studies of transition metals in a soft coordination environment. They went on to investigate benzo-fused derivatives of iso-tellurazoles, as well as selenium analogues, which crystallised to form macromolecular pores and voids.<sup>Ho2017</sup>

The Taylor group has been active in the development of X- and Ch-bonding molecular sensors. Early work demonstrated that X-bonding tridentate ligands (reminiscent of enterobactin) showed moderate selectivity for  $\text{Cl}^-$ .<sup>Dimitrijevic2010</sup> They later developed bidentate Ch-bonding ligands which exhibited a tenfold increase in association constant with respect to chloride.<sup>Garrett2015a, Garrett2016</sup>

Similar results have been achieved by the Beer group, who have developed X-bonding sensors for the perrhenate anion.<sup>Cornes2017</sup> These sensors are based on functionalised cyclodextrins, and are even more sensitive than the corresponding H-bonding analogues. The group has also used iodotriazole scaffolds to chelate anions.<sup>Borissov2017</sup> Incorporation of a chiral binaphthol moiety was shown to differentiate between enantiomers of chiral anions.

The role of selenium-based Ch-bonding on the crystal structure and mechanism of the drug ebselen was demonstrated by Thomas et al.<sup>Thomas2015</sup> Interestingly, the Lewis acidity of the  $\sigma$ -hole was invoked as an explanation of the antioxidant properties of the drug.

### 1.2.2 Catalysis and bond activation

In 2008, halogen bonding was first applied to a Hantzsch ester reduction of a quinoline derivative.<sup>Bruckmann2008</sup> This reaction is well characterised and understood, and has been catalyzed with a variety of Brønsted and Lewis acids. The X-bond donors chosen were perfluoroiodoalkanes, and high conversions were achieved with modest catalyst loadings of 10%.

In 2011, a modified Ritter reaction was devised wherein benzhydryl bromide was activated by a dicationic imidazolium-based X-bond donor to give the carbocation intermediate, which was then captured by acetonitrile and then hydrolysed to afford the amide product.<sup>Walter2011</sup> This pioneering work was limited by the necessity of stoichiometric amounts of the X-bond donor, as it is consumed in the course of the reaction.

A similar alkylation of 1-chloroisochroman was achieved by the same group using a neutral perfluoroiodoarene X-bond donor in catalytic quantities.<sup>Knipe2013</sup> The proposed mechanism is similar to the thiourea-catalysed reaction of Reisman, Doyle, and Jacobsen,<sup>Reisman2008</sup> which has shown promise in asymmetric induction. The authors noted issues with solubility of the perfluoroiodoarene catalysts, which is expected of such highly fluorinated compounds.

These reactions have all been repeated with Ch-bond donors in place of X-bonds.

The quinoline reduction was successfully catalysed by a dithiophene system by Benz et al. in 2017,<sup>Benz2017</sup> and then again by the same group with a benzodiselenazole.<sup>Benz2017a</sup> With the increased selectivity and strength of the Se-based Ch-bonding catalyst compared to the X-bonding perfluoroiodoalkane, the authors were able to reduce the catalyst loading to 1%.

Wonner et al developed a selenated bisbenzimidazolium Ch-bonding catalyst for the alkylation of 1-chloroisochroman, and solvolysis of benzhydryl bromide.<sup>Wonner2017, Wonner2017a</sup> Although the best results were observed with the dicationic catalysts, conversion was also achieved with a neutral bisbenzimidazole catalyst, providing further evidence that the catalytic Lewis-acid site is indeed the  $\sigma$ -hole. For a given row in the periodic table (i.e. comparing a Se-based donor

to a Br-based donor), Ch-bonding appeared to give superior results to X-bonding, as measured by % yield.

An unusual manifestation of X-bonding is in the self-disproportionation of enantiomers, as reported by Terada et al.<sup>Soloshonok2017</sup> They observed spontaneous enrichment of one enantiomer of mebroqualone upon chromatography using an achiral solid phase, which they attributed to the formation of diasteromeric X-bonded oligomers. This phenomenon has been observed in compounds capable of interacting through H-bonding or strong dipole-dipole interactions.

### 1.2.3 Biological systems

#### 1.2.3.1 Proteins

While we usually think of the tertiary structure of proteins as being dominated by H-bonding and hydrophobic effects, there is increasing evidence that Ch-bonding plays an important role as well. This is not unexpected, as sulfur, a component of both cysteine and methionine, is known to form Ch-bonds in small molecules. In the early days of Ch-bonding interactions (2001, before the name had come into common use) Iwaoka et al published an analysis of 604 protein structures in the Protein Data Bank (PDB).<sup>Iwaoka2001</sup>

A remarkable number of close contacts (sum of Van der Waals radii plus 0.5Å) between sulfur and Lewis basic (X) atoms were identified in the structures, with 33% of cysteine residues and 22% of methionine residues showing a close contact. Furthermore, the geometric parameters of these contacts were studied, with more than half of all contacts having a S–S–X (X=O,N) of 150–180°. The observed contacts were ascribed to a  $\pi(\text{C}=\text{O}) \rightarrow \sigma^*(\text{S}-\text{S})$  interaction, in contrast to the  $n(X) \rightarrow \sigma^*(\text{S}-\text{X})$  interaction which dominates in small molecules. Also contrary to the case of small molecules, the authors suggest that the orbital component of the interaction is small, though important for establishing the directionality of the interaction. Dispersion appears to be the major stabilising force, as optimization using a non-dispersion corrected level of theory gave unrealistically large distances.

The differences between Ch-bonding in proteins and small molecules is likely due to variation in orbital energies in the functional groups which are found in each class. While small molecule Ch-bond donors are characterised by easily accessible, low energy  $\sigma^*(\text{Ch}-\text{X})$  orbitals, these are simply not found in proteins. Instead, donors are characterised by  $\sigma^*(\text{S}-\text{S})$  or  $\sigma^*(\text{S}-\text{C})$  orbitals, which are much higher in energy and less accessible to acceptors. Ch-bond acceptors, too, are markedly different between small molecules and proteins. In general, the HOMO of a system (the most Lewis basic site) is dominated by lone pairs. This is observed in most small molecules, as they form Ch-bonds through these lone pairs. However, the amide bond, which

is ubiquitous in proteins, shows an unusual inversion in orbital energies. The  $\pi(\text{C}=\text{O})$  orbital is elevated with respect to the lone pair according to MP2 calculations, making it the more basic site. Structural data supports this assertion, as the Ch-bond donor usually approaches the top of the C=O bond in proteins, rather than the usual approach towards the oxygen lone pair.<sup>Iwaoka2012</sup>

It is worth noting that selenium is also found in proteins as selenocysteine and selenomethionine. This would be expected to be an even stronger Ch-bond donor. However, selenoproteins are relatively few in number, precluding such extensive statistical analysis.<sup>Iwaoka2015</sup> They are only mentioned here for the sake of completeness.

*Intramolecular* interactions are just one instance of Ch-bonding in biological systems. Proteins often interact with ligands or substrates through H-bonds, so it is reasonable to propose that Ch-bonding could be applied in this field as well. Indeed, a protein-ligand Ch- and X-bonding interaction was used to target the gatekeeper methionine (MET146) residue of c-Jun N-terminal kinase 3 (JNK3) in a model study by Lange et al.<sup>Lange2015</sup> In this work, a protein→ligand Ch-bond was used to stabilise the interaction. Inhibition of a cysteine protease using a variety of sulfur-containing heterocyclic ligands was also investigated.<sup>Giroud2017</sup> These ligands formed ligand→protein Ch-bonds, complementary to the work by Lange. Non-conventional protein-ligand interactions are summarised in a comprehensive review by Beno et al.<sup>Beno2015</sup>

### 1.2.3.2 Nucleic acids

Nucleic acids represent another application of Ch-bonding in biology. In addition to their crucial role in the storage of genetic information, they have also been investigated as a structural material in nanotechnology. The ubiquity of H-bonds in nucleic acid complexes suggests that  $\sigma$ -hole interactions may also be used to direct formation of these complexes. X-bonding was indeed able to be used to direct formation of a Holliday junction between two DNA strands.<sup>Voth2007</sup> The authors estimated that the X-bonding interaction (mediated through a bromo-substituent) was 2–5 kcal/mol stronger than the corresponding H-bond. A 2017 review identified a further 21 X-bonded nucleic acid structures.<sup>Kolar2017</sup> This, however, appears to be the extent of research on  $\sigma$ -hole interactions with nucleic acids, which is surprising given the attractiveness of nucleic acids as drug targets, and the rich Lewis basic sites exposed through the major and minor grooves.



# **Chapter 2**

## **Experimental methods**

**2.1 General synthesis**

**2.2 Nuclear magnetic resonance**

**2.3 Mass spectrometry**

**2.4 UV-vis spectroscopy**

**2.5 X-ray diffraction**

**2.5.1 Charge density refinement**



## Chapter 3

# Simulating chalcogen bonding using molecular mechanics: A pseudoatom approach to model ebselen.

### 3.1 Introduction

Ebselen (**1**) is a molecule that has piqued the interest of many medicinal chemists, in no small part due to its decidedly non-druglike appearance. First synthesized in 1924, its unusual properties went more or less uninvestigated for more than 50 years.<sup>Lesser1924</sup> Interest in ebselen boomed in the early 1980s, and since then it has been the subject of several studies into its synthesis, biological properties, and metabolism.<sup>Weber1976, Renson1981, Muller1984, Wendel1984, Parnham1984, Engman1989, Schewe1990, Mugesh2000, Parnham1987, Kil2007, Singh2013, Azad2014, Parnham2000, Chantadul2020</sup> Very recently it was identified as a compound of interest for the treatment of COVID-19, showing promising inhibition of the viral M<sup>pro</sup> protease enzyme.<sup>Jin2020</sup> Its biological activity can be broadly attributed to its ability to neutralize reactive oxygen species (ROS), reducing the level of oxidative stress to which cells are subjected.<sup>Mugesh2000</sup> To this end, ebselen has been investigated for its neuroprotective, mood-stabilizing, anti-inflammatory, and anti-cancer properties.<sup>Parnham1987, Kil2007, Singh2013, Azad2014, Parnham2000, Chantadul2020</sup> Very recently it was identified as a compound of interest for the treatment of COVID-19, showing promising inhibition of the viral M<sup>pro</sup> protease enzyme.<sup>Jin2020</sup>

The *in vivo* antioxidant ability of ebselen is believed to be mediated through a catalytic cycle analogous to that of glutathione peroxidase (a selenoenzyme).<sup>Antony2011</sup> The selenium-containing heterocycle is reductively opened to afford the free selenol **1a**, which is the active

catalyst. This is rapidly oxidised by ROS to a selenenic acid **2**, which is then reduced back to **1a** by glutathione (GSH) via a selenenyl sulfide **3**. Its activity against a number of other targets appears to also be mediated through formation of a covalent complex via nucleophilic attack at the selenium. There is also evidence that ebselen interacts with targets non-covalently.<sup>Jin2020</sup> These interactions may include association with aromatic or hydrophobic residues, or H-bonding through the carbonyl. Ebselen can also form non-covalent complexes with Lewis bases through an electrophilic  $\sigma$ -hole on the selenium atom, similarly to electron-deficient sulfur-containing molecules.<sup>Thomas2015, Fellowes2019, Beno2015</sup>

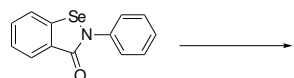


FIGURE 3.1: Catalytic cycle of ebselen *in vivo*.

Molecular modelling is a vital tool in drug development, allowing for rapid and broad-reaching screening of drug candidates against likely substrates at minimal cost and risk. *Ab initio* quantum methods (QM) are widely used to model small molecules (generally smaller than a few hundred atoms), where their accuracy and ability to describe quantum effects underlying photochemical properties and bond breaking/formation processes are critical. They are however, computationally costly. Molecular mechanics (MM), where systems are treated strictly classically, is a viable alternative for large systems. The drawbacks are that MM relies on having an extensive parameter set (a “force field”) to describe the system (which is not necessarily available, or applicable to the system at hand), and that descriptions of quantum effects often fail spectacularly.

Both of these issues are encountered when attempting to model ebselen using MM. Firstly, parameters to describe selenium-containing small molecules are simply not available in most popular force fields, including GAFF, Gromos, and CGenFF. This has been substantially addressed in the work of Torsello *et al*, where extensive parametrization of a series of diaryl diselenides and diaryl ditellurides was performed, and they provided a methodology to extend this to general chalcogen-containing molecules.<sup>Torsello2016</sup> They did not, however, address the second issue of quantum effects, which is reasonable given that they do not play a large role in diselenides. The chemistry of ebselen, on the other hand, is dominated by the  $\sigma$ -hole, which is a quantum effect.<sup>Thomas2015</sup> The  $\sigma$ -hole is a region of positive electrostatic potential situated opposite to the Se–N bond, caused by a strongly anisotropic electron distribution around the selenium atom. This causes the selenium to adopt a highly directional electrophilic character,

which can lead to the formation of “chalcogen-bonds” with electron pair donors (named by analogy to the ubiquitous hydrogen bond).<sup>Murray2009</sup>

The presence of a  $\sigma$ -hole is not a new problem in MM, nor are they exclusive to chalcogens, as they are also found on the heavier halogens, where they give rise to halogen bonding.<sup>Clark2007</sup> Perhaps due to the higher prevalence of halogens in drug-like molecules, a number of approaches have been proposed to account for  $\sigma$ -holes in halogenated molecules. The common theme in these methods is the inclusion of a pseudoatom with positive electrostatic potential attached to the halogen atom. This pseudoatom is variously called an extra point (EP), explicit  $\sigma$ -hole (ESH), or virtual or off-atom centered point, and the approaches differ in the location of the pseudoatom and method used to derive its charge.<sup>Renidine2011, Ibrahim2011, Hobza2012, Harder2016</sup> Lone pairs can also be described using negatively charged pseudoatoms, and this approach has been used for some time.<sup>Dixon1997, Cieplak2001, Harder2016</sup>

It is worth noting an alternative approach, used by Cozzolino and Vargas-Baca, which treats secondary bonding interactions as true bonds, with an explicitly parametrized potential.<sup>Cozzolino2011</sup> This was used to parametrize the supramolecular synthon 1,2,5-telluradizazole, which is known to self assemble into a range of interesting structures. This approach, however, relies on describing the bond using an *anharmonic* potential, which is not easily implemented in AMBER.

The inability to model ebselen in biological systems is a major hurdle in understanding the mechanism of its action. In this work we develop a parameter set for the selenium atom in ebselen, including a pseudoatom to simulate the  $\sigma$ -hole. This work is implemented in AMBER, due to its popularity, speed, and robustness, although there is no reason these parameters could not be extended to other force fields. We also restrict ourselves to the “vanilla” feature set of AMBER, given that advanced features such as polarizable force fields are not widely used in the analysis of ligand-receptor systems. We then show that this model accurately reproduces experimental geometries and energies, and compares favourably to *ab initio* calculations. This force field will prove useful in understanding the interactions between ebselen and current targets, and possibly lead to the discovery of new targets.

## 3.2 Results and Discussion

We began by deriving the classical bonding parameters involving selenium in ebselen, using the procedure of Torsello.<sup>Torsello2016</sup> All quantum calculations were performed using Gaussian09, unless otherwise specified.<sup>Gaussian09</sup> Electrostatic potentials were calculated using the cubegen program in the Gaussian suite, or mol2cub (<https://github.com/tjfellowes/mol2cub>). The ground state geometry of ebselen was optimized at the  $\omega$ B97X-D/def2TZVP level, followed by

vibrational analysis to confirm the structure was minimized. Chai2008, Weigend2005, Weigend2006 Partial charges were assigned to the atoms using the RESP scheme, at the HF/6-31G\* level. Cornell1993 This was chosen for consistency with existing AMBER force fields.

### 3.2.1 Classical bonding parameters

Bond and angle force constants were derived by conducting a relaxed potential energy surface scan over a range of  $\pm 0.3 \text{ \AA}$  for bonds and  $\pm 10^\circ$  for angles. The resulting data was truncated to within 5 kcal/mol of the equilibrium energy (at larger distances the surfaces were appreciably anharmonic), and this surface was fitted with a classical harmonic oscillator model (equation 3.1) using the `nls` function in the R software package.<sup>R</sup> The equilibrium distance/angle  $x_0$  was fixed to the value from the optimized geometry. Torsion angles were similarly scanned at the DFT and MM (with the torsion term set to zero) levels, and the difference between these surfaces was fitted using a periodic series truncated to the fourth order (equation 3.2). An unrealistically high torsion barrier was identified in the central Se–N–C<sub>ar</sub>–C<sub>ar</sub> dihedral, due to a repulsive short-range interaction between the aromatic hydrogen and carbonyl oxygen. We were unable to correct for this in the periodic series describing the torsion, so the non-bonding parameter for the oxygen was reduced to ??. This did not appear to have any negative impact on interactions involving this oxygen, while improving the overall structural model. The resulting parameters are presented in tables Table 3.1 and Table 3.2.

$$V(x) = \frac{1}{2}k(x - x_0)^2 \quad (3.1)$$

$$V(\phi) = \sum_{n=1}^4 \left( \frac{V_{\max,n}}{2} \times (1 + \cos(n\phi + \gamma_n)) \right) \quad (3.2)$$

TABLE 3.1: Classical parameters for ebselen. Bond lengths are given in Å, and angles in degrees. Force constants are given in kcal/mol·Å<sup>2</sup> or kcal/mol·radian<sup>2</sup>.

Parameter	$x_0$	$k$
r(Se–N)	1.8586	434.67
r(Se–C)	1.8829	422.33
$\angle$ (C–Se–N)	86.6	610.7
$\angle$ (Se–N–C <sub>ar</sub> )	119.6	182.7
$\angle$ (Se–N–C <sub>CO</sub> )	115.8	404.5
$\angle$ (C–C–Se)	119.4	329.2

Values of 2.12 and 0.2910 for the Lennard-Jones parameters  $\sigma$  and  $\varepsilon$  were used for selenium. The default GAFF Lennard-Jones parameters for the carbonyl oxygen were found to give an

TABLE 3.2: Dihedral parameters for ebselen. NEEDS REVISION

Parameter	$V_{\max,2}$ kcal/mol	$V_{\max,4}$ kcal/mol	$V_{\max,6}$ kcal/mol	$V_{\max,8}$ kcal/mol	$\gamma_2$ °	$\gamma_4$ °	$\gamma_6$ °	$\gamma_8$ °
$\phi(\text{C}_{\text{ar}}-\text{C}_{\text{ar}}-\text{N}-\text{Se})$	-0.0862	0.7841	0.0363	0.0424	180	0	0	0

unreasonably high barrier to rotation about the central dihedral angle (due to steric repulsion between the oxygen and the aryl hydrogen), so they were changed to 1.25 and 0.2.

Default GAFF values were used for all other atoms, and Lorentz/Berthelot mixing rules were used to derive cross-terms.

### 3.2.2 Energy decomposition analysis

While attempting to model the  $\sigma$ -hole using molecular mechanics, we must remember that we are forcing a classical treatment onto an inherently quantum phenomenon. That said, some parts of the quantum phenomenon are easier than others to treat classically. There are thought to be three attractive energetic components which contribute to a  $\sigma$ -hole interaction. Namely, electrostatics, induction, and dispersion.<sup>Bleiholder2006, Bleiholder2007, Pascoe2017</sup> The magnitudes of each component of  $\sigma$ -hole interactions has been the subject of heated debate in recent years. For many applications, these disagreements are fairly philosophical and of little consequence, however this is not the case when attempting to model  $\sigma$ -hole interactions using MM.

The electrostatic component generally refers to the interaction between two static (not distorted by each other) electric fields, which can be graphically represented by visualizing the electrostatic potential surfaces of the donor and acceptor moieties (figure [Figure 3.4](#)). This is already treated in MM (for the case of atom centered charges) as a sum of pairwise interactions. The accuracy of this component is only limited by the resolution of the electrostatic potential; it would appear that a pseudoatom approach could thus adequately describe the  $\sigma$ -hole. Dispersion is accounted for empirically within the  $r^{-6}$  term of the Lennard-Jones potential.

Issues arise when attempting to model the induction component of the  $\sigma$ -hole  $E_{\text{ind}}$ . This component refers to the redistribution of charge within (polarization) or between (charge-transfer) the donor and acceptor as they approach each other. Movement of charge is simply not accounted for within the most common AMBER force fields. This presents a large problem, as charge-transfer drives the strong directionality of  $\sigma$ -hole interactions, and may account for a significant proportion of their strength.

To ensure that this is not an insurmountable problem for this parametrization, we conducted energy decomposition analyses (EDA) on a variety of complexes containing ebselen. There are numerous EDA schemes available such as KM-EDA, NEDA, and ALMO, however we chose to

use symmetry-adapted perturbation theory (SAPT).<sup>SAPT2020, Jeziorski1994</sup> In contrast to several other schemes, SAPT explicitly includes dispersion (as opposed to adding it as an empirical correction), and contains no physically meaningless “catch-all” energy term. The total interaction energy  $E_{\text{tot}}$  is decomposed into an electrostatic component  $E_{\text{elst}}$ , an inductive component  $E_{\text{ind}}$  (this incorporates polarization and charge transfer, as they are not distinct phenomena within the SAPT framework), and a dispersive component  $E_{\text{dis}}$ . These attractive forces are balanced by a repulsive exchange component  $E_{\text{exch}}$ .

Four Lewis bases were chosen which are representative of those likely to be encountered in biological systems, and which span a wide range of basicity. Their structures are given in figure Figure 3.2. SAPT(DFT) analyses were conducted using the Psi4 software package on geometries optimized at the  $\omega$ B97X-D/def2TZVP level, and the results are shown in figure Figure 3.3.<sup>Parrish2017</sup>

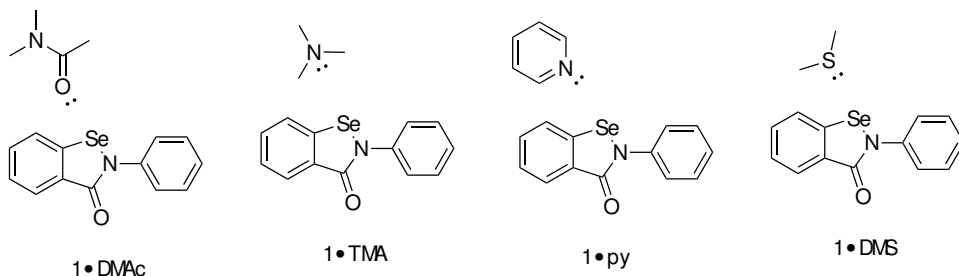


FIGURE 3.2: Structures of complexes used for SAPT(DFT) analysis.

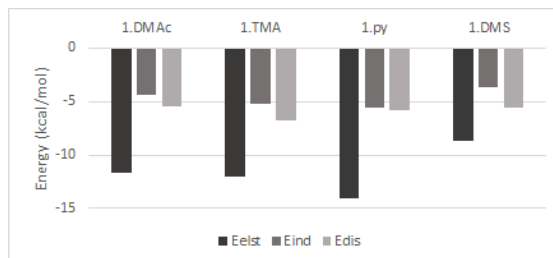


FIGURE 3.3: SAPT(DFT) analysis of complexes with four Lewis bases. All energies are given in kcal/mol.

The SAPT results indicate that the majority (around 80%) of the interaction can be described by electrostatics and dispersion. This suggests that the explicit  $\sigma$ -hole parametrization will be reliable, as electrostatics and dispersion are well described by MM.

### 3.2.3 Incorporation of pseudoatom

With classical parameters for ebselen in hand, as well as theoretical assurance that the system can be adequately described using electrostatics, we began to optimize parameters for the pseudoatom representing the  $\sigma$ -hole. While AMBER supports massless extra points (which

would be ideal to model the  $\sigma$ -hole), these are necessarily hardcoded into the program at this stage. We determined that modification of core routines and recompiling the code was beyond the scope of this work, and represented a significant hurdle to other groups wishing to adopt our model. The pseudoatom was therefore modelled as a H atom, with an associated mass of 1 amu. The SHAKE algorithm is applied to all H atom types, which serves to damp high frequency vibrations and allows longer time steps to be used. The VDW parameters for this atom type were set to 0, so it would only exert influence through the electrostatic force. It is important to note that the non-zero mass of the pseudoatom will slightly effect the dynamics of the system, but not the final equilibrium. The pseudoatom was placed on the selenium atom  $180^\circ$  from the nitrogen, at a distance of  $0.8 \text{ \AA}$  (i.e. within the VDW surface). Force constants of  $119.2 \text{ kcal/mol}\cdot\text{\AA}^2$  and  $150.0 \text{ kcal/mol}\cdot\text{radian}^2$  were applied. The former was chosen to mimic the polarizability of an isolated selenium atom, and the latter was arbitrarily set. By employing a finite force constant, we are able to simulate the polarization contribution to Ch-bonding. The polarizability of an atom can be approximately calculated from first principles as

$$\alpha_{\text{atom}} = 4\pi\epsilon_0 r^3 \quad (3.3)$$

where  $r$  is the atomic radius. The polarizability of a dipole with variable length (such as the polarized Se–pseudoatom bond) can be shown to be

$$\alpha_{\text{dipole}} = \frac{q^2}{k} \quad (3.4)$$

where  $q$  is the charge separation and  $k$  is the force constant. Equating these expressions and solving for  $k$  gives a force constant of  $119.2 \text{ kcal/mol}\cdot\text{\AA}^2$ .

### 3.2.4 Electrostatic potential map

With these parameters in hand, we were able to construct electrostatic potential maps (figure [Figure 3.4](#)), which show good qualitative agreement between the DFT and pseudoatom model potentials. Barely visible in the DFT ESP map is a second  $\sigma$ -hole, opposite the Se–C bond. Carbon is significantly less electronegative than nitrogen, so it doesn't polarize the selenium to the same degree, leading to a much smaller  $\sigma$ -hole. While it is conceivable that this  $\sigma$ -hole could form Ch-bonds as well, we have not observed any evidence of this in any of the derivatives we have studied.<sup>Fellowes2019</sup> We therefore did not attempt to model it, although it could be modelled in the same way as the main  $\sigma$ -hole opposite the nitrogen.

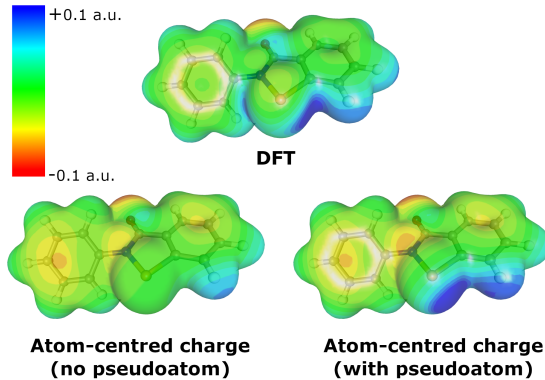


FIGURE 3.4: ESP mapped on the 0.005 a.u. electron density isosurface. The  $\sigma$ -hole is visible as the dark blue region on the DFT and atom-centered charge (with pseudoatom) surfaces.

### 3.2.5 Validation against DFT geometries

A preliminary verification of our model was conducted by comparing the geometries and energies calculated in the SAPT(DFT) analysis with the respective MM values. The Lewis bases chosen for the SAPT(DFT) analysis were constructed in AMBER. GAFF was used for all atoms, and an extra point was added to simulate the lone pair per the method of Dixon and Kollman.<sup>Dixon1997</sup> Geometries were assessed by minimizing the ebselen-Lewis base structure over 1000 steps, then conducting a 2 ns MD trajectory in a vacuum. Trajectories were performed at 300 K for the strongly bonded systems (**1**·py and **1**·DMAc), however the weaker complexes (**1**·TMA and **1**·DMS) tended to dissociate under these conditions. Their trajectories were therefore conducted at 200 K and 100 K respectively. Binding energies were calculated by slowly cooling the system to 0 K, then conducting a short simulation to determine the potential energy of the system. Relevant parameters are given in figure Figure 3.5 and table Table 3.3, alongside DFT values for comparison.

TABLE 3.3: Median geometric parameters for complexes with **1**. DFT equilibrium values are given in brackets for comparison. DFT energies are derived from SAPT(DFT) (table S5). REDO

Complex	$r(\text{Se} \cdots \text{B})$	$\angle(\text{N}-\text{Se} \cdots \text{B})$	$\angle(\text{lone pair})$	Energy (kcal/mol)
<b>1</b> ·py	2.98 Å (2.775 Å)	169.8° (176.2°)	158.2° (165.7°)	-8.376 (-7.093)
<b>1</b> ·DMAc	2.964 Å (2.786 Å)	166.3° (172.4°)	129.7° (117.9°)	-10.351 (-7.551)
<b>1</b> ·TMA	3.091 Å (2.857 Å)	167.6° (177.4°)	100.71° (113.6°)	-6.666 (-6.627)
<b>1</b> ·DMS	3.322 Å (3.265 Å)	165.0° (177.4°)	89.1° (89.8°)	-4.541 (-5.646)

### 3.2.6 Validation against experimental melting point

We also sought to validate our model against the experimentally determined melting point. An ebselen crystal (CSD code **SENGOH**,  $5 \times 5 \times 5$  unit cells, 1000 molecules) was constructed, and placed in a simulation box of the appropriate size at 1 atm. The crystal was heated to 300K,

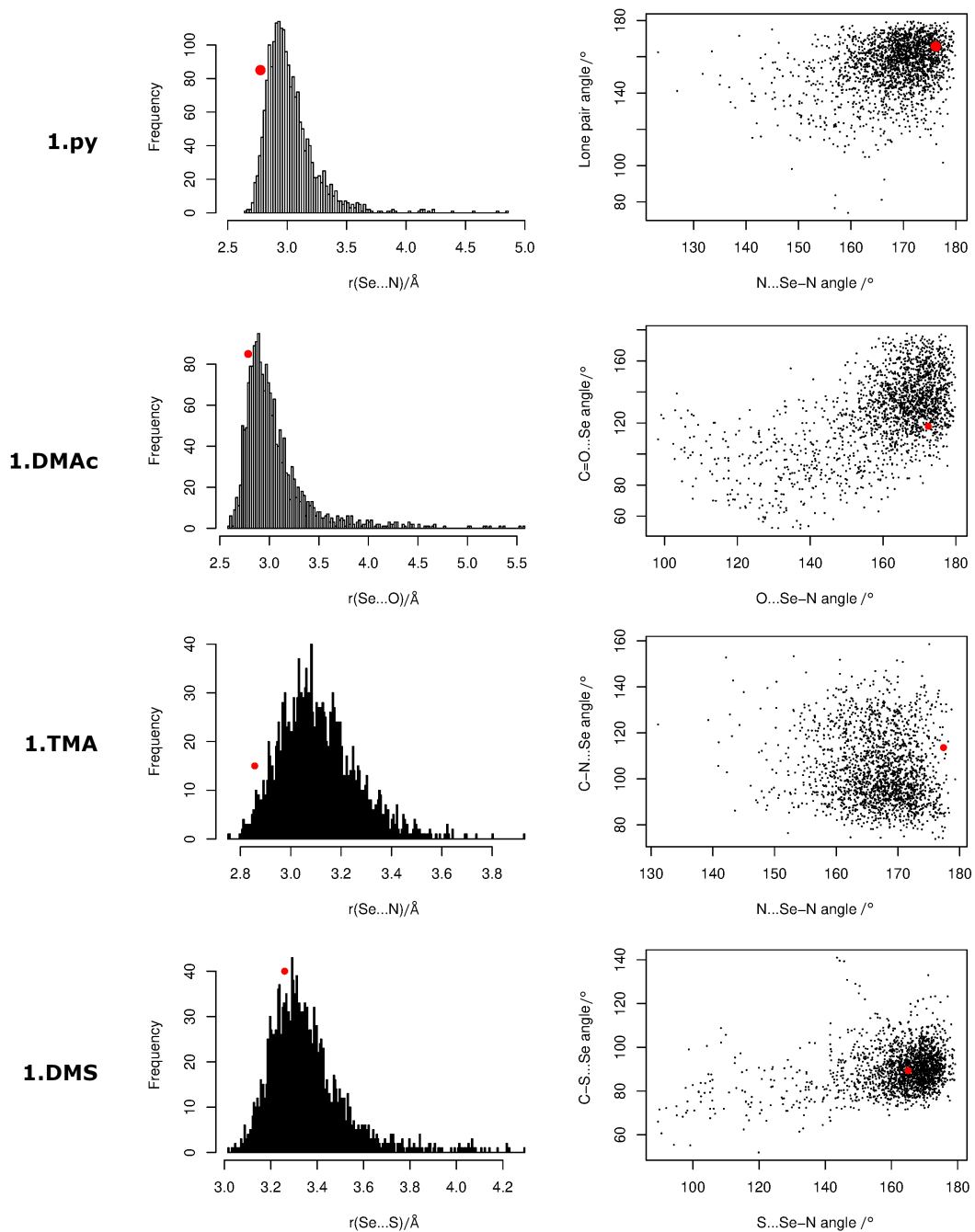


FIGURE 3.5: Distribution of geometric parameters for complexes over a 2 ns trajectory. DFT equilibrium values are shown as red circles. REDO

then 5 random molecules were deleted to create voids (crystal defects) that act as nucleation sites for melting. This avoids the effects of superheating, which is a documented issue in simulated phase transitions.<sup>???</sup> The nucleated geometry was used as a starting point for a series of trajectories at temperatures from 400–500 K in 10 K increments to identify an approximate melting range, then 1 K increments to accurately determine the melting point.

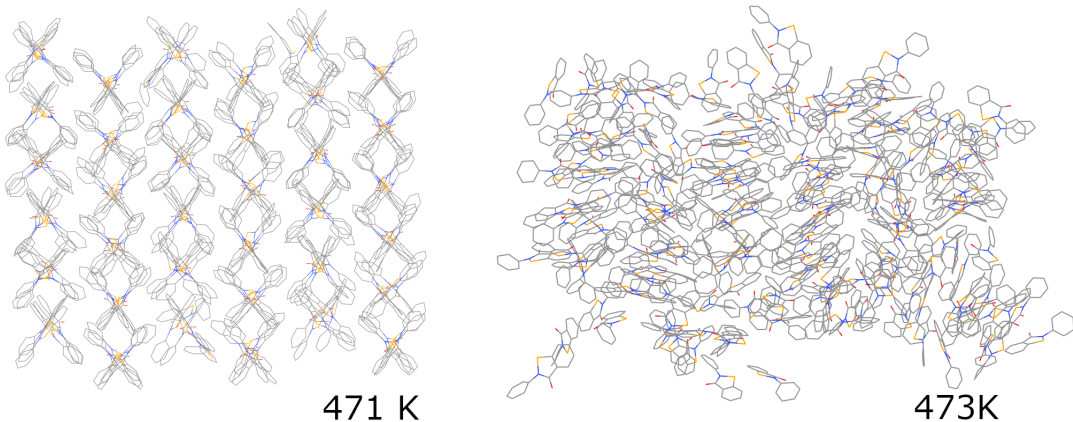


FIGURE 3.6: Melting of a simulated ebselen crystal. The final state of the crystal is shown after 2 ns at the specified temperature.

These results show that Ch-bonds can be adequately described by the inclusion of a positively charged pseudoatom. Interestingly, the weaker complexes (**1**·TMA and **1**·DMS) are better described both in terms of geometry and energy. This may be due to the somewhat decreased charge-transfer component of these interactions, which is poorly described. For the stronger complexes, both the interaction energy and distance are overestimated, representing a compromise between the two criteria.

### 3.2.7 Validation against SOD1 binding

In order to show the utility of our model, we conducted a binding simulation with a known ebselen target. Superoxide dismutase-1 (SOD1) forms a covalent complex with ebselen through the Cys111 residue, which appears to support correct folding of the protein, inhibiting aggregation and associated toxicity.<sup>Capper2018</sup> Although formation of the covalent complex cannot be simulated using our model (as this is a bond-forming process), we are able to visualize the stabilized encounter complex which undergoes ring opening to form the final adduct. Indeed, the Ch-bond formed through the  $\sigma$ -hole can be thought of as the early stages of a nucleophilic attack at the selenium.<sup>Thomas2015</sup> SOD1 (PDB **2C9V**) was chosen because of the availability of an atomic resolution structure, demonstrated evidence of ebselen binding, and it's relatively small size.<sup>Capper2018, Strange2006</sup> The structure was prepared for AMBER by removing disorder, then removing water and ions (the Cu and Zn ions were retained). The ff14SB force field was used

for the protein. The ebselen residue was introduced within the binding groove approximately halfway between the two units. The complex was then neutralized by addition of four  $\text{Na}^+$  ions at the sites of most negative electrostatic potential, and solvated with a TIP3P explicit water model to give a final box size of  $77.095 \times 96.253 \times 78.411\text{\AA}$ . The structure was minimized over 1000 cycles to remove bad contacts, then heated to 300 K over 200 ps. A simulation of 2 ns at 300 K was then performed to assess the average binding geometry, which was found to exhibit a bifurcated Ch-bond between the expected Cys111 sulfur and the adjacent Ile113 backbone carbonyl (figure Figure 3.7). A similar experiment was performed *without* the  $\sigma$ -hole, which failed to bind in a reproducible geometry, with the ebselen molecule wandering through the groove. This is presumably driven by hydrophobic interactions, and the entropic cost of desolvation.

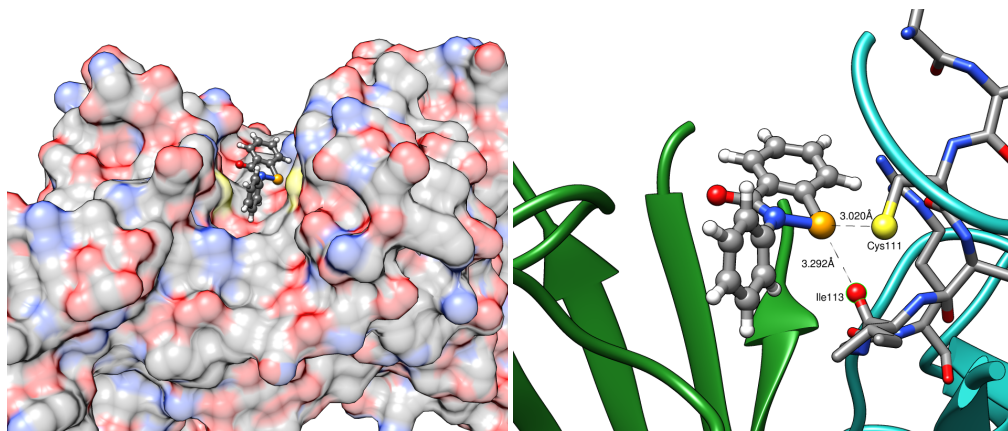


FIGURE 3.7: Average binding geometry of ebselen in the SOD1 groove.

### 3.3 Conclusion

In conclusion, we have developed a set of parameters which can greatly improve modelling of ebselen and its derivatives. Our model gives realistic geometries and energies of gas phase complexes, and reproduces the interaction between ebselen and a protein. Although this work is restricted to ebselen itself, the parameters will be generally applicable to derivatives of ebselen (with appropriate charge fitting). We hope that these results will be useful for the discovery of new targets.



## **Part I**

# **The strength and nature of chalcogen bonding**



## **Chapter 4**

# **New insights into chalcogen bonding provided by co-crystal structures of benzisoselenazolinone derivatives and nitrogen bases.**

This chapter was published in Cryst. Eng. Comm., 22 Jan 2019. [Fellowes2019 \\*](#)

### **4.1 Abstract**

A number of derivatives of benzisoselenazolinones, including the drug ebselen, have been synthesized, and their interactions with various nitrogen bases characterized through x-ray crystallography. Structural studies revealed a strong interaction in all cases, with Se···N distances well within the Van der Waals radii of the constituent atoms. We suggest that there is a significant charge transfer component to this interaction, in contrast to some other interactions of similar strength and directionality. We have also found that this interaction can be enhanced *via* H-bonding to the carbonyl group of the benzisoselenazolinone moiety.

---

\*Compound numbering, section headings, and terminology have been updated to fit this thesis.

## 4.2 Introduction

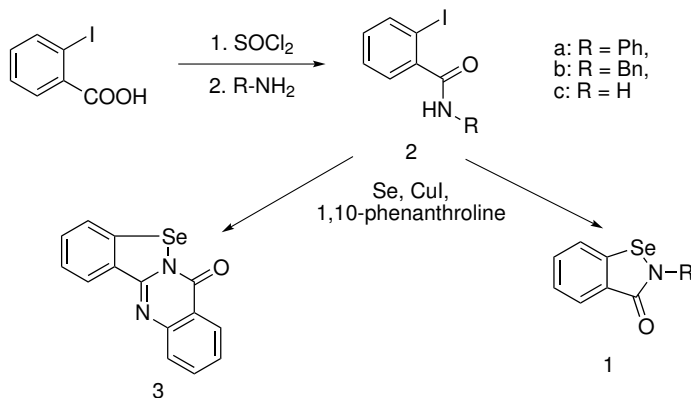
Chalcogen bonding (Ch-bonding) is a class of non-covalent interaction which has recently piqued the interests of the chemical community, and potential applications in materials and medicinal chemistry are emerging.<sup>Mitchell2017, Wonner2017a, Fanfrlik2014, Vogel2019</sup> It bears similarities to the related concept of halogen bonding, and the ubiquitous phenomenon of hydrogen bonding, in that the result is a relatively strong and highly directional non-bonded interaction.<sup>Paolo1974</sup> This strength and directionality has been exploited in crystal engineering,<sup>Gleiter2003, Kremer2016, Huynh2017</sup> anion recognition,<sup>Lim2017, Lim2018, Garrett2016</sup> and bond activation,<sup>Wonner2017, Benz2017, Benz2017a</sup> and appears to play a critical role in protein folding.<sup>Iwaoka2001, Iwaoka2015</sup>

Studies on Te $\cdots$ N Ch-bonds in solution phase have shown they can be as strong as 2.7 kcal/mol.<sup>Garrett2015a</sup> A number of interesting and potentially useful supramolecular polymers have been synthesised and characterised by Vargas-Baca *et al.*, based on tellurium- and selenium-containing heterocycles.<sup>Ho2016, Ho2017</sup>

In our efforts to apply the concept of Ch-bonding to biological systems, we turned to the benzisoselenazolinone scaffold of the antioxidant compound ebselen **1a**. **1a** has been known since the 1980s to effectively scavenge reactive oxygen species *in vivo*.<sup>Muller1984</sup> It has remarkably low toxicity for an organoselenium compound, and is being investigated as a possible treatment for a number of conditions.<sup>Schewe1995, Kil2007, Singh2013, Parnham2000</sup> It is also an ideal scaffold for Ch-bonding, bearing a selenium atom bonded to an electronegative amide nitrogen. Indeed, Ch-bonding in **1a** has been investigated previously in the context of crystal packing of the pure compound, but there is a lack of experimental evidence for interactions with other acceptors.<sup>Thomas2015</sup>

Numerous studies have examined the nature of the Ch-bond, in particular the balance between electrostatic effects (due to anisotropic electrostatic potential around the chalcogen atom), covalent (orbital overlap and electron delocalisation), and dispersion forces.<sup>Oliveira2017, Pascoe2017, DeVleeschouwer2017, Kolar2016, Gl</sup>

In the case of halogen bonding, these contributions are generally well characterized. Halogen bonds range from primarily electrostatic (as in the case of fluorinated iodobenzenes<sup>Prasang2009</sup>) to charge-transfer dominated (molecular halogens<sup>Mulliken1950</sup>). In the case of Ch-bonding in derivatives of **1a**, the contributions are less clear. We therefore sought to characterize Ch-bonding interactions between a number of derivatives of **1a**, and a variety of Ch-bond acceptors.

FIGURE 4.1: Synthesis of Ch-bond donors **1a**, **1b** and **3**.

## 4.3 Results and Discussion

### 4.3.1 Synthesis of benzisoselenazolone derivatives **1a** and **1b**

Compounds **1a** and **1b** were synthesized via published procedures from amides **2a** and **2b**.<sup>Bhabak2010</sup> The Se-tetracycle **3** was isolated in poor yield as the major product from the cyclization of primary amide **2c** in an attempt to form **1c**. It is noteworthy that the spectral characteristics of **3** are essentially identical to reported spectral data of **1c**.<sup>Bhabak2010</sup>

TABLE 4.1: Selected structural parameters of Ch-bonded complexes

Complex	r(N···Se) Å	r(Se–N <sub>1</sub> ) Å	r(Se–C <sub>1</sub> ) Å	r(N <sub>1</sub> –C(O)) Å	∠(N···Se–N <sub>1</sub> ) °	∠(C <sub>para</sub> ···N···Se) °
<b>1a</b> only	—					
<b>1a</b> · DMAP	2.371(1)	1.9676(10)	1.8959(12)	1.2345(14)	174.18(4)	173.52(4)
<b>1b</b> only	—	1.8805(14)	1.8867(16)	1.350(2)	—	—
<b>1b</b> · DMAP M1	2.4276(14)	1.9297(13)	1.8984(15)	1.348(2)	173.93(5)	174.89(5)
<b>1b</b> · DMAP M2	2.4331(14)	1.9191(14)	1.8966(14)	1.349(2)	175.30(5)	158.14(5)
<b>1b</b> · DMAP · H <sub>2</sub> O	2.4046(15)	1.9367(14)	1.9070(14)	1.330(2)	175.54(5)	167.43(5)
<b>1b</b> · quinuclidine	2.5874(17)	1.9077(17)	1.898(2)	1.354(3)	176.77(7)	161.32(7)
<b>1b</b> · DABCO	2.6166(15)	1.9019(14)	1.8967(17)	1.355(2)	175.76(6)	160.00(6)
<b>3</b> only	—	1.883(2)	1.899(3)	1.393(3)	—	—
<b>3</b> · pyridine	2.461(3)	1.926(2)	1.908(3)	1.373(4)	174.13(9)	169.1(1)
<b>3</b> · DMAP	2.304(1)	1.9716(9)	1.918(1)	1.375(1)	173.81(4)	173.16(4)

## 4.4 Co-crystal structures of benzisoselenazolinones and Lewis bases

High quality low temperature crystal structures were obtained for the parent benzisoselenazolinone derivatives **1a**,<sup>Thomas2015</sup> **1b** and the Se-tetracycle **3** and the chalcogen-bonded co-crystals of these compounds with a variety of nitrogen bases, including pyridine, dimethylaminopyridine (DMAP) quinuclidine and DABCO. Powder diffraction patterns were obtained of the bulk

co-crystal material and compared with the single crystal data, with excellent agreement. This provides strong evidence of phase purity, with the exception of **1b**·DMAP, which indicated the presence of the unbound monomers in addition to the Ch-bonded adduct. Relevant structural parameters are presented in [Table 4.1](#), while all thermal ellipsoid plots are presented in the supplementary material (SUPP-Figures 7–15<sup>†</sup>). In the following discussion we begin by assessing the Ch-bond donor abilities of **1a**, **1b**, and **3** by comparing the structural parameters with a common nitrogen base adduct (DMAP), followed by comparison of a single Ch-bond donor **3** with two different nitrogen bases with markedly different basicities (pyridine and DMAP).

#### 4.4.1 Effects of the benziselenazolone on Ch-bond strength

The DMAP adducts of **1a**, **1b** and **3** are characterized by near linear N···Se–N(CO) angles ([Table 4.1](#)) with N<sub>DMAP</sub>···Se distances which are 2.4276(14) and 2.4331(16) Å for the two independent molecules of **1b**, 2.371(1) Å for **1a**, and the strikingly short N···Se distance of 2.304(1) Å for **3**. All are well within the van der Waals radii of N and Se of 3.85 Å.<sup>Batsanov2001</sup> The antipodal Se–N<sub>1</sub> bond distance within these adducts is significantly lengthened compared to the free Ch-bond donors, 0.063 Å in **1a**, 0.049 Å in **1b**, and 0.088 Å in **3**, with the degree of lengthening being related in an inverse sense to the N<sub>DMAP</sub>···Se distance, in all cases the (non-antipodal) Se–C<sub>1</sub> bond is essentially unchanged. These structural parameters suggest an order of Ch-bond donor abilities **1b** < **1a** < **3**, which is supported by theoretical calculations which are discussed below, as well as being consistent with the <sup>77</sup>Se NMR chemical shifts.

#### 4.4.2 Endocyclic bond lengthening associated with stronger complexes

Further discussion is warranted on the **1b**·DMAP adduct; firstly, the two independent molecules of **1b**·DMAP differ significantly with respect to the direction that the nitrogen base lone pair makes with the Se–N<sub>1</sub> bond; in molecule 1 this angle is close to colinear at 174.89(5)<sup>°</sup> while in molecule 2, this deviates significantly from linearity 158.14(5)<sup>°</sup>. Associated with this difference is a slightly longer N<sub>DMAP</sub>···Se distance of 2.4331(14) Å in molecule 2 compared to 2.4276(14) Å in molecule 1 ( $\Delta=0.0055$  Å;  $3\sigma$ ) and a shorter Se–N<sub>1</sub> distance 1.9191(14) Å vs 1.9297(14) Å ( $\Delta=-0.10$  Å;  $7.5\sigma$ ) indicating a slightly weaker interaction. This can be seen in [Figure 4.2](#).

The structural effects described, particularly the lengthening of the Se–N<sub>1</sub> bond are consistent with donation of electron density from the nitrogen lone pair into the Se–N<sub>1</sub> antibonding orbital being a significant component of these N···Se Ch-bonds, which has been described before.<sup>Pascoe2017</sup>

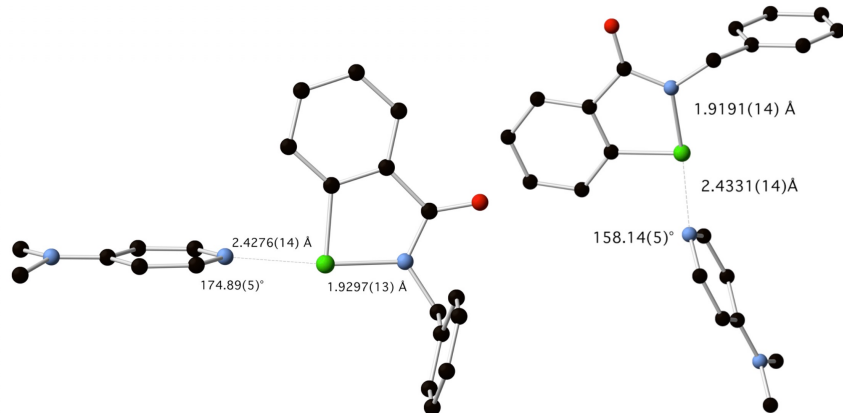


FIGURE 4.2: Structure of **1b**·DMAP, showing the two distinct geometries.

#### 4.4.3 H-bond enhanced Ch-bonding

The second reason for further discussion of the **1b**·DMAP adduct is based on the structural parameters obtained for the hydrate structure **1b**·DMAP·H<sub>2</sub>O which was serendipitously obtained by evaporation of a THF solution in an open flask. The structure is shown in Figure 4.3.

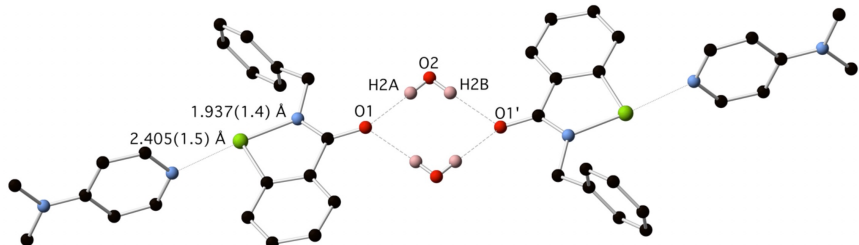


FIGURE 4.3: Structure of **1b**·DMAP·H<sub>2</sub>O.

**1b**·DMAP·H<sub>2</sub>O crystallizes as a centrosymmetric hydrogen-bonded dimer in which two water molecules bridge two molecules of **1b** across a crystallographic inversion centre. Of note, when comparison is made between the structural parameters for **1b**·DMAP molecule 1, which has a similar geometry about the N···Se moiety as for **1b**·DMAP·H<sub>2</sub>O, there is a significant contraction of the N<sub>DMAP</sub>···Se distance from 2.4276(14) Å to 2.4046(14) Å ( $\Delta=-0.023$  Å; 16 $\sigma$ ), and an increase in the Se–N<sub>1</sub> bond distance from 1.9297(13) to 1.9367(14) Å ( $\Delta=0.007$  Å; 5 $\sigma$ ). We have coined the term ‘hydrogen-bond enhanced Ch-bonding’ to describe this interesting structural effect.

#### 4.4.4 Effects of the Lewis base on Ch-bond strength

We were fortunate to obtain crystal structures of the Se-tetracycle **3** with both pyridine and DMAP, which gave us the opportunity to compare the structural effects arising from two Ch-bond acceptors with significantly different basicities. The pyridine adduct of **3** is characterized by a  $N_{PYR} \cdots Se$  distance 2.461(3) Å and  $Se-N_1$  distance of 1.926(2) Å and a near linear  $N_{PYR} \cdots Se-N_1$  angle, the  $Se-N_1$  bond distance is significantly longer than the corresponding distance 1.883(2) Å in non-bound structure of **3**. The DMAP adduct of **3** is characterized by a significantly shorter  $N_{DMAP} \cdots Se$  distance of 2.304(1) Å ( $\Delta = -0.157$  Å) and longer  $Se-N_1$  distance of 1.9716(9) Å ( $\Delta = 0.046$  Å), consistent with a significantly stronger interaction.

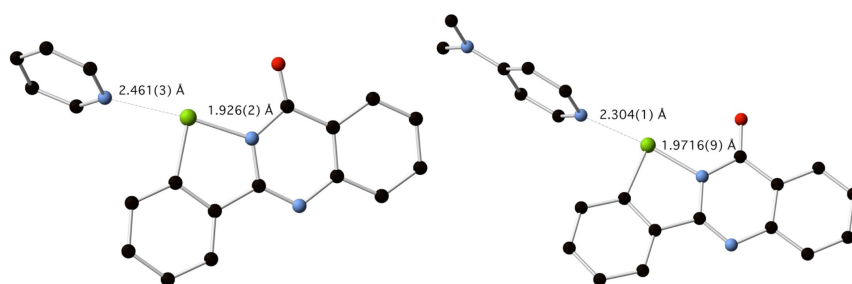


FIGURE 4.4: Pyridine and DMAP adducts of Se-tetracycle **3**.

Ch-bonded co-crystals of the benzisoselenazolinone derivative **1b** with the tertiary amines; quinuclidine and DABCO were obtained and structurally characterized. The adducts are presented in [Figure 4.5](#). The  $N_{QUIN} \cdots Se$  and  $N_{DABCO} \cdots Se$  distances of 2.5874(17) Å and 2.6166(15) Å for **1b**·quinuclidine and **1b**·DABCO respectively are significantly longer than those observed for **1b**·DMAP suggesting an order of Ch-bond strengths with **1b** DABCO < Quinuclidine < DMAP which correlates well with the hydrogen bond acceptor ability of these bases, as quantified by the  $pK_{HB}$  ([Table 4.2](#)).

TABLE 4.2: Hydrogen bond basicities of bases studied.

	pyridine	DABCO	quinuclidine	DMAP
$pK_{HB}$	1.86 <sup>Berthelot1998</sup>	2.63 <sup>Graton2002</sup>	2.71 <sup>Graton2002</sup>	2.80 <sup>Berthelot1998</sup>
<b>1b</b> ·base $r(N \cdots Se)$ / Å	—	2.6166(15)	2.5874(17)	2.4276(14) <sup>a</sup>
<b>1b</b> ·base $\Delta H_f$ / kcal/mol	-6.35	-7.82	—	-7.91

<sup>a</sup>Bond distance given is the shorter of the two coordination environments.

#### 4.4.5 DFT interaction energies, NBO and NEDA analysis

Interaction energies for the complexes were calculated using the  $\omega$ B97X-D dispersion corrected functional, which has been used to study similar systems with good agreement with coupled

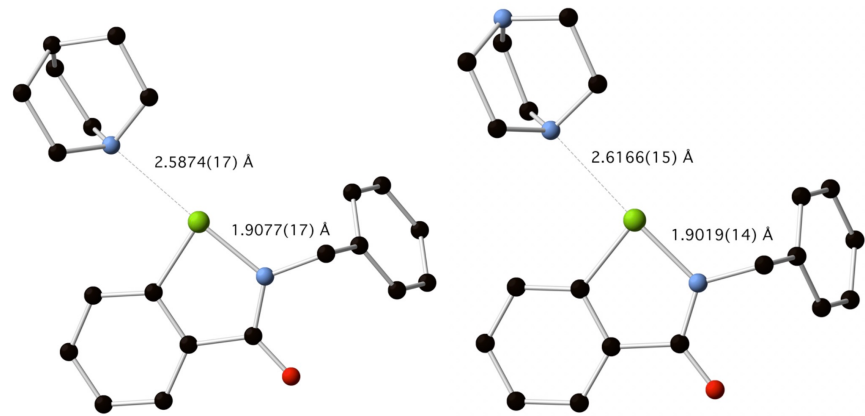


FIGURE 4.5: Adducts of benzisoselenazolinone **1b** with quinuclidine and DABCO.

cluster methods.<sup>Oliveira2017</sup> All geometries were therefore optimized at  $\omega$ B97X-D/def2TZVP, and minima verified by frequency analysis.

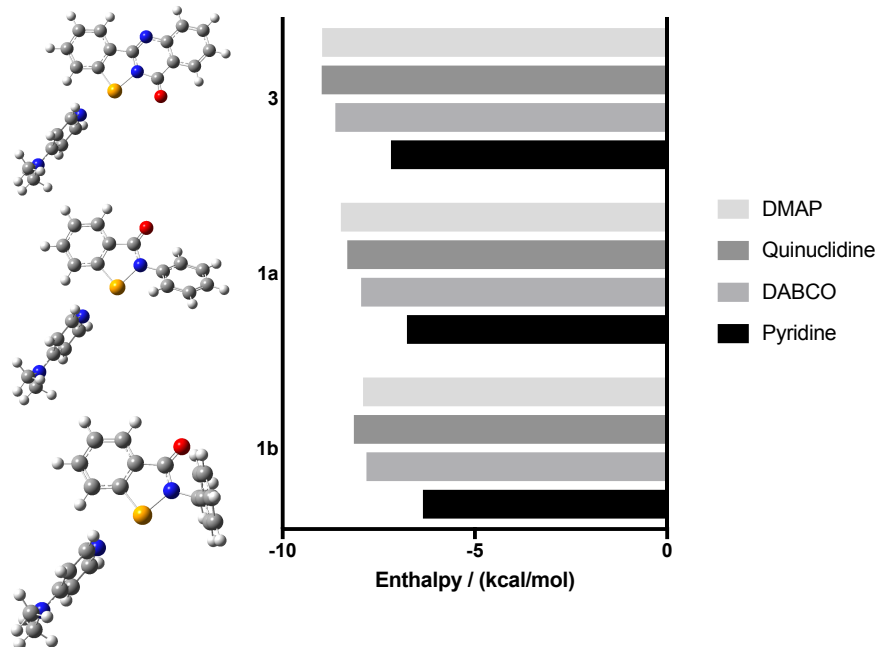


FIGURE 4.6: Interaction enthalpies calculated at  $\omega$ B97X-D/def2TZVP. Optimised geometries for the DMAP complexes are shown to the left.

NBO analysis was conducted on the optimized geometries, which supports our suggestion that there is a strong orbital component to Ch-bonding in these systems. Second order perturbation theory revealed that the energy associated with  $n(N_{\text{base}}) \rightarrow \sigma^*(N_1-\text{Se})$  delocalization was 12.79, 15.45, and 16.23 kcal/mol for **1b**·DMAP, **1a**·DMAP, and **3**·DMAP respectively.

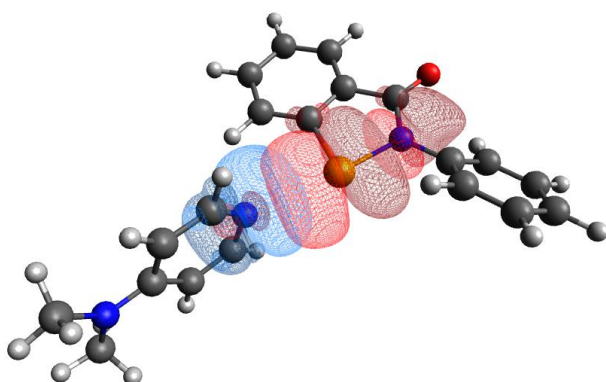


FIGURE 4.7: Overlap of nitrogen lone pair with  $\sigma^*$ (Se - N) in **1a**·DMAP complex.

## 4.5 Conclusion

In summary, we have demonstrated the importance of Ch-bonding between derivatives of ebselen **1a** and a variety of nitrogen bases. These selenium-containing heterocycles form close contacts with electron pair donors, well within the Van der Waals radii, with predictable geometries consistent with the Ch-bonding model. These interactions appear to be primarily due to orbital overlap as opposed to electrostatic or dispersion mediated effects, as evidenced by lengthening of the antipodal Se–N bond, and computational analysis, which is consistent with findings in related systems by Cockroft *et al.*<sup>Pascoe2017</sup> We have also found that the strength of a Ch-bond can be enhanced *via* a hydrogen bond to the carbonyl group of the heterocycle. We hope to exploit the strength and directionality of Ch-bonds in ebselen to target biomolecules such as nucleic acids and proteins using compounds containing the isoselenazolone moiety.

## 4.6 Supplementary materials

### 4.6.1 Synthetic procedures

#### 4.6.1.1 Preparation of 2-phenylbenzo[*d*][1,2]selenazol-3(2*H*)-one **1a**.

Copper iodide (98.4 mg, 0.517 mmol) and 1,10-phenanthroline (83.1 mg, 0.461 mmol) were stirred in anhydrous DMF (3 mL) for 15 mins at r.t., then 2-iodo-N-phenylbenzamide (653.2 mg, 2.021 mmol), selenium (196.9 mg, 2.495 mmol) and potassium carbonate (627.3 mg, 4.539 mmol) were added sequentially under a flow of argon. The mixture was heated at 110°C for 8 h, when TLC showed consumption of starting material. The mixture was then tipped into brine (30 mL) and stirred to form a brown precipitate, which was extracted into DCM (40 mL) and washed

with water ( $2 \times 20$  mL). The DCM solution was filtered through a silica plug, then evaporated, and the residue applied to a SNAP 25 g silica cartridge, eluting with a petroleum ether/ethyl acetate gradient. The major peak was evaporated to afford colourless crystals of **1a** (378.8 mg, 69%, m.p. 179.1–180.3°C, lit. mp 180–181°C).  $^{77}\text{Se}$  NMR  $\delta$  959.66.

#### 4.6.1.2 Preparation of 2-benzylbenzo[*d*][1,2]selenazol-3(2*H*)-one **1b**.

Copper iodide (95.8 mg, 0.503 mmol) and 1,10-phenanthroline (93.8 mg, 0.521 mmol) were stirred in anhydrous DMF (3 mL) for 15 mins at r.t., then N-benzyl-2-iodobenzamide (860.9 mg, 2.553 mmol), selenium (256.6 mg, 3.249 mmol) and potassium carbonate (542.2 mg, 3.923 mmol) were added sequentially under a flow of argon. The mixture was heated at 110°C for 5 h, when TLC showed consumption of starting material. The mixture was then tipped into brine (30 mL) and stirred to form a solid mass, which was dissolved in DCM (40 mL) and washed with water ( $2 \times 20$  mL). The DCM solution was filtered through a silica plug, then evaporated, and the residue applied to a SNAP 50 g silica cartridge, eluting with a petroleum ether/ethyl acetate gradient. The major peak was evaporated to afford pale yellow crystals of **1b** (396.4 mg, 53%, m.p. 137.8–138.8°C).  $^{77}\text{Se}$  NMR  $\delta$  884.02.

#### 4.6.1.3 Preparation of 5*H*-benzo[4,5][1,2]selenazolo[2,3-*a*]quinazolin-5-one **3**.

Copper iodide (96.4 mg, 0.503 mmol) and 1,10-phenanthroline (85.7 mg, 0.476 mmol) were stirred in anhydrous DMF (4 mL) for 10 mins at r.t., then 2-iodobenzamide (510.6 mg, 2.067 mmol), selenium (209.5 mg, 2.653 mmol) and potassium carbonate (506.3 mg, 3.663 mmol) were added sequentially under a flow of argon. The mixture was heated at 110°C for 12 h, when TLC showed consumption of starting material. The mixture was then tipped into brine (30 mL) and stirred to form a solid mass, which was extracted into ethyl acetate (20 mL) and washed with water ( $2 \times 20$  mL). The DCM solution was filtered through a silica plug, then evaporated, and the residue applied to a SNAP 50 g silica cartridge, eluting with a petroleum ether/ethyl acetate gradient. The major peak was evaporated to afford pale yellow crystals of **3** (45.8 mg, 15%, m.p. 267–268°C).  $^{77}\text{Se}$  NMR  $\delta$  992.48.

### 4.6.2 Crystallographic data

Intensity data was collected on an Oxford Diffraction SuperNova CCD diffractometer using either Cu-K $\alpha$  or Mo-K $\alpha$  radiation at 130.0(1) K, or on a Rigaku XtalLAB Synergy at 100.0(1) K. Compound **1b**·DMAP·H<sub>2</sub>O underwent a destructive phase change when cooling to 130 K,

therefore data were collected at 200 K. Data for **3** was collected on the MX1 beamline at the Australian Synchrotron.<sup>Cowieson2015</sup> The temperature was maintained using an Oxford Cryostream cooling device. The structures were solved by direct methods and difference Fourier synthesis.<sup>Sheldrick2015</sup> Thermal ellipsoid plot was generated using the program ORTEP-3<sup>Farrugia1997</sup> integrated within the WINGX<sup>Farrugia1999</sup> suite of programs.

#### 4.6.2.1 Crystal data for **1a**·DMAP

$\text{C}_{20}\text{H}_{19}\text{N}_3\text{OSe}$ ,  $M = 396.34$ ,  $T = 130.0$  K,  $\lambda = 0.71073$  Å, Triclinic, space group  $\bar{P}1$ ,  $a = 8.3674(3)$ ,  $b = 9.8399(5)$ ,  $c = 10.6622(5)$  Å,  $\alpha = 93.296(4)^\circ$ ,  $\beta = 93.021(4)^\circ$ ,  $\gamma = 101.210(4)^\circ$ ,  $V = 857.86(7)$  Å<sup>3</sup>,  $Z = 2$ .  $D_c = 1.534$  mg M<sup>-3</sup>,  $\mu(\text{Mo-K}\alpha) = 2.201$  mm<sup>-1</sup>,  $F(000) = 404$ , crystal size  $0.52 \times 0.34 \times 0.23$  mm. 11339 reflections measured,  $\theta_{\max} = 36.66^\circ$ , 7889 independent reflections,  $R_{\text{int}} = 0.0163$ , the final R was 0.0293 ( $I > 2\theta(I)$ , 6882 reflections) and  $wR(F^2)$  was 0.0721 (all data), GOF 0.992. CCDC 1867205. From dichloromethane/pentane (70%) m.p. 111.3–112.1°C.

#### 4.6.2.2 Crystal data for **1b**

$\text{C}_{14}\text{H}_{11}\text{NOSe}$ ,  $M = 288.20$ ,  $T = 100.0$  K,  $\lambda = 0.71073$  Å, Orthorhombic, space group  $\text{Pca}2_1$ ,  $a = 11.7848(3)$ ,  $b = 4.5869(1)$ ,  $c = 21.3572(5)$  Å,  $V = 1154.48(5)$  Å<sup>3</sup>,  $Z = 4$ .  $D_c = 1.658$  mg M<sup>-3</sup>,  $\mu(\text{Mo-K}\alpha) = 3.233$  mm<sup>-1</sup>,  $F(000) = 576$ , crystal size  $0.63 \times 0.54 \times 0.22$  mm. 44918 reflections measured,  $\theta_{\max} = 45.38^\circ$ , 9588 independent reflections,  $R_{\text{int}} = 0.0481$ , the final R was 0.0331 ( $I > 2\theta(I)$ , 7848 reflections) and  $wR(F^2)$  was 0.0792 (all data), GOF 1.063. CCDC 1867211.

#### 4.6.2.3 Crystal data for **1b**·DMAP·H<sub>2</sub>O

$\text{C}_{21}\text{H}_{21}\text{N}_3\text{OSe} \cdot (\text{H}_2\text{O})$ ,  $M = 428.38$ ,  $T = 200.0$  K,  $\lambda = 0.71073$  Å, Triclinic, space group  $\bar{P}1$ ,  $a = 9.6254(2)$ ,  $b = 10.2486(2)$ ,  $c = 10.6505(2)$  Å,  $\alpha = 83.660(2)^\circ$ ,  $\beta = 76.398(2)^\circ$ ,  $\gamma = 78.423(2)^\circ$ ,  $V = 998.19(4)$  Å<sup>3</sup>,  $Z = 2$ .  $D_c = 125$  mg M<sup>-3</sup>,  $\mu(\text{Mo-K}\alpha) = 1.901$  mm<sup>-1</sup>,  $F(000) = 440$ , crystal size  $0.41 \times 0.32 \times 0.23$  mm. 30047 reflections measured,  $\theta_{\max} = 41.06^\circ$ , 12528 independent reflections,  $R_{\text{int}} = 0.0267$ , the final R was 0.0456 ( $I > 2\theta(I)$ , 6303 reflections) and  $wR(F^2)$  was 0.1219 (all data), GOF 1.000. CCDC 1867213. From THF in an open flask (90%) m.p. 96–97°C.

#### 4.6.2.4 Crystal data for **1b**·DMAP

$\text{C}_{21}\text{H}_{21}\text{N}_3\text{OSe}$ ,  $M = 410.37$ ,  $T = 130.0$  K,  $\lambda = 0.71073$  Å, Triclinic, space group  $\bar{P}1$ ,  $a = 9.6002(4)$ ,  $b = 10.2109(4)$ ,  $c = 19.8380(7)$  Å,  $\alpha = 78.710(3)^\circ$ ,  $\beta = 84.901(3)^\circ$ ,  $\gamma = 77.458(4)^\circ$ ,

$V = 1859.33(13) \text{ \AA}^3$ ,  $Z = 4$ ,  $Zt = 2$ .  $D_c = 1.466 \text{ mg M}^{-3}$ ,  $\mu(\text{Mo-K}\alpha) = 2.034 \text{ mm}^{-1}$ ,  $F(000) = 840$ , crystal size  $0.65 \times 0.24 \times 0.37 \text{ mm}$ . 36541 reflections measured,  $\theta_{\max} = 40.95^\circ$ , 23437 independent reflections,  $R_{\text{int}} = 0.0264$ , the final R was  $0.0448 (I > 2\theta(I))$ , 15177 reflections) and  $wR(F^2)$  was 0.1120 (all data), GOF 1.044. CCDC 1867209. From dichloromethane/pentane (60%) m.p. 86.1–92.5°C.

#### 4.6.2.5 Crystal data for 1b·quinuclidine

$C_{21}H_{24}N_2OSe$ ,  $M = 399.38$ ,  $T = 130.0 \text{ K}$ ,  $\lambda = 1.54184 \text{ \AA}$ , Monoclinic, space group  $P2_1/c$ ,  $a = 10.1610(2)$ ,  $b = 16.0506(3)$ ,  $c = 11.4300(2) \text{ \AA}$ ,  $\beta = 104.622(2)^\circ$ ,  $V = 1803.75(6) \text{ \AA}^3$ ,  $Z = 4$ .  $D_c = 1.471 \text{ mg M}^{-3}$ ,  $\mu(\text{Cu-K}\alpha) = 3.895 \text{ mm}^{-1}$ ,  $F(000) = 824$ , crystal size  $0.29 \times 0.10 \times 0.03 \text{ mm}$ . 12588 reflections measured,  $\theta_{\max} = 77.19^\circ$ , 3771 independent reflections,  $R_{\text{int}} = 0.0379$ , the final R was  $0.0329 (I > 2\theta(I))$ , 3397 reflections) and  $wR(F^2)$  was 0.0849 (all data), GOF 1.028. CCDC 1867207. From dichloromethane/pentane (50%) m.p. 135.2–137.4°C.

#### 4.6.2.6 Crystal data for 1b·DABCO

$C_{20}H_{23}N_3OSe$ ,  $M = 400.37$ ,  $T = 130.0 \text{ K}$ ,  $\lambda = 1.54184 \text{ \AA}$ , Monoclinic, space group  $P2_1/c$ ,  $a = 10.1249(2)$ ,  $b = 15.9246(3)$ ,  $c = 11.4660(2) \text{ \AA}$ ,  $\beta = 106.572(2)^\circ$ ,  $V = 1771.93(6) \text{ \AA}^3$ ,  $Z = 4$ .  $D_c = 1.501 \text{ mg M}^{-3}$ ,  $\mu(\text{Cu-K}\alpha) = 2.965 \text{ mm}^{-1}$ ,  $F(000) = 824$ , crystal size  $0.37 \times 0.17 \times 0.04 \text{ mm}$ . 13121 reflections measured,  $\theta_{\max} = 77.12^\circ$ , 3711 independent reflections,  $R_{\text{int}} = 0.0280$ , the final R was  $0.0258 (I > 2\theta(I))$ , 3333 reflections) and  $wR(F^2)$  was 0.0657 (all data), GOF 1.056. CCDC 1867206. From dichloromethane/pentane (65%) m.p. 131.4–133.3°C.

#### 4.6.2.7 Crystal data for 3

$C_{14}H_8N_2OSe$ ,  $M = 299.18$ ,  $T = 100.0 \text{ K}$ ,  $\lambda = 0.71092 \text{ \AA}$ , Orthorhombic, space group  $Pca2_1$ ,  $a = 17.371(4)$ ,  $b = 5.3080(11)$ ,  $c = 11.633(2) \text{ \AA}$ ,  $V = 1072.6(4) \text{ \AA}^3$ ,  $Z = 4$ .  $D_c = 1.853 \text{ mg M}^{-3}$ ,  $\mu(\text{Mo-K}\alpha) = 3.486 \text{ mm}^{-1}$ ,  $F(000) = 592$ , crystal size  $0.15 \times 0.10 \times 0.02 \text{ mm}$ . 16031 reflections measured,  $\theta_{\max} = 31.56^\circ$ , 2967 independent reflections,  $R_{\text{int}} = 0.0363$ , the final R was  $0.0271 (I > 2\theta(I))$ , 2061 reflections) and  $wR(F^2)$  was 0.0751 (all data), GOF 1.129. CCDC 1867208.

#### 4.6.2.8 Crystal data for 3·pyridine

$C_{19}H_{13}N_3OSe$ ,  $M = 378.28$ ,  $T = 130.0 \text{ K}$ ,  $\lambda = 1.54184 \text{ \AA}$ , Monoclinic, space group  $P2_1/c$ ,  $a = 20.7476(9)$ ,  $b = 4.9407(2)$ ,  $c = 17.6687(7) \text{ \AA}$ ,  $\beta = 107.376(4)^\circ$ ,  $V = 1156.27(5) \text{ \AA}^3$ ,  $Z = 4$ .  $D_c = 1.454 \text{ mg M}^{-3}$ ,  $\mu(\text{Cu-K}\alpha) = 3.018 \text{ mm}^{-1}$ ,  $F(000) = 760$ , crystal size  $0.56 \times 0.05 \times 0.03 \text{ mm}$ .

5766 reflections measured,  $\theta_{\max} = 75.76^\circ$ , 3419 independent reflections,  $R_{\text{int}} = 0.0301$ , the final  $R$  was 0.0346 ( $I > 2\theta(I)$ , 2889 reflections) and  $wR(F^2)$  was 0.0955 (all data), GOF 1.054. CCDC 1867211. From dichloromethane/pentane (70%) m.p. 247.5–248.4°C.

#### 4.6.2.9 Crystal data for 3·DMAP

$C_{21}H_{18}N_4OSe$ ,  $M = 421.35$ ,  $T = 100.0$  K,  $\lambda = 0.71073$  Å, Triclinic, space group  $P\bar{1}$ ,  $a = 8.8093(2)$ ,  $b = 10.7445(2)$ ,  $c = 10.9812(2)$  Å,  $\alpha = 111.687(2)^\circ$ ,  $\beta = 109.283(2)^\circ$ ,  $\gamma = 96.631(2)^\circ$ ,  $V = 877.57(3)$  Å<sup>3</sup>,  $Z = 2$ ,  $Z' = 2$ .  $D_c = 1.595$  mg M<sup>-3</sup>,  $\mu(\text{Mo-K}\alpha) = 2.159$  mm<sup>-1</sup>,  $F(000) = 428$ , crystal size  $0.18 \times 0.11 \times 0.06$  mm. 56053 reflections measured,  $\theta_{\max} = 41.07^\circ$ , 11273 independent reflections,  $R_{\text{int}} = 0.0547$ , the final  $R$  was 0.0358 ( $I > 2\theta(I)$ , 8667 reflections) and  $wR(F^2)$  was 0.0872 (all data), GOF 1.048. CCDC 1867212. From dichloromethane/pentane (80%) m.p. 248.8–249.4°C.

# Chapter 5

## Hammett relationships and the strength of the Ch-bond

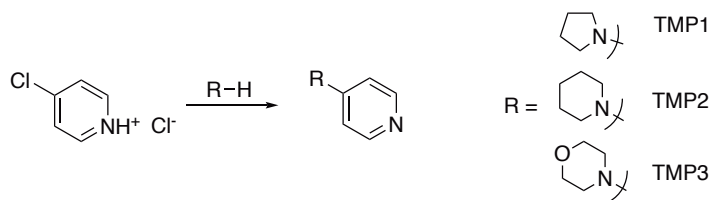
### 5.1 Introduction

In the previous chapter, we established that Ch-bonding is not only present in ebselen derivatives, but dominates packing in crystals of the pure compound (through  $\text{Se}\cdots\text{O}$  interactions) and in co-crystals with a variety of Lewis bases. In this chapter, we extend our investigation to a wider range of derivatives with systematically varied electronic properties.

#### LINEAR FREE ENERGY RELATIONSHIPS

### 5.2 Results and discussion

Our previous work had shown that electron-rich pyridines (specifically DMAP) formed the strongest Ch-bonds out of all the bases trialled. This is roughly consistent with the hydrogen bond basicity ( $\text{pK}_{\text{HB}}$ ) of the bases (Table 4.2). The planar geometry and aromatic character of DMAP may also facilitate crystallisation, as opposed to the relatively bulky and flexible aliphatic bases which may not pack as efficiently. For these reasons, we restricted the bases used in this study to other electron-rich pyridines. Although DMAP is already a very strong base, the basicity can be increased by incorporating the aniline nitrogen in another ring. This reduces the energetic penalty associated with the delocalisation of the lone pair into the pyridine ring, by forcing a more planar geometry upon the nitrogen.<sup>???</sup> Compounds **4a**, **4b** and **4c** were therefore synthesised by treating 4-chloropyridine hydrochloride with 2 equivalents of the appropriate base (Scheme 5.1).



SCHEME 5.1: Synthesis of Lewis bases **4a**, **4b** and **4c**.

The benzisoselenazolone derivatives **1a**, **1d**, **1e**, **1f**, **1g**, **1h**, **1i**, **1j** and **1k** were prepared by the reaction of substituted anilines with a selenenyl chloride intermediate, ultimately derived from anthranilic acid ([Scheme 5.2](#)). The one-pot selenocyclisation reaction used in the previous chapter often did not tolerate the various functional groups on the aryl ring, affording reduction, cross-coupling, or protodehalogenation byproducts (??).

Co-crystals of the benzisoselenazolones and pyridines were grown by vapour diffusion from an equimolar solution in dichloromethane/pentane. Relevant structural parameters are given in [Table 5.1](#). In addition to the structural parameters, we characterised the various Ch-bonds using Bader's QTAIM framework. Depending on the quality of the data we were able to obtain for each crystal, we used:

- experimental electron density from a multipole refinement with atomic coordinates determined from high angle refinement ( $d < 0.8\text{\AA}$ ),
- experimental electron density from a multipole refinement with atomic coordinates determined by refinement using aspherical scattering factors derived from the DFT electron density,
- density derived from the DFT calculation.

The second "hybrid" strategy has the advantage of being able to capture electron density effects not fully described by DFT, while not requiring a large amount of weak high-angle (or neutron) data for the reliable determination of atomic coordinates. The low-angle data, however, does need to be free from faults, so this strategy may still not be appropriate for all data sets.

### 5.2.1 Hammett plots of bond lengths.

Evident in this data is a trend of increasing Ch-bond length with increasing electron donating character of the substituent. There are a number of methods to quantify this property of the substituent, and we will explore a couple of the most common. The Hammett substituent parameter  $\sigma$  for a given substituent is determined from the ionization equilibrium of the parent carboxylic acid. Although originally used to explain reaction *kinetics* with an associated reaction constant  $\rho$ , the substituent constant provides a convenient measure of electron donating

Compound	R =	Compound	R =	Compound	R =
<b>1a</b>	-H	<b>1f</b>	-CF <sub>3</sub>	<b>1i</b>	-CH <sub>3</sub>
<b>1d</b>	-NO <sub>2</sub>	<b>1g</b>	-Br	<b>1j</b>	-OMe
<b>1e</b>	-CN	<b>1h</b>	-CO <sub>2</sub> Et	<b>1k</b>	-OEt

SCHEME 5.2: Synthesis of benziselenazolone derivatives **1a**, **1d**, **1e**, **1f**, **1g**, **1h**, **1i**, **1j** and **1k**.

TABLE 5.1: Selected structural and electron density parameters of Ch-bonded complexes.

Complex	r(N···Se) Å	r(Se–N <sub>1</sub> ) Å	r(Se–C <sub>1</sub> ) Å	r(N <sub>1</sub> –C(O)) Å	∠(N···Se–N <sub>1</sub> ) °	∠(C <sub>para</sub> ···N···Se) °	$\rho_{BCP}(\text{Se} \cdots \text{N})$ e/Å <sup>3</sup>	$\nabla^2(\rho_{BCP})(\text{Se} \cdots \text{N})$ e/Å <sup>5</sup>
<b>1a</b>	—	1.896(3)	1.892(4)	1.359(5)	—	—	—	—
<b>1d</b>	—	—	—	—	—	—	—	—
<b>1e</b>	—	1.894(2)	1.877(2)	1.372(2)	—	—	—	—
<b>1f<sup>a</sup></b>	—	1.880(9)	1.889(9)	1.38(1)	—	—	—	—
<b>1f<sup>b</sup></b>	—	1.898(8)	1.901(9)	1.37(1)	—	—	—	—
<b>1g</b>	—	1.898(2)	1.889(2)	1.371(3)	—	—	—	—
<b>1h</b>	—	1.902(2)	1.879(2)	1.371(3)	—	—	—	—
<b>1i</b>	—	1.904(3)	1.890(3)	1.365(4)	—	—	—	—
<b>1j</b>	—	1.8741(9)	1.887(1)	1.356(1)	—	—	—	—
<b>1k</b>	—	1.901(3)	1.885(4)	1.357(4)	—	—	—	—
<b>1a-DMAP</b>	2.371(1)	1.968(1)	1.896(1)	1.358(2)	174.18(4)	173.51(6)	0.3511	2.6960 <sup>c</sup>
<b>1d-DMAP</b>	2.240(3)	1.967(2)	1.883(2)	1.340(2)	174.27(9)	176.8(1)	0.4755	3.2960 <sup>d</sup>
<b>1e-DMAP</b>	2.301(1)	1.997(1)	1.899(2)	1.368(2)	174.79(5)	167.57(6)	0.4130	2.5210 <sup>c</sup>
<b>1e-DMAP<sup>e,a</sup></b>	2.254(2)	2.019(2)	1.902(1)	1.366(2)	174.46(6)	176.33(7)	0.4780	2.4816 <sup>d</sup>
<b>1e-DMAP<sup>e,b</sup></b>	2.308(2)	1.993(1)	1.901(1)	1.372(2)	174.93(5)	167.85(7)	0.4284	2.4558 <sup>d</sup>
<b>1f-DMAP</b>	2.3347(9)	1.9855(9)	1.899(1)	1.372(1)	175.24(4)	162.65(5)	0.4048	2.4112 <sup>d</sup>
<b>1g-DMAP</b>	2.3215(7)	1.9840(7)	1.9021(8)	1.362(1)	173.85(3)	173.56(4)	0.4058	3.1160
<b>1h-DMAP<sup>e</sup></b>	2.322(1)	1.982(1)	1.902(1)	1.367(2)	174.96(4)	172.86(6)	—	—
<b>1i-DMAP</b>	2.4301(4)	1.9341(4)	1.8918(4)	1.3650(6)	175.33(1)	158.64(2)	—	—
<b>1j-DMAP<sup>f,a</sup></b>	2.270(1)	1.9689(9)	1.899(1)	1.350(1)	174.17(3)	159.44(4)	—	—
<b>1j-DMAP<sup>f,b</sup></b>	2.4496(9)	1.9267(9)	1.895(1)	1.357(1)	174.57(3)	160.53(4)	—	—
<b>1j-DMAP<sup>g,a</sup></b>	2.334(1)	1.965(1)	1.894(1)	1.363(1)	175.95(5)	155.71(6)	—	—
<b>1j-DMAP<sup>g,b</sup></b>	2.407(1)	1.9411(1)	1.894(1)	1.358(2)	176.12(5)	156.60(6)	—	—
<b>1k-DMAP<sup>a</sup></b>	2.517(2)	1.921(1)	1.895(2)	1.356(3)	172.30(6)	158.37(8)	—	—
<b>1k-DMAP<sup>b</sup></b>	2.327(5)	1.931(2)	1.894(2)	1.353(3)	171.4(1)	151.2(3)	—	—
<b>1a-4a</b>	2.350(1)	1.9830(9)	1.8985(7)	1.3616(8)	174.20(3)	176.46(4)	0.2419	5.4650
<b>1d-4a</b>	—	—	—	—	—	—	—	—
<b>1e-4a</b>	2.289(1)	2.000(1)	1.902(1)	1.363(2)	174.77(5)	175.06(7)	—	—
<b>1f-4a</b>	—	—	—	—	—	—	—	—
<b>1g-4a</b>	2.319(2)	1.981(2)	1.895(1)	1.362(2)	174.57(6)	174.60(8)	0.3617	3.7020
<b>1h-4a</b>	2.337(3)	1.982(3)	1.906(4)	1.374(5)	173.5(1)	170.1(2)	—	—
<b>1i-4a</b>	2.272(1)	1.986(1)	1.905(1)	1.351(2)	172.66(5)	173.51(6)	—	—
<b>1j-4a</b>	—	—	—	—	—	—	—	—
<b>1k-4a<sup>a</sup></b>	2.356(3)	1.972(3)	1.898(3)	1.355(4)	174.5(1)	170.2(1)	—	—
<b>1k-4a<sup>b</sup></b>	2.371(3)	1.964(3)	1.898(3)	1.360(4)	174.9(1)	170.9(1)	—	—
<b>1a-4b</b>	—	—	—	—	—	—	—	—
<b>1d-4b</b>	—	—	—	—	—	—	—	—
<b>1e-4b</b>	—	—	—	—	—	—	—	—
<b>1f-4b</b>	—	—	—	—	—	—	—	—
<b>1g-4b</b>	—	—	—	—	—	—	—	—
<b>1h-4b</b>	—	—	—	—	—	—	—	—
<b>1i-4b</b>	—	—	—	—	—	—	—	—
<b>1j-4b</b>	—	—	—	—	—	—	—	—
<b>1k-4b</b>	2.3361(8)	1.9576(8)	1.9043(9)	1.353(1)	173.90(3)	171.42(4)	—	—
<b>1a-4c</b>	2.414(2)	1.960(2)	1.902(2)	1.366(2)	175.46(6)	166.23(8)	—	—
<b>1d-4c</b>	—	—	—	—	—	—	—	—
<b>1e-4c<sup>e</sup></b>	2.301(1)	1.993(1)	1.907(1)	1.368(2)	173.08(5)	164.75(6)	—	—
<b>1f-4c</b>	—	—	—	—	—	—	—	—
<b>1g-4c</b>	2.381(2)	1.975(2)	1.905(2)	1.367(2)	173.84(6)	174.97(8)	0.3536	3.4890
<b>1h-4c</b>	2.337(3)	1.982(3)	1.906(4)	1.374(5)	173.5(1)	170.1(2)	—	—
<b>1i-4c</b>	2.412(5)	1.977(5)	1.908(5)	1.360(7)	174.4(2)	178.9(2)	—	—
<b>1j-4c</b>	—	—	—	—	—	—	—	—
<b>1k-4c<sup>a</sup></b>	2.398(4)	1.958(4)	1.894(6)	1.367(6)	174.6(2)	174.1(2)	—	—
<b>1k-4c<sup>b</sup></b>	2.448(6)	1.951(4)	1.901(5)	1.367(5)	175.5(2)	170.5(3)	—	—

<sup>a</sup>Environment *a*<sup>b</sup>Environment *b*<sup>c</sup>Fully experimental density used<sup>d</sup>DFT density used<sup>e</sup>DCM solvate<sup>f</sup>Polymorph 1<sup>g</sup>Polymorph 2

character for ground state phenomena as well.<sup>???</sup> Closely linked to the substituent constant  $\sigma$  are the values of  $\sigma^+$  and  $\sigma^-$ , which can be used when mesomeric effects have a strong influence on the property being studied. Hammett substituent parameters are particularly convenient as they have been determined for a wide variety of substituents.

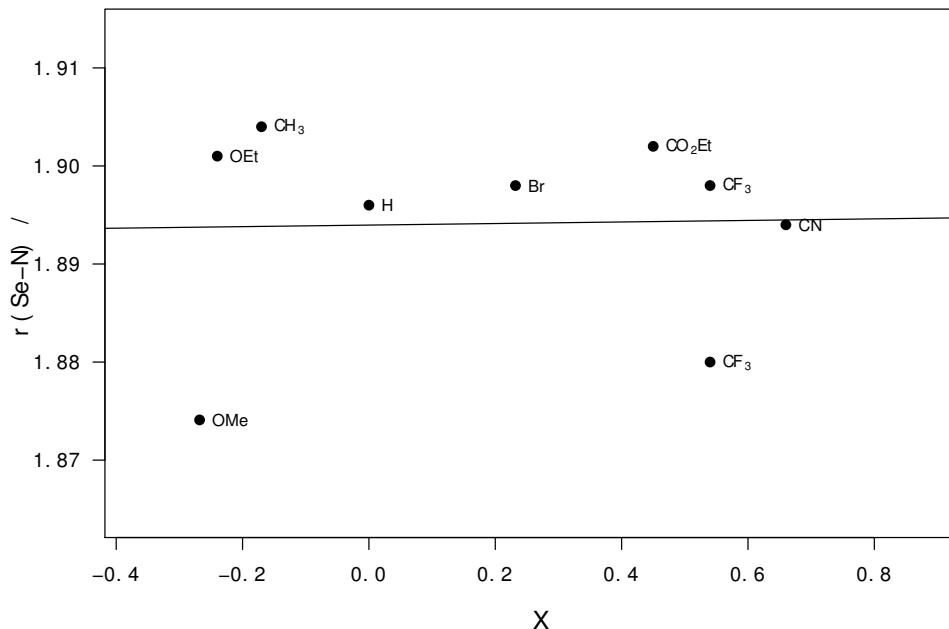


FIGURE 5.1: Hammett plot of endocyclic Se–N bond length of uncomplexed ebselen derivatives.

As can be seen in ??, there is practically no correlation between the electronic properties of the aryl ring and the endocyclic Se–N bond length in crystals of the unbound ebselen derivatives. This is not unexpected, as in all cases the crystals consist of one dimensional chains of ebselen molecules Ch-bonded to the carbonyl oxygen of the next (??). As the magnitude of the  $\sigma$ -hole (Ch-bond donor ability) is *increased* by an electron withdrawing substituent, the Ch-bond acceptor ability of the carbonyl is *decreased*. These opposing effects appear to be approximately equal in magnitude, so cancel each other out and give a very flat Hammett plot.

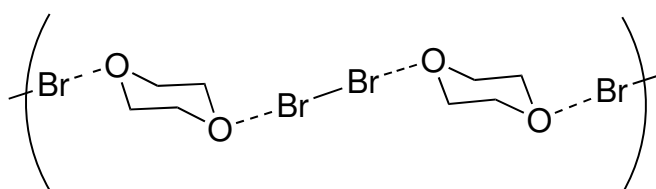


FIGURE 5.2: One dimensional chains formed by Ch-bonding between the selenium and carbonyl oxygen in **1i**. All other ebselen derivatives display a similar packing motif.

Fortunately, inspecting the same bond length in co-crystals of ebselen derivatives and a Lewis base gives us a much clearer dependence, as can be seen in ?? . This is because the Ch-bond

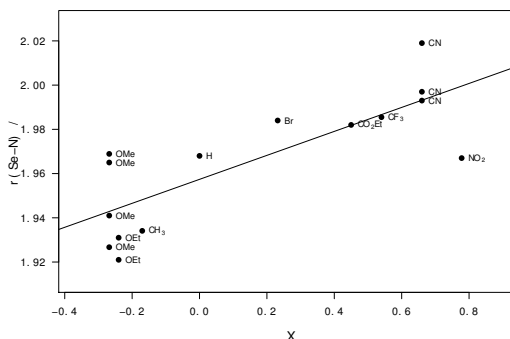


FIGURE 5.3: Hammett plots of endocyclic Se–N bond length and Se ··· N Ch-bond length of ebselen derivatives complexed with DMAP. The lines are described by the equations  $r(\text{Se}-\text{N}) = (1.957(5) + 0.054(12) \times \sigma_X) \text{ Å}$  and  $r(\text{Se} \cdots \text{N}) = (2.385(17) - 0.15(4) \times \sigma_X) \text{ Å}$ .

acceptor ability is now independent of the electronic properties of the Ch-bond donor, so the Se–N bond length is determined solely by the latter. Linear regression analysis affords the relationship  $r(\text{Se}-\text{N}) = (1.957(5) + 0.054(12) \times \sigma_X) \text{ Å}$  with a correlation coefficient of 0.6297.

An inverse correlation can be seen in the Se ··· N Ch-bond length in ?? . The gradient of the line is now negative and somewhat steeper, at  $-0.15(4) \text{ Å}$ . However the correlation coefficient is decreased to 0.5056. The reason for this is apparent in the left hand side of the plot. While the more strongly Ch-bonded systems (with electron withdrawing substituents) are generally very well described by the regression model, the electron rich derivatives **1j** and **1k** vary significantly in their bond lengths.\* Indeed, omitting these data points improves the correlation coefficient to 0.8148 while the gradient and intercept are almost unchanged at  $-0.156(28) \text{ Å}$  and  $2.386(15) \text{ Å}$  respectively, suggesting that the model is appropriate, and that there is some other effect occurring in electron rich systems.

DFT calculations show that the vibrational mode associated with Ch-bond stretching is found at very low energy. The force constant is  $5\text{--}10 \mu\text{dyne}\cdot\text{\AA}^{-1}$ , which means that the energetic penalty associated with a  $0.18 \text{ \AA}$  deformation (the difference between the shortest and longest Ch-bond length) is only  $0.02\text{--}0.03 \text{ kcal}\cdot\text{mol}^{-1}$ . Crystal packing forces (the sum of weak interactions such as C-H/ $\pi$ ,  $\pi/\pi$  and C-H/O interactions) are commonly accepted to be in the range of

\*This is also visible, though less apparent, in the plot of endocyclic bond lengths ??.

1–2 kcal·mol<sup>-1</sup>, so it is perhaps not surprising that the Ch-bond is deformed by the crystal environment.<sup>Dunitz1988</sup>

That said, there are no obvious differences between the two Ch-bond environments in any of the crystals that display this effect. We considered the possibility that this was a crystallographic artefact, either a manifestation of missed symmetry, disorder, or a doubled cell. However, we quickly dismissed this, as the data was of extremely high quality, and no alerts were raised in the ADDSYM routine of PLATON. We additionally performed a solid state IR experiment, which showed doubling of the carbonyl peak, confirming that there were indeed two distinct environments (??). In the pure compound (where there is only one Ch-bond environment) the carbonyl peak is found at approximately 1630 cm<sup>-1</sup> and is sharp and well defined. In the co-crystal, two effects are observed. Firstly, the signal moves to a lower energy as the C=O bond loses some double bond character due to the delocalisation of the pyridine lone pair into the selenium heterocycle (??). Secondly, the signal splits into two peaks at around 1560 cm<sup>-1</sup> and 1575 cm<sup>-1</sup>, corresponding to the strongly and weakly Ch-bonded environments in the crystal.

## 5.2.2 Solution-phase studies

While the above crystallographic analysis gives a useful qualitative understanding of the strength of the Ch-bond, we sought an experimental method that could accurately determine bond energies, so that we could easily compare our Ch-bonded complexes with those dominated by other interactions.

### 5.2.2.1 NMR titration experiments

NMR titrations are a useful tool for the determination of binding affinities in supramolecular and host-guest chemistry. <sup>1</sup>H and <sup>19</sup>F NMR have both been used to study halogen bonded systems, however we decided to take advantage of the unique NMR characteristics of the <sup>77</sup>Se nucleus to probe the Ch-bond in our systems for the following reasons:

- the nucleus has an extremely wide chemical shift range (-1000–2000 ppm),
- the chemical shift is very sensitive to the electronic environment around the selenium,
- the selenium is at the heart of the interaction, so any electronic changes should manifest clearly,
- the spectrum (for our compounds) is extremely simple, featuring only one singlet,

FIGURE 5.4: Solid state IR spectrum of **1k**-DMAP. The spectrum of the pure **1k** (which contains only one molecule in the asymmetric unit) is shown in gray. Splitting of the carbonyl peak is visible in the insert.

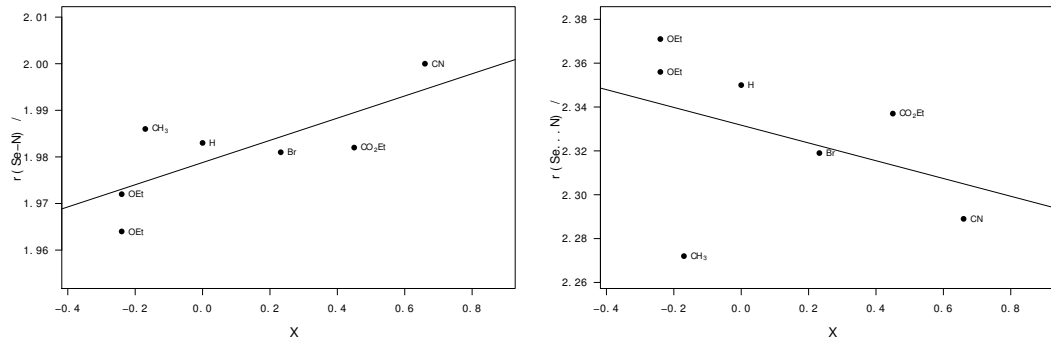


FIGURE 5.5: Hammett plots of endocyclic Se–N bond length and Se···N Ch-bond length of ebselen derivatives complexed with **4a**. The lines are described by the equations  $r(\text{Se}-\text{N}) = (1.9788(32) - 0.024(9) \times \sigma_X) \text{ Å}$  ( $R^2 = 0.5722$ ) and  $r(\text{Se}-\text{N}) = (2.331(14) - 0.04(4) \times \sigma_X) \text{ Å}$  ( $R^2 = 0.1588$ )

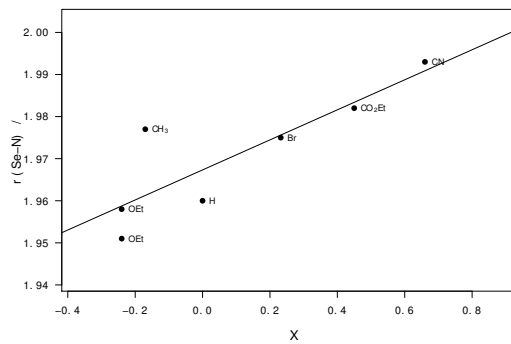


FIGURE 5.6: Hammett plots of endocyclic Se–N bond length and Se···N Ch-bond length of ebselen derivatives complexed with **4c**. The line is described by the equation  $r(\text{Se}-\text{N}) = (1.9673(34) - 0.035(10) \times \sigma_X) \text{ Å}$  ( $R^2 = 0.7260$ ) and  $r(\text{Se}-\text{N}) = (2.397(77) - 0.13(2) \times \sigma_X) \text{ Å}$  ( $R^2 = 0.8708$ ).

- the experiment is moderately sensitive (slightly more sensitive than  $^{13}\text{C}$ ).

We devised a titration experiment, where a solution of a Lewis base is gradually added to a solution of the Ch-bond donor, and the chemical shift of the selenium is measured at the various concentrations of base. As the concentration of base increases, a greater proportion of the selenium species will be in a Ch-bonded environment, with an associated increase in electron density at the selenium due to the coordinated base. This will lead to an upfield shift of the selenium resonance.

It is important to note that even in the absence of a Lewis base, the organoselenium species will still likely feature a Ch-bond to the carbonyl oxygen of another molecule. This interaction can be seen to dominate the crystal packing of ebselen derivatives in the absence of any other coordinating species. This is substantially weaker than a Se . . . N interaction, but non-negligible. We must therefore view these as *competition* experiments, rather than an absolute measure of binding energy.

For single site binding (a valid approximation for these systems, as the single  $\sigma$ -hole is likely to out-compete all other interactions), the dissociation constant can be expressed as

$$K_d = \frac{[\text{ebs}][\text{base}]}{[\text{ebs} \cdot \text{base}]} \quad (5.1)$$

If the Ch-bond formation/breaking is slow on the NMR timescale, two distinct resonances will be observed that correspond to the “free” (Ch-bonded to a carbonyl oxygen) and “bound” (Ch-bonded to the Lewis base) selenium species, and their relative concentrations can be determined by integration of the signals. As it happens, this is not the case, and the process is fast relative to the NMR timescale. The observed chemical shift is therefore the mole fraction ( $f_{\text{ebs}} = [\text{ebs}]/[\text{ebs}]_0$  and  $f_{\text{ebs} \cdot \text{base}} = [\text{ebs} \cdot \text{base}]/[\text{ebs}]_0$ ) weighted average of the chemical shifts of the two species:

$$\delta_{\text{observed}} = \delta_{\text{ebs}} f_{\text{ebs}} + \delta_{\text{ebs} \cdot \text{base}} f_{\text{ebs} \cdot \text{base}} \quad (5.2)$$

If we consider only the *change* in chemical shift from the free species, this becomes simply:

$$\Delta(\delta_{\text{observed}}) = \Delta(\delta_{\text{ebs} \cdot \text{base}}) f_{\text{ebs} \cdot \text{base}} \quad (5.3)$$

$$= \Delta(\delta_{\text{ebs} \cdot \text{base}}) \left( \frac{[\text{ebs} \cdot \text{base}]}{[\text{ebs}]_0} \right) \quad (5.4)$$

From here we can rearrange the equilibrium expression (??) and mass balance equation ( $[\text{ebs}]_0 = [\text{ebs}] + [\text{ebs} \cdot \text{base}]$ ), and substitute them in to arrive at the generic binding isotherm

equation:

$$\Delta(\delta) = \frac{\Delta(\delta_{\text{ebs-base}}) \times [\text{base}]}{K_d + [\text{base}]} \quad (5.5)$$

This assumes that there is insignificant depletion of the base concentration due to complexation.<sup>Thordarson2011</sup> Such an assumption may not be entirely valid for this situation, which may explain the imperfect fitting. However, the analysis is considerably simplified, and adequate standard deviations are obtained using this method.

The resulting  $K_d$  values can be converted to free energies:

$$\Delta G = -RT \ln K_d \quad (5.6)$$

A saturated solution of the organoselenium derivative in chloroform was used, due to the high solubility (to reduce acquisition time) and non-coordinating nature (to minimise Ch-bonding to the solvent). This was spiked with a small amount of deuteriochloroform for the lock signal. Spectra were acquired on a 500 MHz instrument, using a 60° pulse and 1 s relaxation delay, until an unambiguous  $^{77}\text{Se}$  resonance was observed. The resulting chemical shifts were then tabulated and plotted against the concentration of the Lewis base. These are shown in ??.

Non-linear regression analysis was performed with the `nls` function in the R software package, and the calculated values are given in ??.<sup>R</sup>

TABLE 5.2: Binding energies for complexes of **1b**, **1k**, **1g**, **1a** and **1e** with DMAP, derived from  $^{77}\text{Se}$ -NMR titration experiments.

Complex	Binding energy (kcal/mol)	$\Delta(\delta_{\text{ebs-base}})$ (ppm)
<b>1b</b> ·DMAP	0.17(6)	41.6
<b>1k</b> ·DMAP	0.47(3)	102.8
<b>1g</b> ·DMAP	0.87(5)	104.2
<b>1a</b> ·DMAP	1.12(4)	70.05
<b>1e</b> ·DMAP	2.28(5)	82.62

Although there is insufficient data to derive clear trends from a Hammett relationship, we can nevertheless visualise the data in a plot, which shows that the Ch-bond gets appreciably stronger with more electron withdrawing substituents (??).

### 5.2.2.2 UV-Vis titration experiment

Although extremely useful, the NMR titration technique had a number of drawbacks. Firstly, relatively large amounts ( $\sim 100$  mg) of the Ch-bond donor were required. For simple systems such as these, this was not an issue, however we hoped to apply the technique to less synthetically accessible molecules, which may not be available in such quantities. Secondly, the experiment is quite time consuming, with tens of minutes required per spectrum.

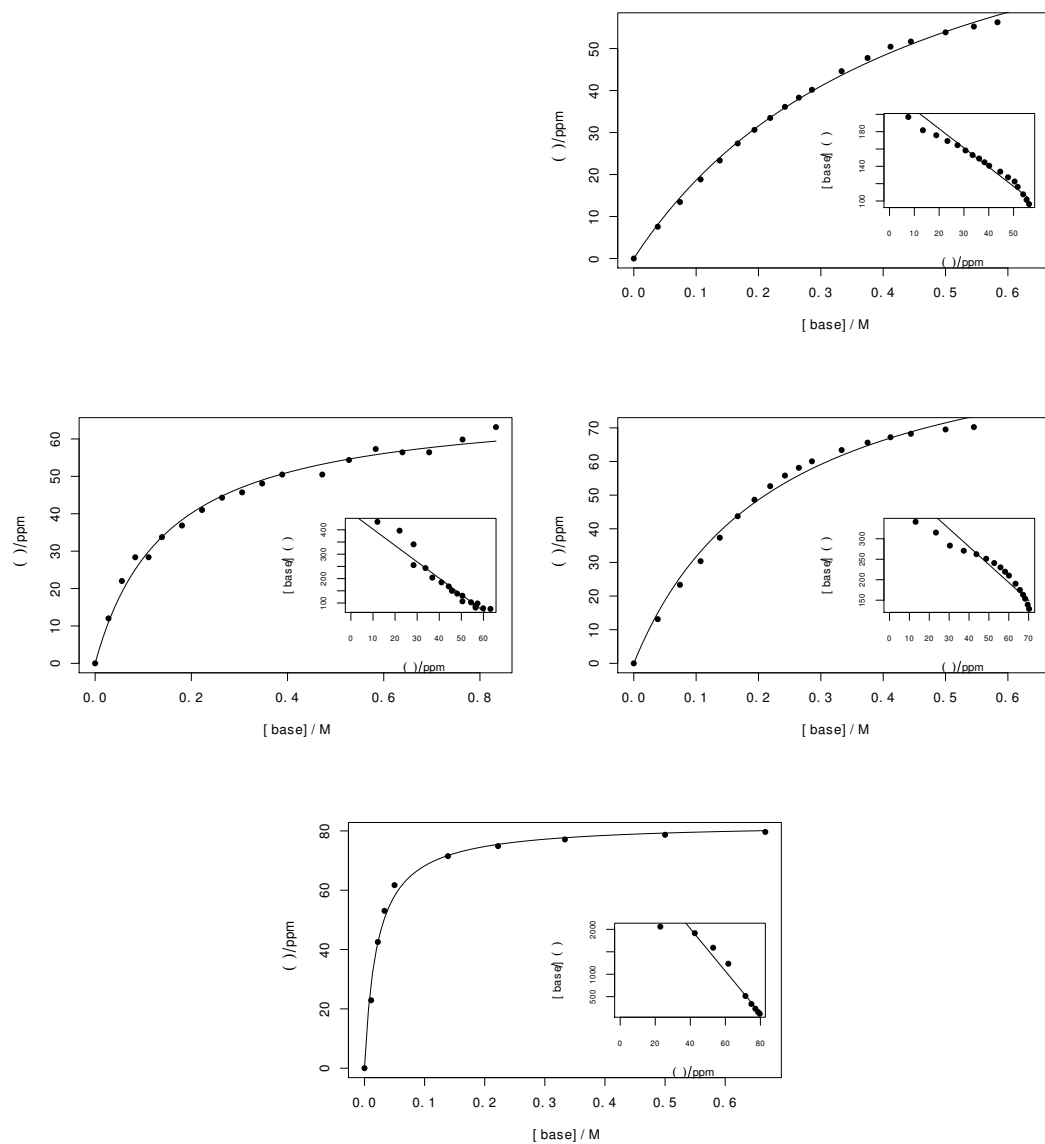


FIGURE 5.7: Binding isotherms for ebselen derivatives **1b**, **1k**, **1a**, **1g** and **1e** with DMAP.  
Scatchard plots are inset.

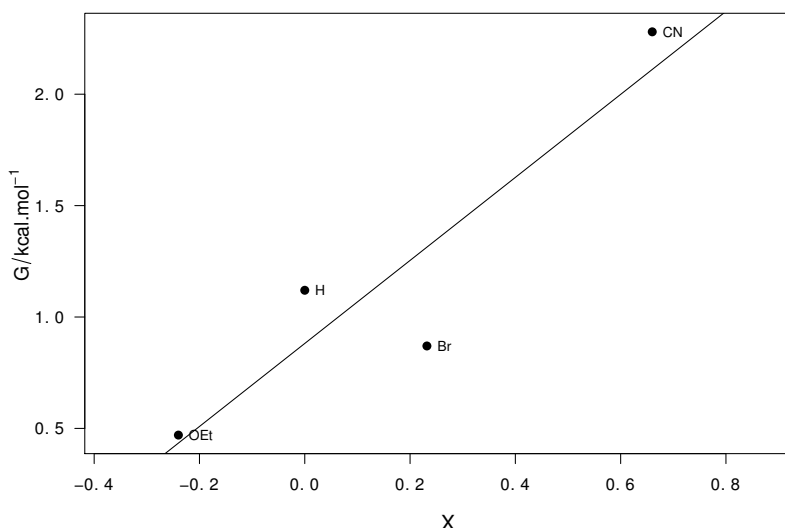


FIGURE 5.8: Hammett plot of binding energies between ebselen derivatives and DMAP, determined by  $^{77}\text{Se}$ -NMR titration. The line is described by the equation  $\Delta G = (0.88(21) + 1.86(57) \times \sigma_X) \text{ kcal} \cdot \text{mol}^{-1}$  ( $R^2 = 0.8437$ ).

UV-Vis spectroscopy presented a possible solution to both of these issues, with spectra collected in seconds even with extremely dilute solutions. Interactions which have a charge-transfer component (such as Ch-bonding) can give rise to strong absorbances attributable to the  $n \rightarrow \sigma^*$  transition.<sup>Blackstock1987</sup> However, we were unable to observe any evidence of such absorbances in our systems. This may be due to the fact that these Ch-bonds are primarily electrostatic in origin, or because the aromatic systems are already strongly absorbing, thus obscuring the charge-transfer band.

### 5.2.3 Ch-bonding in the gas phase

To complete our trifecta of experiments, we sought evidence that supports Ch-bonding in the gas phase. Broadly, we intended to isolate an ion corresponding to the complex by mass spectrometer, and subsequently fragment it by CID to regain the original species. Naturally, this requires that one (or both) of the components of the complex have a charge, so that it can be detected by the mass spectrometer. We initially injected an equimolar mixture of DMAP and ebselen **1a** in methanol, and isolated an ion of  $m/z$  398.08 a.m.u. However, this could be assigned to either the desired Ch-bonded complex, protonated at the carbonyl oxygen, or to a H-bonded complex. CID of this ion exclusively gave an ion of  $m/z$  123.09 a.m.u., corresponding to protonated DMAP (??). We interpreted this as evidence that we had formed the H-bonded complex, as migration of the proton on the timescale of a collision is unlikely, and the proton is most likely to remain with the more basic species in the H-bond. Furthermore, a  $\text{N}^+ - \text{H} \cdots \text{O}$

hydrogen bonds are very strong (in excess of 15 kcal/mol),<sup>Emsley1980</sup> which is likely to out compete Ch-bonding, with estimated bond enthalpies of < 10 kcal/mol in the gas phase.

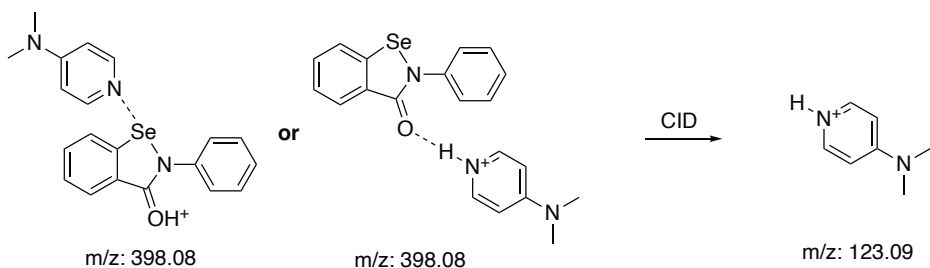


FIGURE 5.9: Dissociation of the complex **1a**·DMAP·H<sup>+</sup> under CID.

To circumvent this preferential formation of an H-bonded complex, we devised a system with no possibility of H-bonding. The isonicotinate ion was used as the Lewis base, and the complex isolated in the negative ion mode with m/z 397.01 a.m.u. CID of this ion exclusively gave a species of m/z 122.02 a.m.u., corresponding to isonicotinate (??). This provides strong evidence that a Ch-bonded complex is able to be formed in the gas phase.

FIGURE 5.10: Dissociation of the complex **1a**·isonicotinate under CID.

Using the technique of CID, one could imagine an experiment where such a Ch-bonded complex is fragmented with gradually increasing energy, and the yield of the product ion measured. This could theoretically be correlated with the gas phase bond energy. Indeed, this is the basis of the technique of Threshold CID (TCID) developed by Armentrout.<sup>Armentrout2003, Rodgers2000, Narancic2007</sup> Although the experiment is simple, the data analysis is not. This is due to the often poorly characterised energy distribution of the reactant ions, and vibrational energy redistribution in the products. These barriers are not insurmountable for simple systems (the technique has been successfully applied to metal complexes, and small non-covalent complexes), but in our moderately complex molecules with many vibrational modes, errors are likely to dominate any values extracted from the experiment. However, we present here a proof of concept experiment, which shows the decrease in reactant ion intensity and increase in product ion as CID energy is increased (??).

FIGURE 5.11: Rudimentary TCID experiment of **1a**·isonicotinate.

## 5.3 Supplementary materials

### 5.3.1 Synthetic procedures

#### 5.3.1.1 Preparation of bis(2-carboxyphenyl)diselenide ??

Anthranilic acid (3.460 g, 25.33 mmol) was dissolved in 1 M hydrochloric acid (80 mL) and cooled to 0°C. Sodium nitrite (1.751 g, 25.37 mmol) in water (40 mL) was then added drop-wise with stirring. The mixture was kept at 0°C.

Selenium (2.080 g, 26.34 mmol) was suspended in 1 M sodium hydroxide (120 mL) and degassed by repeatedly evacuating the flask until the solvent began to boil, then backfilling with N<sub>2</sub>. One grain of sodium borohydride was added under N<sub>2</sub> counter flow, followed by hydrazine hydrate (1.3 mL, 26 mmol). The mixture was heated until a red colour appeared, then cooled to 0°C.

The diazonium solution was neutralised with a solution of sodium hydroxide (4.320 g, 108.0 mmol) in water (20 mL), then added slowly to the cooled diselenide solution. Upon completion, the mixture was warmed to room temperature and stirred for 1 h, then neutralised with concentrated hydrochloric acid. The dense precipitate was separated by centrifuging, the supernatant decanted off, and the residue resuspended in hot methanol (300 mL). The methanol solution was subjected to hot filtration, and the orange filtrate concentrated to a volume of ~100 mL. This was cooled to -20°C, and the resulting crystals filtered off and dried. Recrystallisation from methanol gave **5** as a pale brown powder (1.8718 g, 37%).

<sup>1</sup>H NMR (400 MHz, *d*<sub>6</sub>-DMSO) δ ppm 7.29–7.38 (m, 1 H), 7.47 (t, *J*=7.43 Hz, 1 H), 7.66 (d, *J*=8.22 Hz, 1 H), 8.02 (d, *J*=7.43 Hz, 1 H) 13.70 (br. s., 1 H).

MS (ESI +ve) m/z 424.8806 (MNa<sup>+</sup>) C<sub>14</sub>H<sub>11</sub>O<sub>4</sub>Se<sub>2</sub><sup>+</sup> requires 424.8802 (Δ=0.941 ppm).

#### 5.3.1.2 Preparation of 2-(chlorocarbonyl)phenylselenyl chloride ??

Diselenide **5** (1.4758 g, 3.6881 mmol) was dissolved in thionyl chloride (10 ml) with 2 drops DMF and heated to reflux for 90 minutes. The excess thionyl chloride was distilled off under reduced pressure, and the solid residue extracted into dry hexane (30 mL). Evaporation of the solvent afforded **6** as yellow crystals (1.870 g, 100%), which were used without further purification or characterisation.

### 5.3.1.3 General procedure for the preparation of benzisoselenazolinone derivatives **1a**, **1d**, **1e**, **1f**, **1g**, **1h**, **1j** and **1k**

The appropriate amine (2.5 mmol) was dissolved in anhydrous acetonitrile (5 mL) and cooled to 0°C. To this was added triethylamine (1 mL, distilled from CaH<sub>2</sub>), followed by **6** (2.5 mmol) in a further 5 mL anhydrous acetonitrile. The mixture was stirred at room temperature for 2 h, then the solvent was removed under vacuum. The solid residue was triturated with water (5 mL) and 1 M hydrochloric acid to afford a friable solid, which was purified by recrystallisation from ethyl acetate at -20° C to afford the pure benzisoselenazolinone derivative.

**Ebselen 1a** Colourless crystals, m.p. 182.1–182.3°C ( $\alpha$  polymorph), 173.4–174.6°C ( $\beta$  and  $\gamma$  polymorph), xx%.

**4-Nitro ebselen 1d** Pale yellow crystals, 7%.

**4-Cyano ebselen 1e** Colourless crystals, m.p. 191°C (dec.), 61%.

**1e**·DMAP m.p. 157.6–160.2°C (DCM solvate, P2<sub>1</sub>/c).

**1e**·DMAP m.p. 176.0–178.8°C (non-solvate, Pbca).

**4-Trifluoromethyl ebselen 1f** Colourless crystals, m.p. 184.6–186.4°C, 14%.

**1f**·DMAP m.p. 178.3–179.6°C.

**4-Bromo ebselen 1g** Colourless crystals, m.p. 189.7–190.7°C, 18%.

**1g**·DMAP m.p. 162.3–164.4°C.

**4-Carboxyethyl ebselen 1h** Colourless crystals, m.p. 173.1–174.5°C 13%.

**1h**·DMAP m.p. 136.0–138.7°C.

**4-Methyl ebselen 1i** Light brown crystals, 58%.

**4-Methoxy ebselen 1j** Light brown crystals, 67%.

**4-Ethoxy ebselen 1k** Light brown crystals, 67%.

### 5.3.2 Crystallisation methods

Crystals of sufficient quality for x-ray diffraction analysis were grown by vapour diffusion of pentane into a dichloromethane solution ( $\sim 50$  mg/mL) of either the pure Ch-bond donor, or a 1:1 mixture of the donor and the appropriate Lewis base, with the following exceptions:

- the non-solvate of **1e**·DMAP was grown by slow evaporation from THF
- second polymorphs of **1k**·DMAP and **1j**·DMAP were grown from diffusion of pentane into diethyl ether.



## **Part II**

# **Chalcogen bonding at oxygen**



# Chapter 6

## Experimental evidence of Chalcogen bonding at oxygen.

This chapter was published in Chem. Commun., 13 Feb 2020. [Fellowes2020](#) \*

### 6.1 Abstract

An *o*-nitro-O-aryl oxime was observed to exhibit a short O···O contact, which exhibited characteristics consistent with a chalcogen bond. The O–N bond length of the oxime was appreciably longer than the expected value, and NBO calculations indicated the presence of a  $n(O) \rightarrow \sigma^*(O-N)$  orbital delocalisation. Topological analysis of the experimental electron density of two analogues shows the presence of a bond path between the two oxygen atoms, with  $\rho(r)$  and  $\nabla^2\rho(r)$  values consistent with an electrostatic interaction. Finally, electrostatic potential calculations indicate the presence of a  $\sigma$ -hole, the “smoking gun” indicating a Ch-bond. These results are unusual as oxygen is not typically considered to be a Ch-bond donor, especially in unactivated systems such as oximes.

### 6.2 Introduction

Chalcogen bonding (Ch-bonding) is a weak interaction of the broader family of  $\sigma$ -hole interactions, in which a chalcogen atom adopts some electrophilic character, allowing it to form a stabilised complex with a Lewis base. Much work has been directed towards applying

---

\*Compound numbering, section titles, and terminology have been updated to fit this thesis.

Ch-bonding principles to fields such as supramolecular engineering, catalysis, and anion sensing.<sup>Riwar2018, Mahmudov2017, Wonner2019, Ho2016, Kremer2016, Benz2017a</sup> Typically only the heavier chalcogen atoms form Ch-bonds (tellurium, selenium or sulfur, the latter having particular relevance to protein folding).<sup>Iwaoka2012</sup> The reason for this is that the electron cloud of the chalcogen must be distorted by an electron withdrawing substituent in order to form the electrophilic  $\sigma$ -hole. The larger and more polarisable the chalcogen atom, the more electrophilic the  $\sigma$ -hole, and the stronger the Ch-bond.<sup>Murray2008</sup>

Oxygen, as the second most electronegative element with its extremely low polarisability, is not considered to be a strong Ch-bond donor, although recent theoretical studies indicate that it can form a  $\sigma$ -hole in species such as  $\text{OF}_2$  and  $\text{FNO}_3$ .<sup>Varadwaj2019a, Varadwaj2019</sup> We report here a compound which appears to contain an intramolecular  $\text{O}\cdots\text{O}$  Ch-bond, which was synthesised and crystallised as part of an investigation into the Beckmann rearrangement.<sup>Yeoh2012</sup>

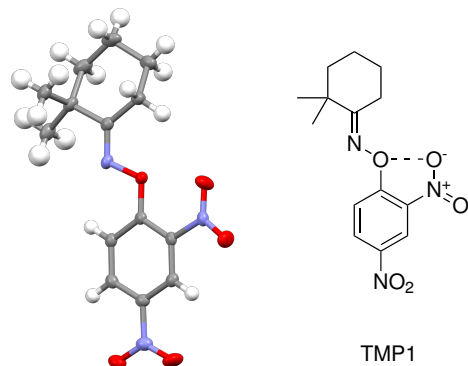


FIGURE 6.1: Oxime **7** displays a close  $\text{O}\cdots\text{O}$  contact, which has characteristics consistent with a Ch-bond.

## 6.3 Results and Discussion

The compound **7** is an *o*-nitro-O-aryl oxime, in which the nitro group constitutes the Ch-bond acceptor, and the oxime is the Ch-bond donor. Although the coplanar geometry of the oxime and nitro groups is expected on the grounds of favourable conjugation of these groups into the aromatic ring, there are a number of signs that suggest that there is an additional stabilising interaction between the groups, namely, the Ch-bond.

### 6.3.1 Structural effects attributable to the Ch-bond

Firstly, bond lengths measured from the crystal structure deviate somewhat from expected values. The  $\text{O}\cdots\text{O}$  Ch-bond distance was measured to be  $2.619(2)$  Å, which is well within the van der Waals radii of two oxygen atoms (3.04 Å).<sup>Bondi1964</sup> The O–N bond of the oxime is

TABLE 6.1: Selected geometric parameters of oximes **7**, ?? and ???. The two geometries in the asymmetric unit of ?? are indicated as ??a and ??b.

Compound	$r(O_1 \cdots O_2)$ Å	$r(N_1O_1)$ Å	$r(N_2O_2)$ Å	$\angle(O_2 \cdots O_1N_1)$ °	$\angle(C_1C_2N_2O_2)$ °
<b>7</b>	2.619(2)	1.489(2)	1.208(2)	161.80(8)	-3.5(2)
<b>8a</b>	2.5423(8)	1.4556(7)	1.2264(9)	160.56(5)	-0.7(1)
<b>8b</b>	2.5522(8)	1.4522(7)	1.223(1)	160.29(4)	-0.2(1)
<b>9</b>	2.6390(8)	1.4480(7)	1.2266(8)	148.60(4)	-30.94(8)

also lengthened appreciably. Comparisons with other O-aryl oximes are convoluted by the significant effect of the electronic properties of the phenyl ring on the oxime bond length. However, an expected value can be calculated using the acidity of the corresponding 2,4-dinitro phenol ( $pK_a = 5.91$ ) and the structural correlation given in equation ???. Yeoh2012, Socrates1970

$$r_{N-OR}(\text{\AA}) = 1.467 - (3.20 \times 10^{-3}) \times pK_a(\text{ROH}) \quad (6.1)$$

This gives an expected bond length of 1.448 Å versus the measured bond length 1.489(2) Å ( $\Delta = 0.041 \text{ \AA} = 13.7\sigma$ ).

This is consistent with the charge transfer model of Ch-bonding, as the lone pair of the nitro oxygen donor is delocalised into the  $\sigma^*(O-N)$  antibonding orbital, leading to a weakening and lengthening of this bond. Reed1988

### 6.3.2 NBO calculations

Secondly, DFT calculations were carried out on the solid phase geometry of **7** in order to ascertain the nature of the O · · · O close contact within the NBO (Natural Bond Orbital) and QTAIM (Quantum Theory of Atoms In Molecules) frameworks. Bader1991, NBO7 The two frameworks are complementary descriptions of bonding within molecules. The calculations were performed at the M06-2X/aug-cc-pVQZ level as implemented in the Gaussian16 suite. gaussian16, Zhao2008, Woon1995 This has been shown to give accurate densities for Ch-bonded complexes. Kim2019

It is customary to optimise structures so they are at a gas-phase minimum, ensuring that any derived energies, vibrational modes, and other quantities are reliable. In this case, however, we were unable to locate a minimum corresponding to the crystal geometry; the nitro group was forced out of the plane of the aryl ring, disrupting the requisite Ch-bond geometry. We note that the potential energy surface of this torsion is quite shallow, so the lack of a satisfactory minimum is likely due to the absence of crystal packing. Regardless, a thorough investigation was considered to be outside of the scope of this preliminary study, therefore solid phase geometries were used instead, with the caveat that certain quantities are likely to be unreliable.

The NBO calculations revealed the presence of a  $n(O) \rightarrow \sigma^*(O-N)$  orbital delocalisation, which is one criterion by which a Ch-bond can be defined.<sup>Pascoe2017</sup> As the geometry at which the NBO analysis was performed was not a gas phase minimum, orbital energies are inaccurate, and so the usual estimate of the strength of a delocalisation ( $E^2$ ) should not be used. We instead measure the magnitude of the delocalisation using the off-diagonal element of the Fock matrix  $F(i,j)$ , from which the energy  $E^2$  is calculated using equation ??.

$$E^2 = q_i \frac{F(i,j)^2}{\epsilon_j - \epsilon_i} \quad (6.2)$$

The value of  $F(i,j)$  for the  $n(O) \rightarrow \sigma^*(O-N)$  orbital delocalisation in **7** is 0.023 a.u., indicating a small delocalisation.

### 6.3.3 QTAIM analysis of electron density

Bader's Quantum Theory of Atoms In Molecules (QTAIM) describes bonding in terms of the observable quantity of electron density and its topology. We analysed the DFT density of oxime **7**, which revealed the presence of a bond path between the two oxygen atoms. Bond paths are associated with bond critical points (bcps), where the gradient vector of the electron density is zero.

The values of both the electron density  $\rho(r)$  and the Laplacian of the electron density  $\nabla^2\rho(r)$  at the bcp are diagnostic of certain types of bonds. Bcps with a small  $\rho(r)$  and positive  $\nabla^2\rho(r)$  (indicating local depletion of electron density at the bcp) are characteristic of ionic bonds or purely electrostatic interactions. The values of  $\rho(r)$  and  $\nabla^2\rho(r)$  respectively are 0.0161 and +0.0790 (in a.u.), suggesting this is primarily a closed shell electrostatic interaction, and that the NBO delocalisation, although present, is secondary.

These observations piqued our interest in the potential for Ch-bonding at oxygen, so we decided to extend our investigation to verify that this interaction was not simply a quirk of the initial oxime.

### 6.3.4 CSD search for similar structures

A search of the Cambridge Structural Database for *o*-nitro-O-aryl oximes afforded several results.<sup>CSD</sup> Structures HEPMEV, HUGSUX, and QOLXOE all contained similar motifs to **7**, with a nitro group approximately coplanar with an *ortho* oxime or oxime-like group.<sup>Saavedra2001, Kostyanovsky2002, Saavedra2006a</sup> Structure IQADOT was particularly interesting, as it contains two electronically similar oximes, only one of which has an *ortho* nitro group.<sup>Renaudet2003</sup> The difference in bond lengths between

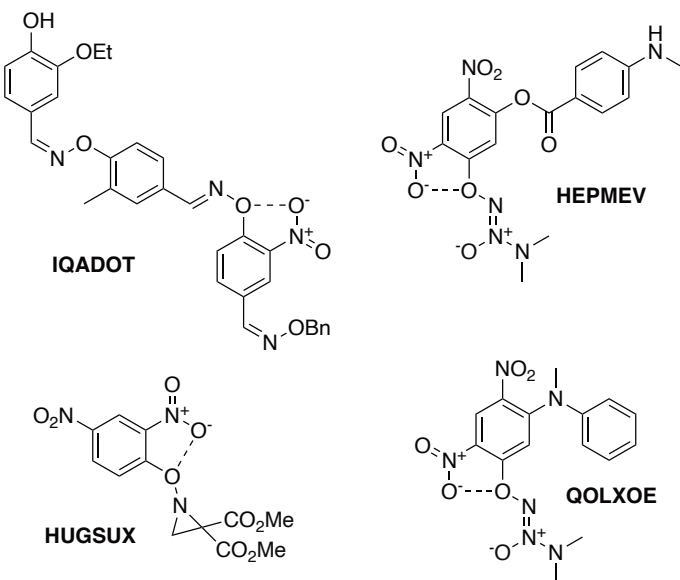
FIGURE 6.2: Structures of CSD matches for the *o*-nitro-O-aryl oxime motif.

TABLE 6.2: Selected geometric parameters of structures HEPMEV, HUGSUX, QOLXOE, and IQADOT

Compound	$r(O_1 \cdots O_2)$ Å	$r(N_1 - O_1)$ Å	$r(N_2 - O_2)$ Å	$\angle(O_2 \cdots O_1 - N_1)$ °	$\angle(C_1 - C_2 - N_2 - O_2)$ °
HEPMEV	2.554(5)	1.426(4)	1.222(4)	161.2(2)	-15.4(6)
HUGSUX	2.563(2)	1.461(2)	1.220(2)	158.4(1)	20.8(2)
QOLXOE	2.557(4)	1.419(4)	1.216(5)	158.7(2)	-10.9(6)
IQADOTa	2.532(2)	1.445(2)	1.207(3)	154.4(1)	-9.2(3)
IQADOTb	—	1.433(2)	—	—	—

them is significant ( $1.445(2)$  Å versus  $1.433(2)$  Å,  $\Delta = 0.012$  Å =  $6\sigma$ ), and the same trend is observed as in 7. Relevant structural parameters are given in table ??.

### 6.3.5 Analysis of analogues and determination of experimental electron density

Two analogues of oxime 7 (**8** and **9**, figure ??) were prepared, forming crystals which gave data of sufficient quality for multipole refinement, allowing us to analyse the experimental electron density as opposed to the calculated DFT density.<sup>Hansen1978</sup> This refinement was performed using the MoProSuite software package.<sup>Jelsch2005</sup> **8** crystallised in a similar coplanar geometry to 7, exhibiting a Ch-bond\*, while **9** displayed a torsion of the nitro group, disrupting the requisite geometry. This torsion can be attributed to crystal packing forces (taken to be worth 0.5–2 kcal/mol) disrupting this extremely weak interaction.<sup>Dunitz2009</sup>

\*The asymmetric unit contained two molecules, however both had similar geometries, and in the interests of simplicity values for only one molecule are presented.

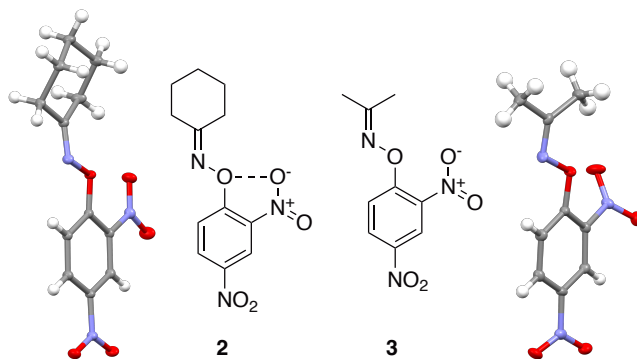


FIGURE 6.3: Oxime **8** adopts a similar conformation to **7**, while the nitro group of **9** is twisted, leading to poor alignment with the oxime.

The oxime bond lengths differ significantly between **8** and **9** (1.4556(7)–1.4522(7) versus 1.4480(7) Å,  $\Delta = 0.0042$  Å =  $6\sigma$ ), supporting the suggestion that the  $n(O) \rightarrow \sigma^*(O-N)$  orbital delocalisation plays a role in these Ch-bonds. NBO analysis of these geometries confirmed this, with  $F(i,j)$  values of 0.026 a.u. for **8**, and an absence of any delocalisation in **9**.

QTAIM analysis of the experimental density revealed the presence of a bond path and bcp in **8** but not in **9**, showing that there is indeed an interaction present when the geometry allows. In **8**, the values of  $\rho(r)$  and  $\nabla^2\rho(r)$  respectively are 0.018 and +0.094 (in a.u.), which agree well with the DFT values calculated for **7**, and are consistent with a closed-shell origin for the interaction (figure ??).

The NCI (non-covalent interaction) index is an extension of QTAIM, which characterises interactions based on the reduced density gradient and the second eigenvalue of the electron density Hessian.<sup>Johnson2010a</sup> This can be used to construct informative maps, showing surfaces where non-covalent interactions appear to be occurring. NCI maps were computed for **8** and **9** based on the experimental electron density, and these are shown in figure ??.

To provide further evidence for the interaction, we took advantage of the fact that derivative **9** does not display a Ch-bond, and searched for a  $\sigma$ -hole in the experimental electron density. Due to the crowded surroundings of the oxime group, we were unable to visualise the 0.001 a.u. isosurface as would be typical for ESP analysis. The extension of the oxime bond (therefore, the  $\sigma$ -hole) was simply not visible. We instead mapped the electrostatic potential onto intersecting planes through the oxime bond, which clearly showed a positive region along the extension of this bond consistent with a  $\sigma$ -hole (figure ??).

When investigating such weak interactions as these, it is important to consider the limitations of each method of analysis. For example, the presence of a topological bond path within the QTAIM framework does not necessarily imply the presence of an attractive bonding interaction. It may simply represent the inevitable consequence of placing two electron clouds in close proximity.<sup>Spackman1999, Gatti2005, Bader2009, Cerpa2008, Cerpa2009</sup> However, in this case, the NBO

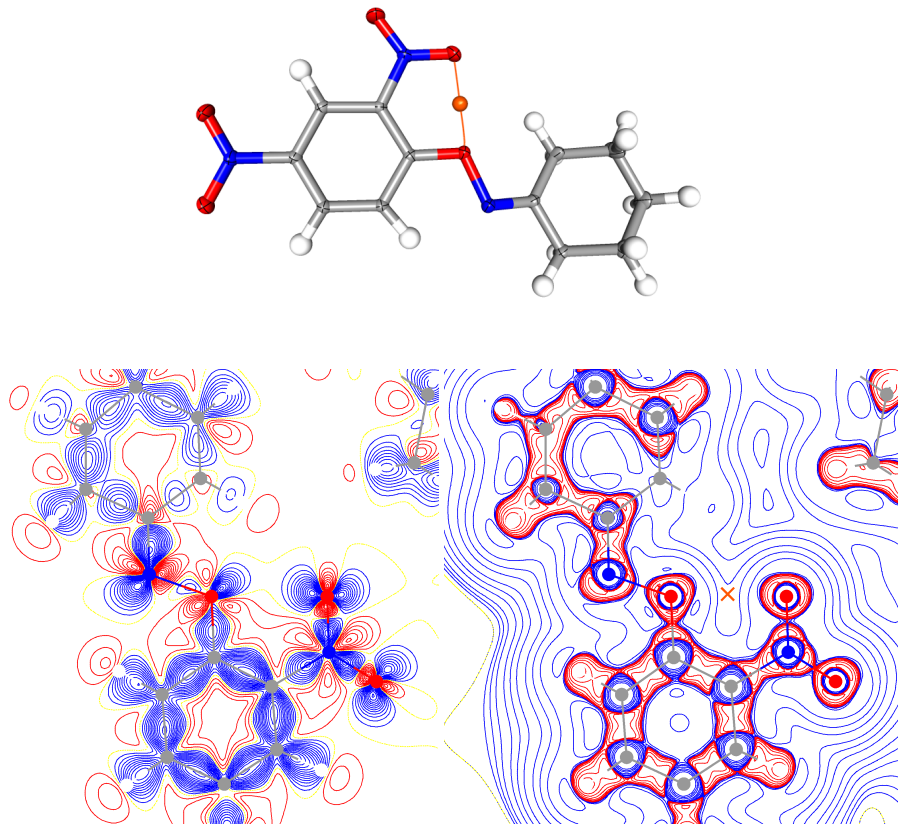


FIGURE 6.4: Deformation and Laplacian maps of the experimental electron density for **8**. Negative values depicted by red contours, and positive by blue. Above is shown the bond path and bcp in orange.

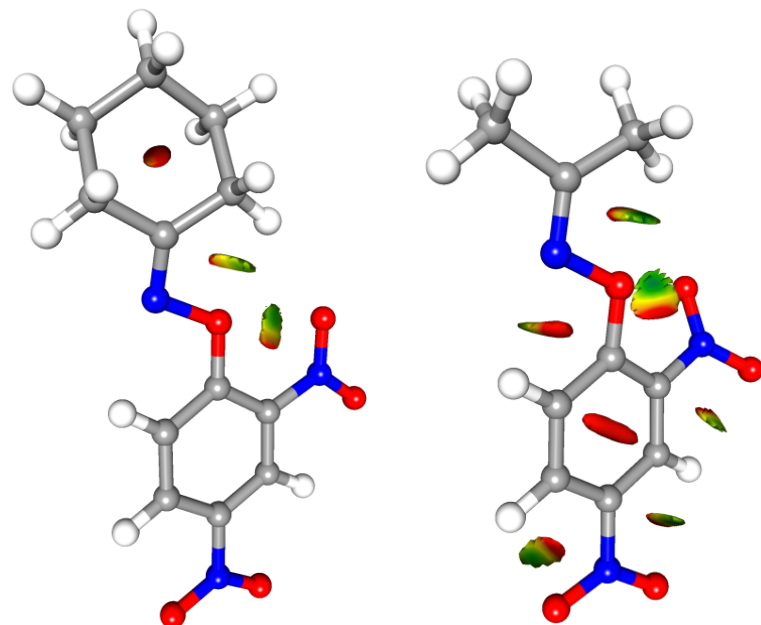


FIGURE 6.5: NCI maps for **8** and **9**. Positive values (non-bonding) are shown in red, and negative values (attractive) are shown in blue.

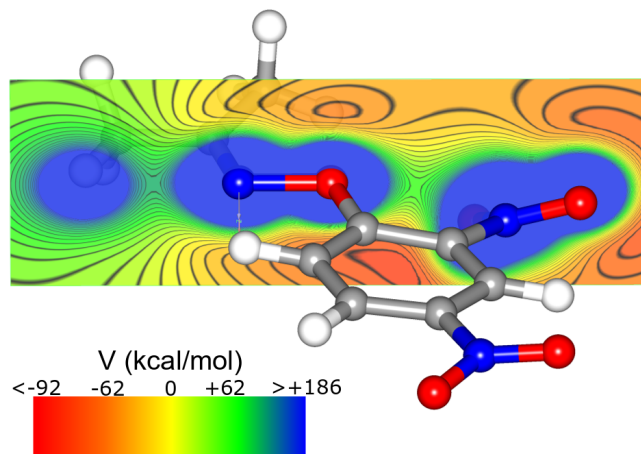


FIGURE 6.6: Electrostatic potential mapped onto a plane through the oxime bond. The  $\sigma$ -hole is visible as a green (positive ESP) elongation of the nuclear potential towards the nitro group to the right. Note that the oxime nitrogen also displays a  $\sigma$ -hole to the left.

calculations, QTAIM and electrostatic potential analysis of the experimental electron densities are all consistent with the statistically significant lengthening of the oxime N–O bond, and all signs point toward a true  $\sigma$ -hole interaction.

We believe this is the first documented experimental evidence of a  $\sigma$ -hole interaction at oxygen, and it is remarkable that it occurs in such air- and water-stable molecules as these oximes. We therefore challenge the consensus that Ch-bonding can only occur at highly activated oxygen atoms, and suggest that there may be implications when considering the reactivity of trace molecules such as peroxides, and nitric and nitrous oxides in biological systems.

## 6.4 Supplementary material

### 6.4.1 Synthesis

#### 6.4.1.1 Preparation of *O*-(2,4-dinitrophenyl) oximes **8** and **9**

Cyclohexanone oxime (556.8 mg, 4.920 mmol) and sodium hydride (60% in mineral oil, 249.5 mg, 6.237 mmol) were dissolved in anhydrous THF (10 mL) and stirred for 5 minutes. This was then added to a solution of 2,4-dinitro-1-fluorobenzene (950.6 mg, 5.108 mmol) in a further 10 mL anhydrous THF. This was stirred for 1 h at room temperature, then diluted with water (100 mL) and extracted with ethyl acetate ( $2 \times 30$  mL). The combined organic phases were washed with brine (30 mL), dried ( $\text{MgSO}_4$ ) and evaporated to afford **8** as a waxy pale yellow solid (895.1 mg, 65%, m.p. 100.2–100.9° C).

Acetone oxime **9** was isolated as a pale yellow powder, yield 72%, m.p. 88.5–88.9° C.

Crystals suitable for x-ray diffraction analysis were grown by slow diffusion of pentane into a saturated solution of the compound in dichloromethane.

### 6.4.2 Crystallographic data

Crystal Data for **7** C<sub>14</sub>H<sub>17</sub>N<sub>3</sub>O<sub>5</sub> ( $M = 307.30$  g/mol): monoclinic, space group P2<sub>1</sub>/c (no. 14),  $a = 7.17630(10)$  Å,  $b = 28.9373(4)$  Å,  $c = 7.06700(10)$  Å,  $\beta = 92.1860(10)^\circ$ ,  $V = 1466.48(4)$  Å<sup>3</sup>,  $Z = 4$ ,  $T = 130.15$  K,  $\mu(\text{Cu K}\alpha) = 0.902$  mm<sup>-1</sup>,  $D_{\text{calc}} = 1.392$  g/cm<sup>3</sup>, 10358 reflections measured ( $12.234^\circ \leq 2\theta \leq 158.922^\circ$ ), 2902 unique ( $R_{\text{int}} = 0.0231$ ,  $R_{\text{sigma}} = 0.0149$ ) which were used in all calculations. The final  $R_1$  was 0.0472 ( $I > 2\sigma(I)$ ) and  $wR_2$  was 0.1242 (all data).

Crystal Data for **8** C<sub>12</sub>H<sub>13</sub>N<sub>3</sub>O<sub>5</sub> ( $M = 279.25$  g/mol): monoclinic, space group P2<sub>1</sub> (no. 4),  $a = 6.66740(10)$  Å,  $b = 16.3925(3)$  Å,  $c = 11.6108(2)$  Å,  $\beta = 101.0310(10)^\circ$ ,  $V = 1245.56(4)$  Å<sup>3</sup>,  $Z = 4.00$ ,  $Z' = 2.00$ ,  $T = 100(1)$  K,  $\mu(\text{Mo K}\alpha) = 0.118$  mm<sup>-1</sup>,  $D_{\text{calc}} = 1.489$  g/cm<sup>3</sup>, 51580 reflections measured ( $7.016^\circ \leq 2\theta \leq 102.638^\circ$ ), 25111 unique ( $R_{\text{int}} = 0.0214$ ,  $R_{\text{sigma}} = 0.0317$ ) which were used in all calculations. The final  $R_1$  was 0.0409 ( $I > 2\sigma(I)$ ) and  $wR_2$  was 0.1153 (all data). Flack parameter = 0.32(14).

Crystal Data for **9** C<sub>9</sub>H<sub>9</sub>N<sub>3</sub>O<sub>5</sub> ( $M = 239.175$  g/mol): orthorhombic, space group P2<sub>1</sub>2<sub>1</sub>2<sub>1</sub> (no. 19),  $a = 5.49110(10)$  Å,  $b = 10.5173(2)$  Å,  $c = 18.2619(3)$  Å,  $V = 1054.65(3)$  Å<sup>3</sup>,  $Z = 4$ ,  $T = 100.00(10)$  K,  $\mu(\text{Mo K}\alpha) = 0.125$  mm<sup>-1</sup>,  $D_{\text{calc}} = 1.506$  g/cm<sup>3</sup>, 24292 reflections measured ( $5.908^\circ \leq 2\theta \leq 102.41^\circ$ ), 10696 unique ( $R_{\text{int}} = 0.0224$ ,  $R_{\text{sigma}} = 0.0326$ ) which were used in all calculations. The final  $R_1$  was 0.0378 ( $I > 2\sigma(I)$ ) and  $wR_2$  was 0.1032 (all data). Flack parameter = -0.02(19).



# Chapter 7

## Further investigations into Ch-bonding at oxygen.

### 7.1 Introduction

Following our initial discovery of unconventional Ch-bonding in *o*-nitro-O-aryl oximes, we sought to establish a structural correlation to bring it in line with more typical Ch-bonding. To this end, we attempted to manipulate the electron density on both Ch-bond donor and acceptor, and measure the structural changes that result. We believed that this was important to further substantiate our claim of Ch-bonding being a significant stabilising factor.

### 7.2 Results and discussion

#### 7.2.1 CSD search

Since the publication of our first report, we became aware of other apparent Ch-bonds involving oxygen, although they were not initially recognised as such. Consistent with expectations, they both involve oxygen atoms bonded to nitrogen. The packing of bis-furoan **XERPOA** is directed by intermolecular O · · · O Ch-bonds, although the structure is also stabilised by the Rb<sup>+</sup> counterion (not shown).<sup>Gilardi2005</sup> The classic oxaziridine electrophilic oxygen species **FIVJEZ** also exhibits a Ch-bond between the oxygen and the chlorine on an adjacent molecule.<sup>Malpezzi1987</sup> Both structures are shown in figure ??.

The presence of these *intermolecular* Ch-bonds is

encouraging, as it indicates that oxygen-based Ch-bonds are competitive with other interactions, and therefore likely to be of interest for the purposes of drug discovery or crystal engineering. [Taylor2020IdentifyingCompetitive](#)

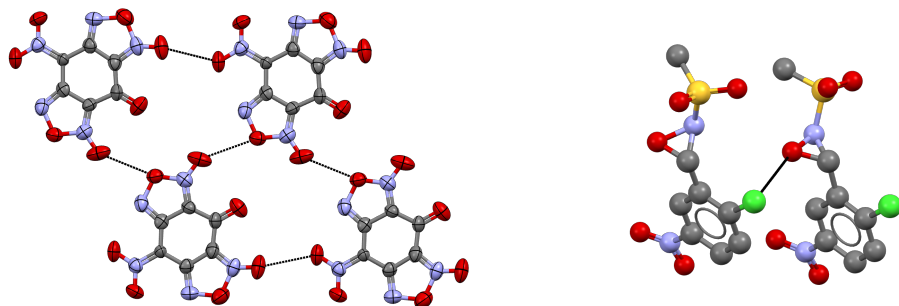


FIGURE 7.1: Structures of **XERPOA** and **FIVJEZ** with Ch-bonds indicated by black dotted lines.

## 7.2.2 Structural studies of analogues

As the Ch-bond appears to be a primarily electrostatic interaction, it follows that the strength of the Ch-bond will be correlated with the difference in electrostatic potential between the donor and acceptor.

To test this, we synthesised a series of analogues which varied in the electron density at the nitro and oxime groups. We first attempted to investigate the effects of substantially increasing the electrophilic character of the oxime oxygen, by starting from an electron-poor oxime. Initial efforts to form hexafluoroacetone oxime (from hexafluoroacetone deuterate and hydroxylamine) were hampered by the fact that the dehydration equilibrium strongly favours the hemiaminal form (figure ??).

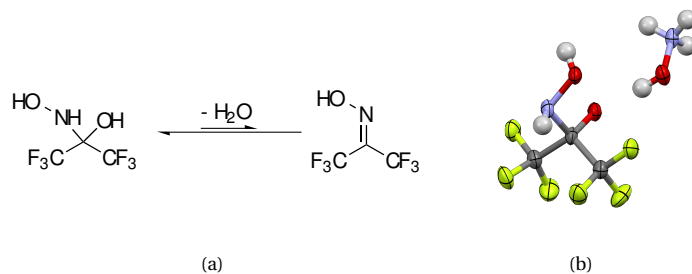


FIGURE 7.2: The dehydration of electron poor hemiaminals is strongly disfavoured. Instead, the hydroxylammonium salt was isolated as a crystalline solid.

Various methods to remove the water failed, so we persisted with the cyclohexanone oxime (as these derivatives had been shown to crystallise well) and instead modified the electronic properties of the aryl group.

We first prepared the derivative lacking a nitro group at the 4 position of the aryl ring (compound **10**). Removing the electron-withdrawing nitro group at this position make the oxime oxygen somewhat more electron rich, while having a negligible effect on the Lewis basicity of the other nitro group. This has the effect of "switching off" the Ch-bond, by reducing its strength relative to other effects. Indeed, this can be observed in the crystal structure (figure ??), where the nitro group adopts a twisted orientation similar to that of **9**.

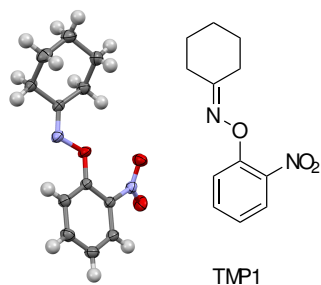


FIGURE 7.3: The structure of **10** exhibits a torsion of the nitro group, suggesting the Ch-bond is too weak to overcome the exchange repulsion between the oxygens.

With this encouraging result, we sought to switch the Ch-bond back on again by improving the donor ability of the *o*-nitro group. This was accomplished by introducing an electron donating group at the 5 position of the ring, which has the effect of increasing electron density at the *o*-nitro group while leaving the oxime relatively unchanged. Compounds **11** and **12** were prepared, both of which had similar electronic properties (?? and ??).

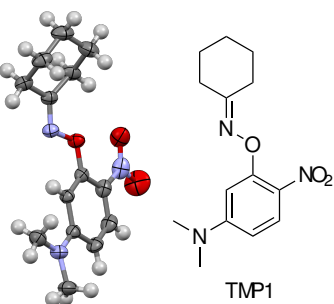


FIGURE 7.4: The structure of **11** features a coplanar nitro group. The increased basicity of the nitro oxygen is sufficient to overcome the repulsion.

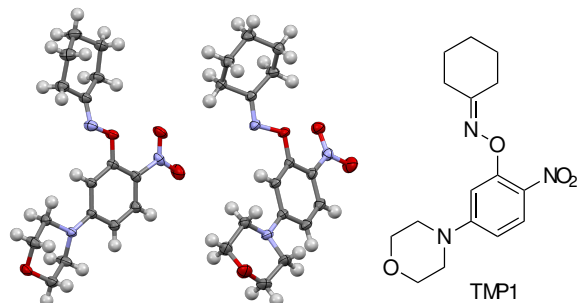


FIGURE 7.5: The structure of **12** also features coplanar nitro groups. There are two molecules in the asymmetric unit, and both are shown.



## **Part III**

# **Applications of Ch-bonding**



## **Chapter 8**

# **Thermal conversion of a pyridine solvate to a de-solvate facilitated by rearrangement of chalcogen bonds. The solvate and non-solvate structures of N-(2-nitro-4-(3-oxobenzo[*d*][1,2]selenazol-2(3*H*)-yl)phenyl)picolinamide.**

This chapter was published in Cryst. Eng. Comm., 26 May 2020. [Fellowes2020a](#) \*

### **8.1 Abstract**

The pyridine solvate of benzisoselenazolinone **13**·pyridine is characterised by planar sheets of the benzisoselenazolinone **13** pierced by channels of pyridine molecules at an angle of 133°, the pyridine molecules are held in place by N ··· Se chalcogen bonding to the isoselenazolinone moiety. These channels, which extend through the structure to the surface of the crystal,

\*Compound numbering, section titles, and terminology have been updated to fit this thesis.

provide a means for escape of pyridine from the lattice when the crystal is heated to ca. 100°C. Upon loss of the pyridine from these channels the remaining molecules undergo rearrangement to fill the space and in doing so the N ··· Se chalcogen bond in **13**·pyridine is replaced by a C=O ··· Se chalcogen bond to give the non solvate **13**(ex.DMF). The geometry of the chalcogen bond requires that the two benzisoselenazolinone ring systems which are essentially coplanar in **13**·pyridine twist by an angle of 138° resulting in the formation of highly corrugated sheets in the non solvate.

## 8.2 Introduction

Chalcogen bonding (Ch-bonding) is an attractive non-covalent interaction between a Lewis base and a chalcogen atom bearing an electron withdrawing substituent (X) (??),<sup>Vogel2019, Bleiholder2006, Garrett2015a</sup> it is directional and has a strength similar to hydrogen bonding. Chalcogen bonding has applications in fields as diverse as medicinal chemistry,<sup>Beno2015, Clark2007, Hudson2016, Iwaoka2002, Reid2014</sup> anion sensing,<sup>Lim2017, Garrett2016, Borissov2019</sup> materials chemistry,<sup>Biot2018</sup> supramolecular chemistry,<sup>Chen2018, Ho2016, Gleiter2018, Bleiholder2006, Huynh2017, Gleiter2003</sup> and catalysis.<sup>Wang2020</sup> In medicinal chemistry the chalcogen bond is considered as an isostere to N–H ··· A hydrogen bonding (??), this property is currently being exploited in the development of new pharmaceuticals.

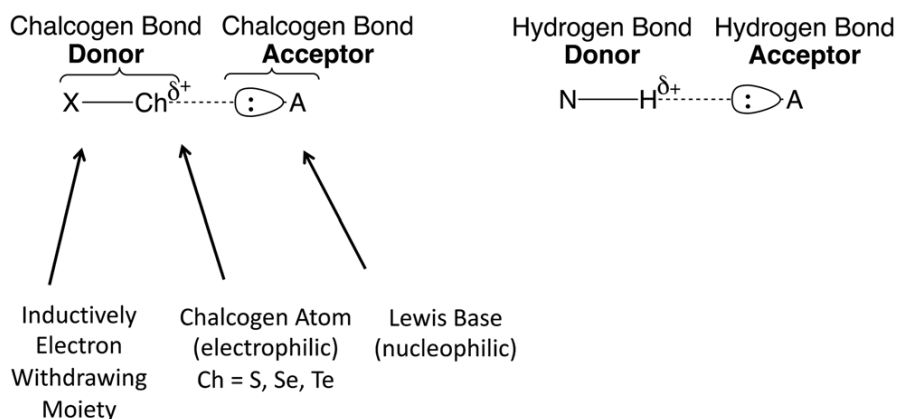


FIGURE 8.1: Chalcogen bonding model, and similarity to H-bonding.

The mechanism of chalcogen bonding is believed to involve both electrostatic and orbital interactions with dispersion being a lesser contributor. The electrostatic component involves attraction between the Lewis base and a positively charged  $\sigma$ -hole which is generated along the extension of the Ch–X bond due to polarisation of the bonding orbital, while the orbital interaction component involves mixing between the occupied lone pair orbital of the Lewis base and the vacant  $\sigma_{\text{Ch}-\text{X}}^*$  bond on the chalcogen, both these interactions account for the directionality of this interaction to different extents. Whereas the electrostatic  $\sigma$ -hole

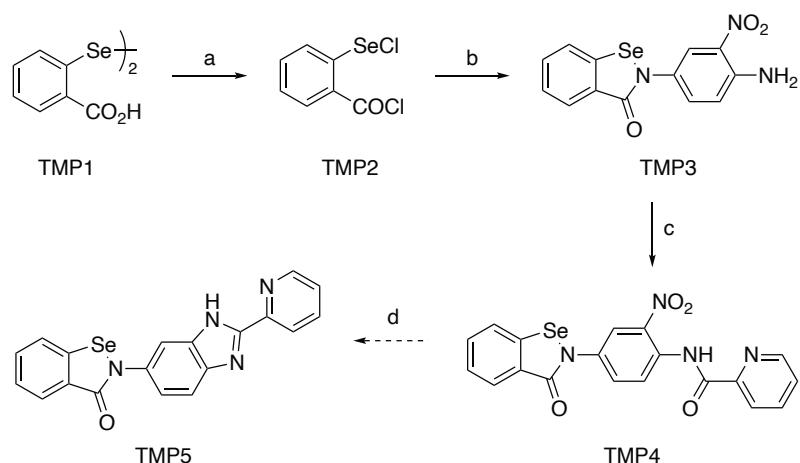
interaction is believed to be the main contributor to the closely related halogen bonding interactions,<sup>Prasang2009, Sarwar2010, Beale2013, Aakeroy2013, Goud2016, Stone2013</sup> significant lengthening of the Ch–X bond observed in the crystal structures of a number of chalcogen bonded systems is suggestive of a significant charge-transfer component to this interaction.<sup>Fellowes2019, Pascoe2017</sup>

## 8.3 Results and discussion

As part of our efforts towards a chalcogen-bonding based DNA minor-groove binding agent we required the benzisoselenazolinone **13**, which we proposed to cyclise to the benzimidazole-substituted benzisoselenazolinone **14**, an analog to the Hoechst-type DNA-binding bisbenzimidazoles.<sup>Loewe1974, Pjura1987, Martin2004</sup>

### 8.3.1 Synthesis

The benzisoselenazolinone **13** was prepared from the diselenide **5** by conversion to the bis-electrophilic selenium reagent **6**,<sup>Lesser1924</sup> followed by condensation with 2-nitro-1,4-benzenediamine to give the benzisoselenazolinone **15**, which was then coupled to picolinic acid via a Yamaguchi intermediate (??).



SCHEME 8.1: Synthesis of precursor **13**. a)  $\text{SOCl}_2$ , b) 2-nitro-1,4-benzenediamine,  $\text{Et}_3\text{N}$ , THF, c) Picolinic acid, TCBC/DMAP,  $\text{Et}_3\text{N}$ , d)  $[\text{H}], \text{H}^+$ .

### 8.3.2 Structural characterisation

Benzisoselenazoline **13** was found to be of low solubility in most organic solvents, but very small orange needles were obtained from slow evaporation from dimethylformamide. The crystal structure obtained using data collected at the Australian Synchrotron was that of a

non-solvate form, referred to herein as **13(ex.DMF)** in the orthorhombic space group Pbca. A thermal ellipsoid plot for **13(ex.DMF)** is presented in ??.

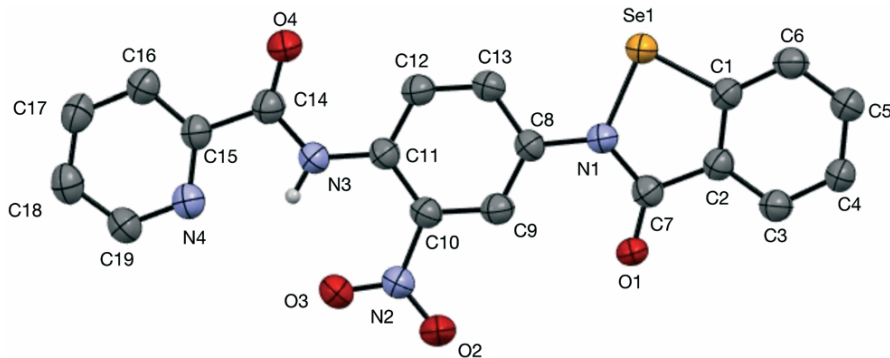


FIGURE 8.2: Thermal ellipsoid plot of **13(ex.DMF)**. Ellipsoids are at the 50% probability level.

The crystal packing in **13(ex.DMF)** is characterised a number of non-covalent interactions including  $\pi$ -stacking which forms columns extending down the *b* axis between molecules of **13** related by the *b* glide plane (??). The planes defined by the central aromatic ring C8-C13 are inclined at an angle  $10.3(2)^\circ$  to the adjacent  $\pi$ -stacked molecule, with a centroid (C8-C13) plane distance of  $3.414(4)$  Å and a centroid–centroid distance of  $3.786(4)$  Å representing a slip distance of  $1.636$  Å.

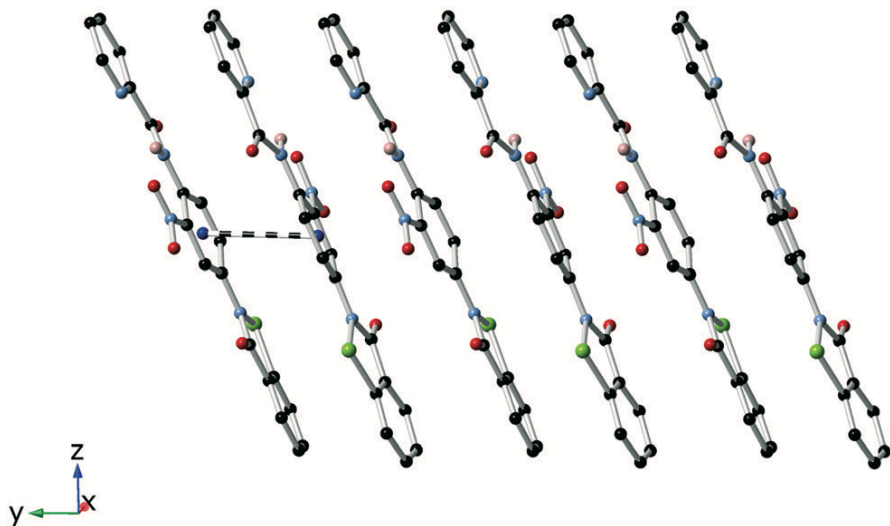


FIGURE 8.3: Offset  $\pi$ -stacking of **13(ex.DMF)** extending down the *b*-axis. The centroid-centroid distance is  $3.786(4)$  Å.

Adjacent  $\pi$ -stacked columns are held together by chalcogen bonding interactions between the isoselenazolinone amide carbonyl oxygen and the selenium atom in the heterocyclic ring forming chains generated by the *a*-glide plane extending down the *a*-axis. The  $O \cdots Se$  distance is  $2.659(3)$  Å and the  $O \cdots Se - N$  angle is  $173.6(2)^\circ$ . The angle between the planes defined by the benzisoselenazolinone rings in the chalcogen bonded pairs is  $138.8^\circ$ . A coplanar arrangement is presumably disfavoured as this would result in severe steric clashes with the

C5 of the benziselenazolinone ring. Similar O ··· Se chalcogen bonding interactions have been observed in other benziselenazolinone derivatives related to the drug ebselen with comparable geometries.<sup>Fellowes2019, Thomas2015, Bhabak2007, Piatek1995</sup> The N3–H3 group which is flanked by the pyridine nitrogen and the nitro group engages in intramolecular N–H ··· N and N–H ··· O hydrogen bonds, but is not involved in any significant intermolecular interactions (??, ??, ??).

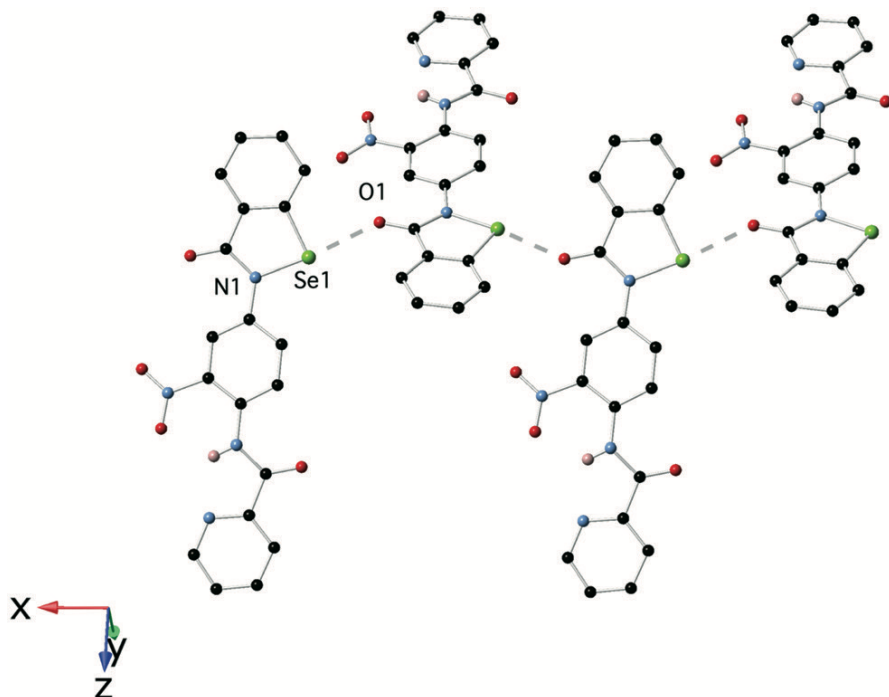


FIGURE 8.4: O ··· Se chalcogen bonding interactions in **13**(ex.DMF).

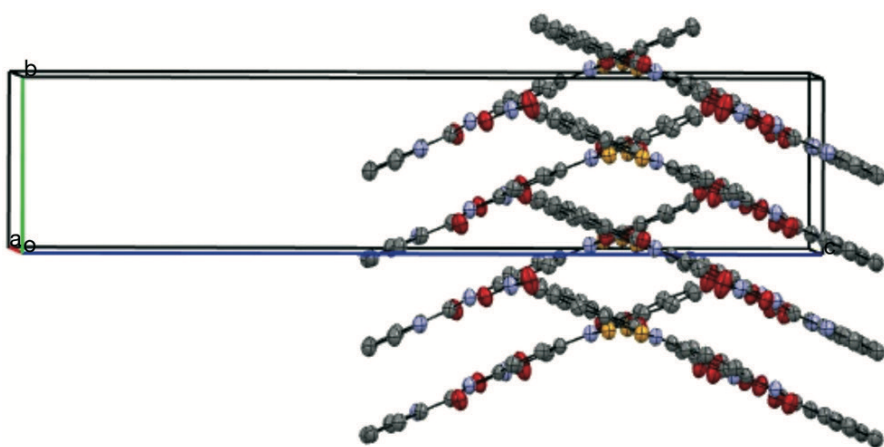


FIGURE 8.5: 2-D layers of **13**(ex.DMF)  $\pi$ -stacking extends along the *b*-axis while the Se ··· O chalcogen bond interactions extend down the *a*-axis.

The combination of the  $\pi$ -stacking and chalcogen bonding generates a 2-dimensional network lying parallel to the *ab* plane. These layers are extended into 3-dimensions by weaker Van-der Waals contacts between molecules related by the *c* glide.

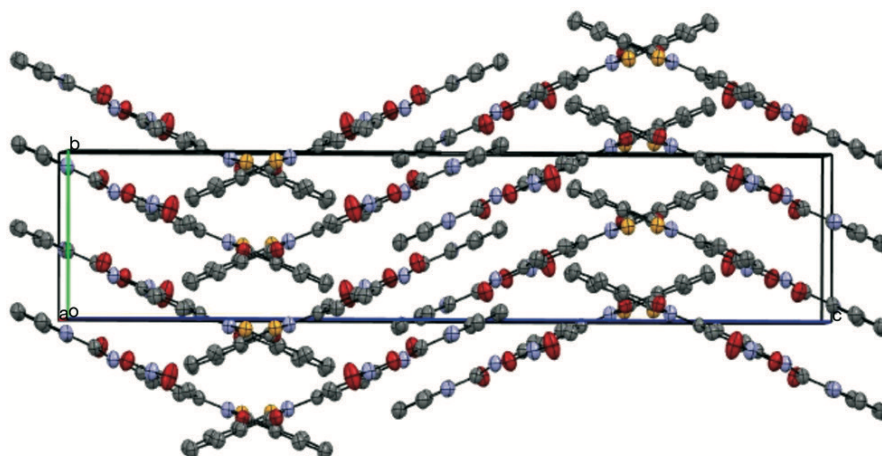


FIGURE 8.6: Extension of the 2-D layers of **13**(ex.DMF) into 3-D by van der Waals interactions.

Crystallisation of benziselenazolinone **13** from pyridine gave rise to orange needles which were found to diffract well on the home-source diffractometer. The structure solved in the monoclinic space group  $P\bar{c}$  and was found to be a pyridine solvate, herein labelled **13**·pyridine. The structure of **13**·pyridine is presented in ?? and shows that the pyridine solvate forms a  $N \cdots Se$  chalcogen bond between the pyridine solvent molecule and the isoselenazolinone moiety. The  $N5 \cdots Se1$  distance is  $2.466(5)$  Å, the  $N5 \cdots Se1-N1$  angle is  $173.2(2)^\circ$ , and the angle between the plane of the coordinated pyridine ring and the benziselenazolinone ring is  $89.2(1)^\circ$ . This geometry compares with previously reported chalcogen bonded adducts involving dimethylaminopyridine with simple benziselenazolinones.<sup>Fellowes2019</sup> It is interesting to note that upon formation of the chalcogen bond to pyridine, there is a significant lengthening of the  $Se1-N1$  bond distance from  $1.910(3)$  Å in **13**(ex.DMF) to  $1.945(5)$  Å in **13**·pyridine, which is consistent with the expected structural effects arising from the charge-transfer component of chalcogen-bonding.<sup>Fellowes2019, Pascoe2017</sup>

Molecules of **13** assemble into planar sheets lying parallel to the  $(\bar{1}04)$  plane, the distance between these sheets as defined by the distance between the centroid of the atoms C8–C13 and the adjacent plane is  $3.336$  Å while the centroid-centroid distance is  $4.973$  Å representing a slippage of  $3.688$  Å (??, ??). The parallel sheets of molecules of **13** are pierced by channels of chalcogen bonded pyridine molecules which run parallel to the  $a$ -axis at an angle of approximately  $133^\circ$  to the plane.

### 8.3.3 Variable temperature studies

Thermal gravimetric analysis of the pyridine solvate **13**·pyridine was conducted on a Mettler TGA/SDTA851 apparatus in  $40 \mu\text{L}$  aluminium crucibles. A mass loss of  $15.04\%$  occurred between  $90$ – $110^\circ\text{C}$  corresponding to the loss of the pyridine solvate (calc.  $15.26\%$ ) followed by

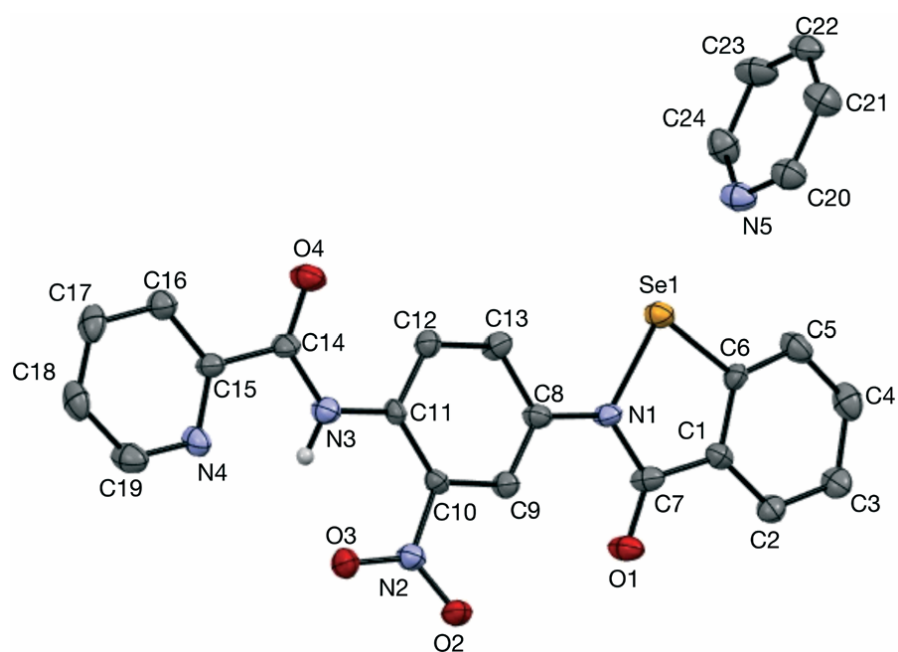


FIGURE 8.7: Thermal ellipsoid plot of **13**·pyridine. Ellipsoids are at the 50% probability level.

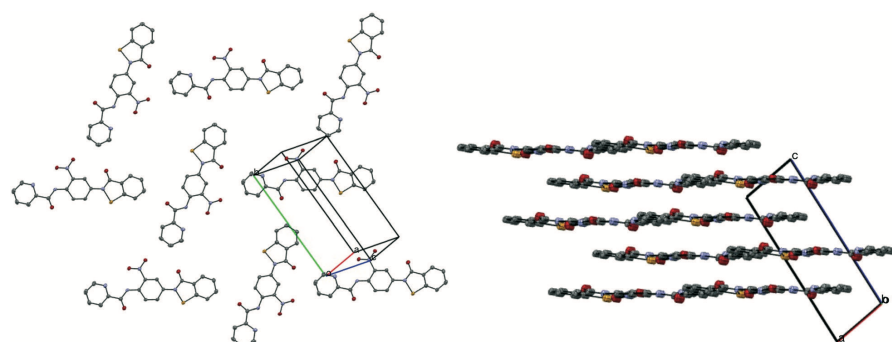


FIGURE 8.8: Sheets of compound **13** viewed from orthogonal and parallel directions. Pyridine solvate has been excluded.

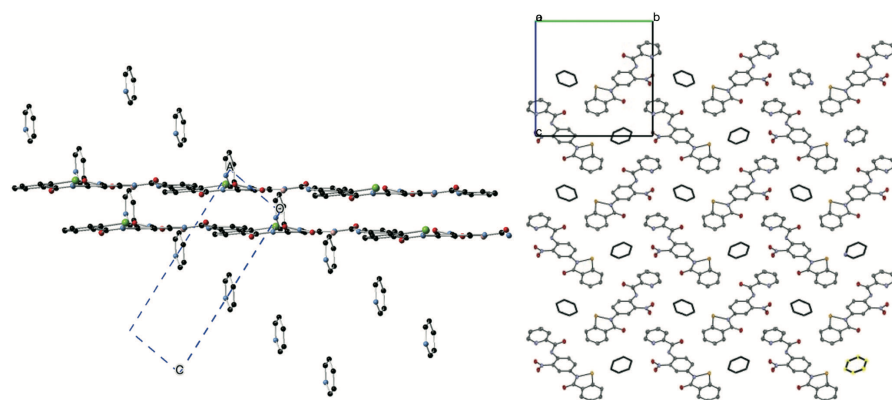


FIGURE 8.9: Two orthogonal views of parallel sheets of compound **13**, pierced by channels of pyridine molecules running parallel to the *a*-axis.

a second loss of 24.73% between 300–360°C which is consistent with the loss of 121 a.m.u. very likely associated with the Pyr-C(O)NH moiety (??).

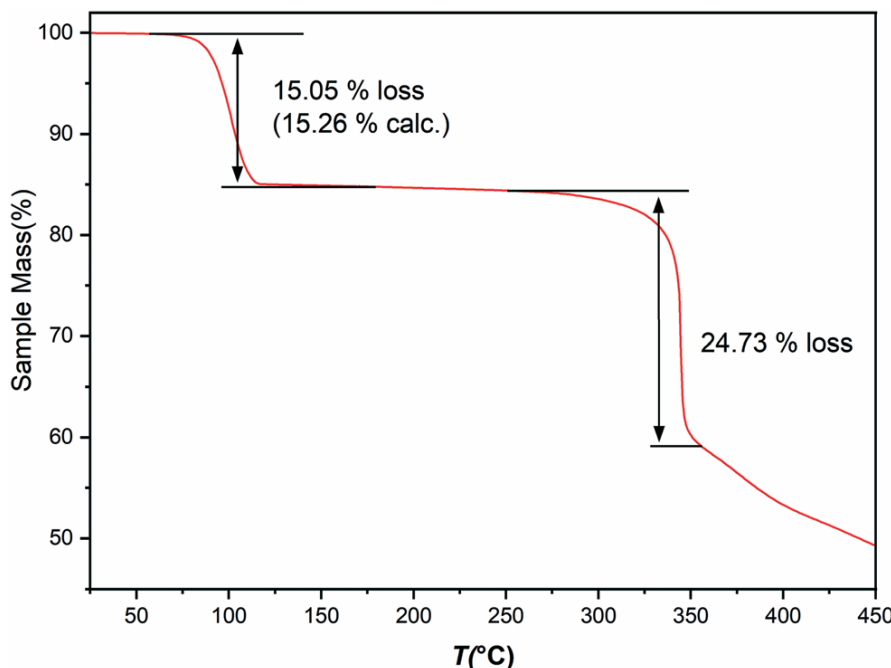


FIGURE 8.10: TGA analysis of **13**·pyridine

The observation that both the non-solvate **13**(ex.DMF) and **13**·pyridine had the same melting point (experimental section below) intrigued us to establish whether desolvation of **13**·pyridine which occurs between 90–120°C results in conversion to non-solvate **13**(ex.DMF). Thus we carried out variable temperature powder X-ray diffraction measurements on **13**·pyridine from -173°C to 117°C. The resulting diffractograms are shown in ??.

From 87°C to 117°C when pyridine is known to be lost from the sample from the TGA analysis, there is a smooth change from one crystalline phase to another. Furthermore comparison of the final diffractogram obtained after being kept at 117°C for 10 minutes very closely matches the calculated powder pattern for the non-solvate **13**(ex.DMF) suggesting the transformation from **13**·pyridine into **13**(ex.DMF). The same experiment was applied to a single crystal of **13**·pyridine glued on a glass fibre to establish whether this transformation occurs from a single crystal of **13**·pyridine to a single crystal of **13**(ex.DMF). The crystal was heated to 90°C and heated at a rate of 0.5°C per minute to 120°C. While there was a steady decrease in the intensity of the reflections for **13**·pyridine, individual reflections consistent with a single crystal of **13**(ex.DMF) were not observed, but rather, there was the development of the powder pattern for **13**(ex.DMF). Interestingly, throughout this transformation the crystal morphology did not appear to change significantly, but the final diffraction pattern was clearly that of a powder. It is likely that the transformation (which must begin at the surface of the crystal) results in fragmentation of daughter crystals of the non-solvate, thus eroding away at the mother crystal.

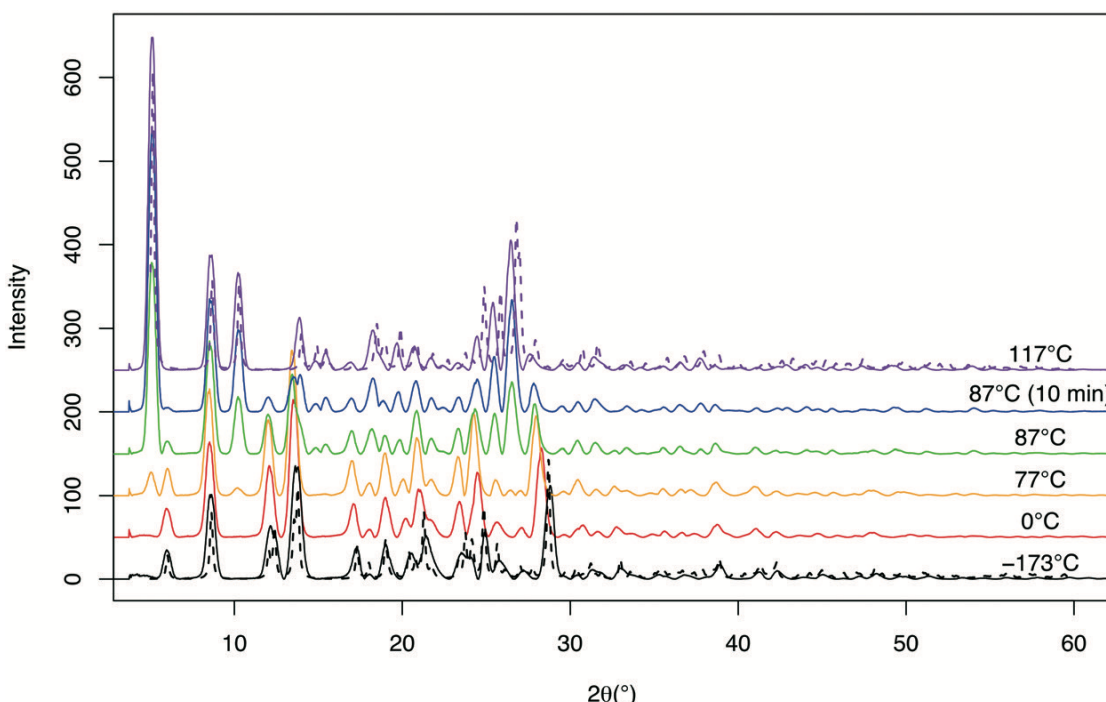


FIGURE 8.11: Variable temperature powder XRD patterns from **13**·pyridine, calculated powder pattern for **13**·pyridine and **13**(ex.DMF) are the dotted lines in the top and bottom traces respectively.

We believe that a single crystal to single crystal transformation is very unlikely as collapsing of the channels containing the pyridine solvate would prevent complete desolvation. A plausible mechanism for this interconversion likely involves replacement of the  $\text{N} \cdots \text{Se}$  chalcogen bond in **13**·pyridine, with a  $\text{O} \cdots \text{Se}$  chalcogen bond involving the isoselenazolinone carbonyl group from a molecule in an adjacent layer which is at a distance of  $12.051 \text{ \AA}$  (??).

## 8.4 Conclusion

The structure of **13**·pyridine is characterised by planar sheets of the benzisoselenazolinone **13** pierced by channels of pyridine molecules at an angle  $133^\circ$ , the pyridine molecules are held in place by  $\text{N} \cdots \text{Se}$  chalcogen bonding to the isoselenazolinone moiety. These channels which extend through the structure to the surface of the crystal provide a means for escape of pyridine from the lattice when the crystal is heated to ca.  $100^\circ\text{C}$ . Upon loss of the pyridine from these channels the remaining molecules undergo rearrangement to fill the space and in doing so the  $\text{N} \cdots \text{Se}$  chalcogen bond in **13**·pyridine is replaced by a  $\text{C}=\text{O} \cdots \text{Se}$  chalcogen bond to give the non solvate **13**(ex.DMF). The geometry of the chalcogen bond requires that the two benzisoselenazolinone ring systems which are essentially coplanar in **13**·pyridine twist by an angle of  $138^\circ$  resulting in the formation of highly corrugated sheets in the non solvate.

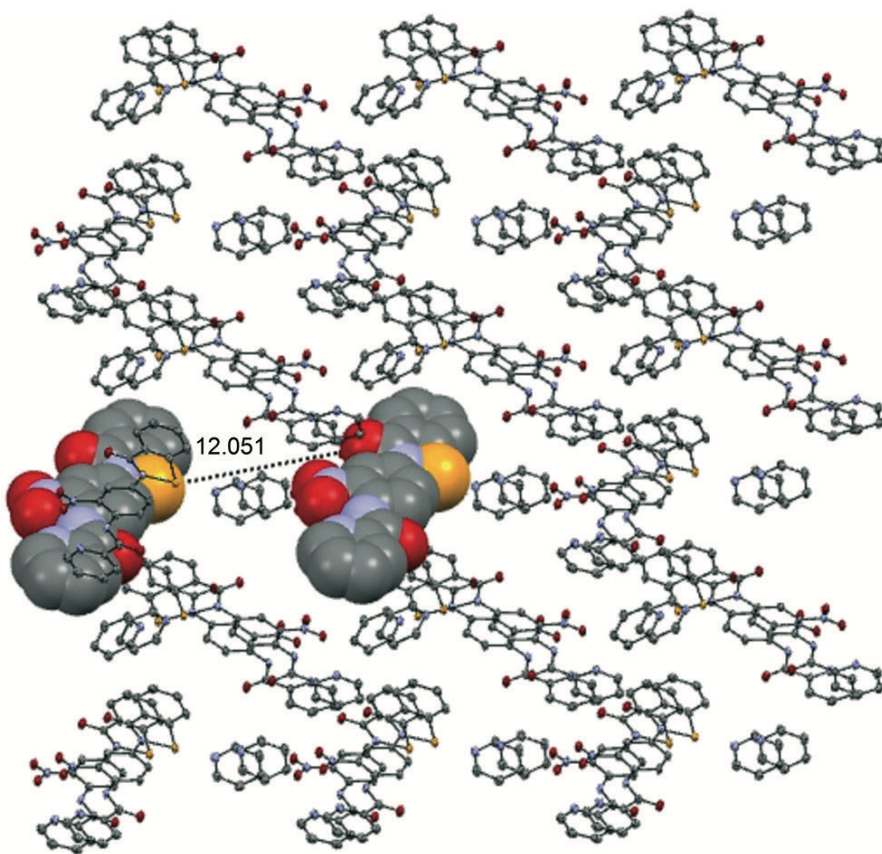


FIGURE 8.12: Interlayer benzisoselenazolinones **13** believed to form a  $\text{O} \cdots \text{Se}$  chalcogen bond upon desolvation of **13**-pyridine.

## 8.5 Experimental

### 8.5.1 Synthesis

#### 8.5.1.1 Preparation of 2-(4-amino-3-nitrophenyl)benzo[*d*][1,2]-selenazol-3(2*H*)-one **15**.

Diselenide **5** (1.2025 g, 3.005 mmol) was dissolved in thionyl chloride (20 mL) and refluxed for 30 min, and the colour changed from purple to light yellow. Excess thionyl chloride was removed *in vacuo*, and the residue dissolved in anhydrous THF (50 mL). To this was added a solution of 2-nitro-1,4-phenylenediamine (991.9 mg, 6.477 mmol) and triethylamine (dist. from  $\text{CaH}_2$ , 3 mL) in anhydrous THF (50 mL). This mixture was stirred at room temperature for 18 h, then filtered, washing the precipitate with water, to afford 2-(4-amino-3-nitrophenyl)benzo[*d*][1,2]-selenazol-3(2*H*)-one **15** as a brick red solid (940 mg, 61%, m.p. 300.8–302.0°C (DMF)).

$^1\text{H}$  NMR (400 MHz,  $d_6$ -DMSO)  $\delta$  ppm 7.08 (d,  $J = 9.00$  Hz, 1 H), 7.46 (t,  $J = 7.43$  Hz, 1 H), 7.55 (s, 2 H), 7.59–7.70 (m, 2 H), 7.86 (d,  $J = 7.43$  Hz, 1 H), 8.06 (d,  $J = 7.83$  Hz, 1 H), 8.12 (d,  $J = 1.96$  Hz, 1 H).

<sup>13</sup>C NMR (100 MHz, *d*<sub>6</sub>-DMSO) δ ppm 120.29, 121.49, 126.32, 126.71, 127.77, 128.31, 128.45, 129.68, 132.66, 134.13, 139.33, 145.03, 165.70.

MS (ESI +ve) m/z 335.9882 (MH<sup>+</sup>) C<sub>13</sub>H<sub>10</sub>N<sub>3</sub>O<sub>3</sub>Se<sup>+</sup> requires 335.9881 (Δ=0.3 ppm).

### 8.5.1.2 Preparation of N-(2-nitro-4-(3-oxobenzo[*d*][1,2]selenazol-2(3*H*)-yl)phenyl) picolinamide **13**.

Picolinic acid (256.6 mg, 2.084 mmol) was dissolved in anhydrous THF (5 mL) and triethylamine (dist. from CaH<sub>2</sub>, 1 mL), then trichlorobenzoylchloride (325 μL) was added and the mixture stirred for 10 min. The above nitroaniline **15** (242.8 mg, 0.956 mmol) was then added, and the mixture stirred under argon for 24 h, during which time the dark red colour faded to give a yellow solution. The mixture was tipped into water (100 mL) and filtered to afford a yellow precipitate, which was recrystallised from pyridine (50 mL) to give N-(2-nitro-4-(3-oxobenzo[*d*][1,2]selenazol-2(3*H*)-yl)phenyl)picolinamide **13** as yellow needles (93.2 mg, 20%), m.p. 342.7–343.7°C (*d*). While recrystallization by slow evaporation from DMF gave small yellow needles m.p. 342–344°C (*d*).

<sup>1</sup>H NMR (500 MHz, *d*<sub>6</sub>-DMSO) δ ppm 7.51 (t, *J* = 7.40 Hz, 1 H) 7.66–7.83 (m, 1 H) 7.94 (d, *J* = 7.63 Hz, 1 H) 8.04 (dd, *J* = 7.8, 2.4 Hz, 1 H) 8.09–8.17 (m, 2 H) 8.23 (d, *J* = 7.78 Hz, 1 H) 8.68 (d, *J* = 2.44 Hz, 1 H) 8.73 (d, *J* = 9.00 Hz, 1 H) 8.81 (d, *J* = 4.43 Hz, 1 H) 12.22 (s, 1 H).

MS (ESI +ve) m/z 441.010 (MH<sup>+</sup>) C<sub>19</sub>H<sub>13</sub>N<sub>4</sub>O<sub>4</sub>Se<sup>+</sup> requires 441.0096 (Δ=0.9 ppm).

## 8.5.2 Crystallography

Intensity data for **13**·pyridine was collected on a Rigaku XtalLAB Synergy at 100.0(1) K. Data for **13**(ex.DMF) was collected on the MX1 beamline<sup>Cowieson2015</sup> at the Australian Synchrotron. The temperature was maintained using an Oxford Cryostream cooling device. The structures were solved by direct methods and difference Fourier synthesis.<sup>Sheldrick2015</sup> Thermal ellipsoid plots were generated using the program Mercury<sup>Macrae2008</sup> integrated within the WINGX<sup>Farrugia1999</sup> suite of programs. Other figures were obtained with both Mercury software and Crystal Maker software.

### 8.5.2.1 Crystal data for **13**(ex.DMF)

C<sub>19</sub>H<sub>12</sub>N<sub>4</sub>O<sub>4</sub>Se, *M* = 439.29, *T* = 100.0 K, *λ* = 0.82656 Å, orthorhombic, space group Pbca, *a* = 12.652(3), *b* = 7.5250(15), *c* = 34.367(7) Å, *V* = 3272.0(11) Å<sup>3</sup>, *Z* = 8, *D<sub>c</sub>* = 1.784 mg M<sup>-3</sup>, *μ* = 3.383 mm<sup>-1</sup>, *F*(000) = 1760, crystal size 0.05 × 0.005 × 0.005 mm<sup>3</sup>, 35758 reflections measured,

$\theta_{\max} = 32.28^\circ$ , 3282 independent reflections [ $R(\text{int}) = 0.0803$ ], the final  $R$  was 0.0601 [ $I > 2\sigma(I)$ , 2513 reflections] and  $wR(F^2)$  was 0.1802 (all data), GOF 1.037.

### 8.5.2.2 Crystal data for 13·pyridine

$C_{19}H_{12}N_4O_4Se \cdot C_5H_5N$ ,  $M = 518.39$ ,  $T = 100.0$  K,  $\lambda = 1.54184$  Å, monoclinic, space group  $Pc$ ,  $a = 4.9726(2)$ ,  $b = 14.6836(5)$ ,  $c = 14.4255(5)$  Å,  $\beta = 98.154(4)^\circ$ ,  $V = 1042.64(7)$  Å<sup>3</sup>,  $Z = 2$ ,  $D_c = 1.651$  mg M<sup>-3</sup>,  $\mu(\text{Cu-K}\alpha) = 2.829$  mm<sup>-1</sup>,  $F(000) = 524$ , crystal size  $0.12 \times 0.033 \times 0.026$  mm<sup>3</sup>, 6794 reflections measured,  $\theta_{\max} = 76.79^\circ$ , 3132 independent reflections [ $R(\text{int}) = 0.0558$ ], the final  $R$  was 0.0422 [ $I > 2\sigma(I)$ , 2977 data] and  $wR(F^2)$  was 0.1107 (all data), GOF 1.098.

## 8.6 Acknowledgements

We gratefully acknowledge Sirtex Medical for funding and the Australian Synchrotron for beamtime via the Collaborative Access Program (proposal 13618b). The Australian Research Council for Post Graduate Scholarships (TF and MPVK).

## Chapter 9

# Engineering supramolecular networks using Ch-bonding

We prepared a 3-pyridyl ebselen derivative **1l** in the hope that it would form a one-dimensional network consisting of linear Ch-bonded chains, and we were pleased to find that this was indeed the case.

In the crystal packing of **1l**, each molecule is Ch-bonded through the pyridyl nitrogen to an adjacent molecule generated by the *n*-glide, with a Se...N distance of 2.386(1) Å. There is an additional Ch-bond to the carbonyl oxygen of the molecule generated by the *n*-glide plus a translation along the *a* axis (??). The Se...O distance is 3.336(1) Å. The bond angles in both cases are consistent with a Ch-bonding interaction, with the nitrogen and oxygen atoms sitting almost perfectly opposite to the electron withdrawing group (174.43(5)° and 165.89(4)° respectively.) The *sp*<sup>2</sup> lone pairs of the nitrogen and oxygen atoms are also well aligned, at angles of 120.60(9)° and 113.93(9)° respectively.

We have previously reported an instance of H-bond assisted Ch-bonding, in which a H-bond to the carbonyl of ebselen strengthens the resulting Ch-bond. We were interested to see if the introduction of a full positive charge in the molecule would have a similar effect, by analogy with charge-assisted H- and X-bonding. We therefore alkylated **1l** using methyl iodide to form **1m**, and were pleased to see yellow needles form in the reaction mixture almost immediately upon cooling. The structure of these crystals is shown in ?? . The pyridyl nitrogen is alkylated as expected, and the charge is balanced by the iodide Ch-bonded to the selenium, at a distance of 2.9904(4) Å and an angle of 178.7(1)° to the antipodal nitrogen.

In order to assess the effect of the positive charge on the Ch-bond, we required a system which lacked the charge on the ebselen molecule. We attempted to co-crystallise **1l** with a

variety of halide salts, but none gave the desired co-crystal. This is not entirely unsurprising, as most cations would not be easily incorporated in the lattice, disfavouring the formation of a co-crystal. However, when **11** was heated in aqueous HCl, then slowly cooled, crystals of **16** precipitated out of the solution (??). The product **16** corresponds to an extreme case of charge assisted Ch-bonding, where the endocyclic Se–N bond is formally broken, and a new bond is established with the Ch-bond donor. We propose a mechanism for this transformation which involves protonation of the carbonyl oxygen by the strong acid, followed by nucleophilic attack by chloride at the selenium. The product then tautomerises to the more stable amide form, and an intramolecular Ch-bond is re-established, thus stabilising the selenyl chloride (??). The stability of this selenyl chloride is remarkable, as it is resistant to hydrolysis and oxidation, and may be kept in air for several weeks.

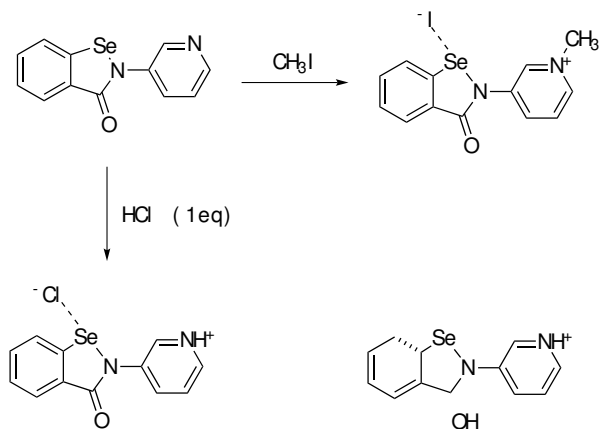


FIGURE 9.1: Reactions of 3-pyridyl ebselen **1??**.

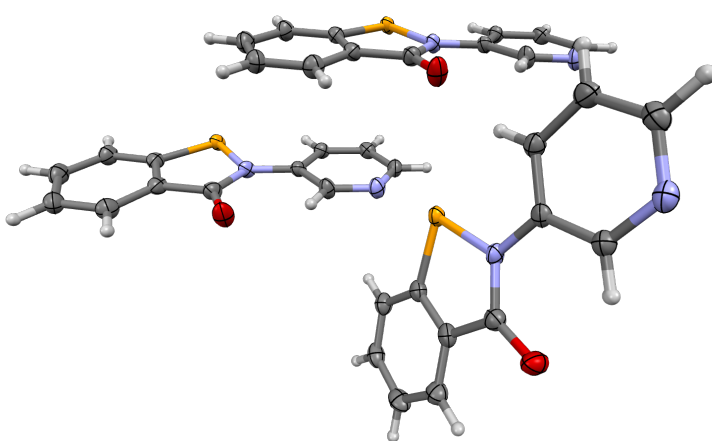


FIGURE 9.2: Ch-bonds formed by 3-pyridyl ebselen **1??** in the crystal packing. The stronger of the two is defined by the N–Se…N<sub>pyr</sub> angle, and the weaker is defined by the C–Se…O angle.

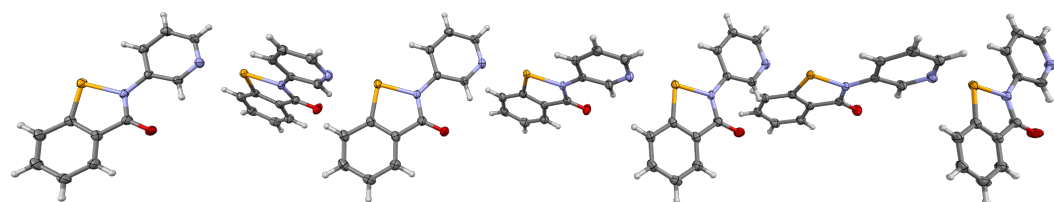


FIGURE 9.3: One-dimensional network formed by the strong N–Se...N Ch-bonds. This is extended into 3 dimensions by the weaker C–Se...O Ch-bonds, and  $\pi$ -stacking.

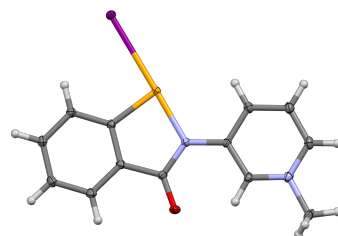


FIGURE 9.4: Structure of the methylated derivative **1??**.

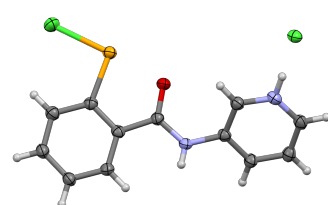


FIGURE 9.5: Structure of the ring opened hydrochloride derivative **16**.



# **Chapter 10**

## **Development of a Ch-bonding DNA binder**

### **10.1 Introduction**

#### **10.1.1 Mechanism of radioprotection**

The mechanism by which bis-benzimidazoles impart radioprotection is believed to be a proton coupled electron transfer from the bound ligand to the damaged DNA.[???] This was elucidated from a structure-activity relationship study, where it was observed that the acidity of the 1' proton was strongly correlated with radioprotective ability.

Ebselen itself, of course, displays antioxidant properties too. These are believed to be the basis for its neuroprotective, anti-helmenthic, and anti-inflammatory behaviour.[???] The mechanism, however, appears to be completely different. Ebselen behaves as a glutathione peroxidase mimic, that is to say, a catalyst that increases the rate at which glutathione reduces reactive oxygen species.



SCHEME 10.1: Synthesis of benzisoselenazolone-benzimidazole Hoechst analogue **20**.



SCHEME 10.2: Synthesis of bis-benzisoselenazolone Hoechst analogue **24**.

## 10.2 *In silico* modelling

## 10.3 Synthesis of analogues

## 10.4 DNA binding studies

## 10.5 Conclusions

## 10.6 Experimental procedures

### 10.6.1 Synthetic methods

Selenium was purified by refluxing in 32% hydrochloric acid for 2 h, then washing with methanol and ether.

#### 10.6.1.1 Preparation of N-(2-amino-5-nitrophenyl)benzamide 17

4-Nitro-1,2-benzenediamine (3.0797 g, 20.110 mmol) and TEA (3 mL, distilled from CaH<sub>2</sub>) were dissolved in anhydrous THF (150 mL). Benzoyl chloride (1.5 mL, 1.8 g, 13 mmol) was then added at -10°C and the mixture slowly warmed to room temperature while stirring for 18 h. The mixture was then tipped into water (400 mL), and extracted with ethyl acetate (3 × 100 mL). The combined organic layers were washed with water (2 × 200 mL), brine (200 mL), then dried (MgSO<sub>4</sub>) and evaporated to give a reddish solid. This was recrystallised from ethyl acetate to give the amide **17** as yellow crystals (2.5027 g, 75%).

#### 10.6.1.2 Preparation of 6-nitro-2-phenyl-1*H*-benzo[*d*]imidazole 18

Amide **17** (1.2283 g, 4.7749 mmol) was refluxed in a solution of BF<sub>3</sub> · OEt<sub>2</sub> (0.75 mL) and dioxane (75 mL) for 1.5 h. The mixture was then cooled to room temperature, stirred for 18 h, then heated to reflux again for 2 h. The yellow solution was diluted with water (300 mL) and extracted with ethyl acetate (3 × 75 mL). The combined organic layers were washed with water and brine (100 mL each), then dried (Na<sub>2</sub>SO<sub>4</sub>), and evaporated to give a brown oil. Trituration with petroleum spirit/dichloromethane afforded **18** as a light brown friable solid (1.0606 g, 93%).

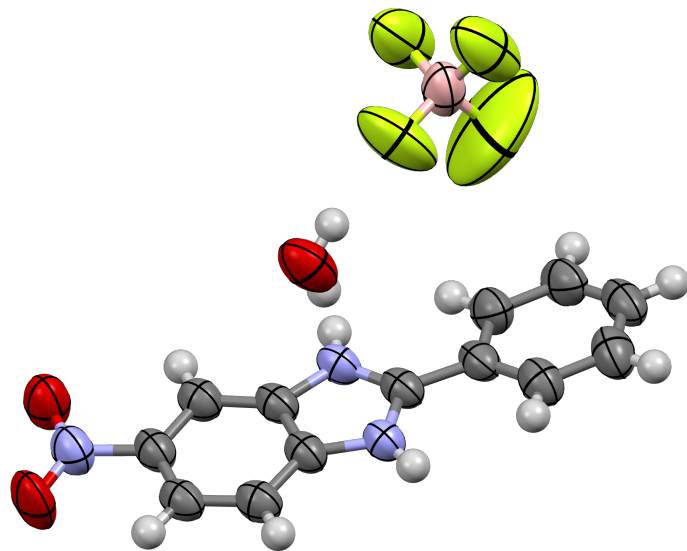


FIGURE 10.1: X-ray crystal structure of **18** as the tetrafluoroborate salt.

#### 10.6.1.3 Preparation of 2-phenyl-1*H*-benzo[*d*]imidazol-6-amine **19**

A solution of the nitrobenzene **18** (893.6 mg, 3.735 mmol) and tin (II) chloride dihydrate (4.410 g, 19.54 mmol) in concentrated hydrochloric acid (20 mL) was refluxed for 2 h. The solution was then cooled, and basified to pH 10 using 5 M aqueous sodium hydroxide. This was then extracted with ethyl acetate (2 × 30 mL), washing with water and brine (30 mL each). The combined organic layers were dried (Na<sub>2</sub>SO<sub>4</sub>) then evaporated to give **19** as a brownish solid (677.2 mg, 87%).

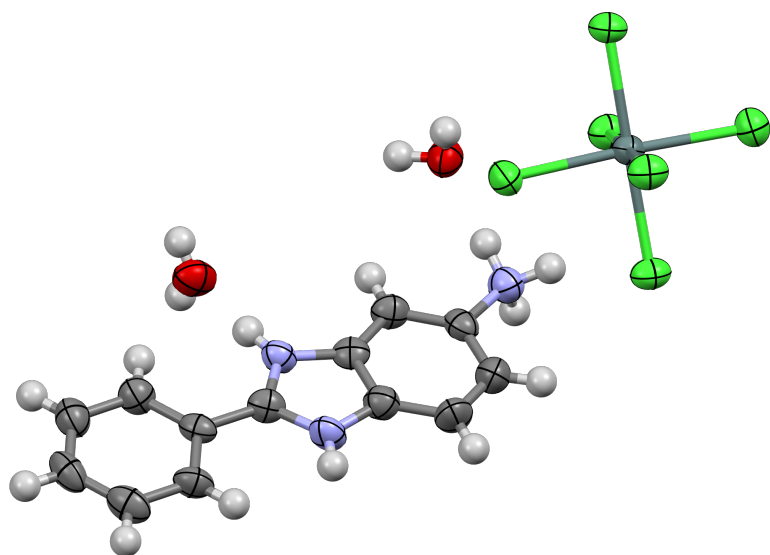


FIGURE 10.2: X-ray crystal structure of **19** as the hexachlorostannate salt.

#### 10.6.1.4 Preparation of 2-(2-phenyl-1*H*-benzo[*d*]imidazol-6-yl)benzo[*d*][1,2]selenazol-3(2*H*)-one **20**

Diselenide **5** (440.1 mg, 1.100 mmol) was refluxed in thionyl chloride with 2 drops DMF for 2 h. The excess reagent was removed by vacuum distillation, and the residue was dissolved in anhydrous acetonitrile (10 mL). This was added dropwise to a solution of the aniline **19** (440.4 mg, 2.105 mmol) and TEA (2 mL) in a further 10 mL anhydrous acetonitrile. The mixture was stirred at room temperature for 18 h, then briefly brought to reflux. It was then cooled, diluted with water (30 mL) and extracted into ethyl acetate ( $3 \times 50$  mL). The combined organic layers were washed with water and brine (50 mL each), then dried ( $\text{MgSO}_4$ ), then evaporated onto celite. This was chromatographed on a SNAP 25 g silica cartridge using an ethyl acetate/methanol gradient, affording 2 major fractions:

1. orange solid, 67.7 mg, 8%, **20**
2. yellow solid, 166.0 mg, 38%, starting material **19**

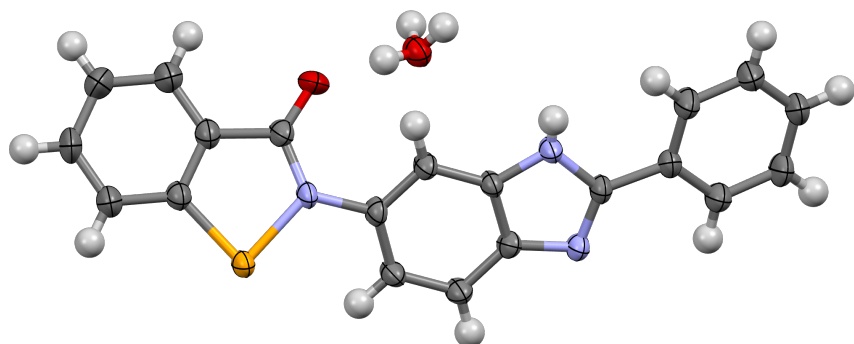


FIGURE 10.3: X-ray crystal structure of **20**. The water is disordered over 3 sites, with each proton having an occupancy of 2/3.

#### 10.6.1.5 Preparation of 2-chloro-4-nitro-N-phenylbenzamide **21**

2-Chloro-4-nitrobenzoic acid (10.3144 g, 51.173 mmol) was refluxed in thionyl chloride (20 mL) with 3 drops DMF for 2 h. The excess reagent was then removed by vacuum distillation and the residue was dissolved in anhydrous DCM (100 mL). This was added slowly to a solution of aniline (4.756 g, 51.07 mmol) and TEA (10 mL, distilled from  $\text{CaH}_2$ ) in a further 100 mL of

anhydrous DCM. The mixture was stirred for 18 h at room temperature, then the solvent was removed *in vacuo*. The residue was washed with water ( $3 \times 50$  mL), then recrystallised from ethanol to afford **21** as colourless plates (10.5134 g, 75%).

$^1\text{H}$  NMR (500 MHz,  $\text{CDCl}_3$ )  $\delta$  ppm 7.23 (t,  $J=7.48$  Hz, 1 H), 7.42 (t,  $J=7.78$  Hz, 2 H), 7.64 (d,  $J=7.93$  Hz, 2 H), 7.81 (br. s., 1 H), 7.93 (d,  $J=8.39$  Hz, 1 H), 8.24 (d,  $J=8.39$  Hz, 1 H), 8.35 (d,  $J=1.07$  Hz, 1 H).

#### 10.6.1.6 Preparation of 6-nitro-2-phenylbenzo[*d*][1,2]selenazol-3(2*H*)-one **22**

Copper (I) iodide (127.2 mg, 0.6679 mmol) and 1,10-phenanthroline (121.5 mg, 0.6743 mmol) were dissolved in anhydrous DMF (4 mL). To this was added selenium (1035.1 mg, 13.109 mmol) and potassium carbonate (755.9 mg, 5.469 mmol), and the mixture heated to 120°C under a nitrogen atmosphere for 5 min. The mixture was then cooled, the amide **21** (968.4 mg, 3.500 mmol) added, and the mixture was again heated at 120°C under nitrogen for 18 h. Upon cooling, the mixture was tipped into brine (200 mL) and stirred in the air for 3 h, then extracted into ethyl acetate ( $4 \times 50$  mL). The combined organic phases were washed with water then brine (100 mL each), then dried ( $\text{MgSO}_4$ ) and evaporated to give a dark orange solid. This was redissolved in ethanol (70 mL) and cooled to –20°C for 72 h, affording **22** as an orange precipitate, which was filtered and dried (119.1 mg, 11%, m.p. 256.2–258.2°C (dec.)). The mother liquor was loaded onto silica and chromatographed using a SNAP 50 g silica cartridge, affording 3 major fractions which were not further characterised.

$^1\text{H}$  NMR (400 MHz,  $d_6$ -DMSO)  $\delta$  ppm .

$^{13}\text{C}$  NMR (100 MHz,  $d_6$ -DMSO)  $\delta$  ppm .

$^{77}\text{Se}$  NMR (0 MHz,  $d_6$ -DMSO)  $\delta$  ppm .

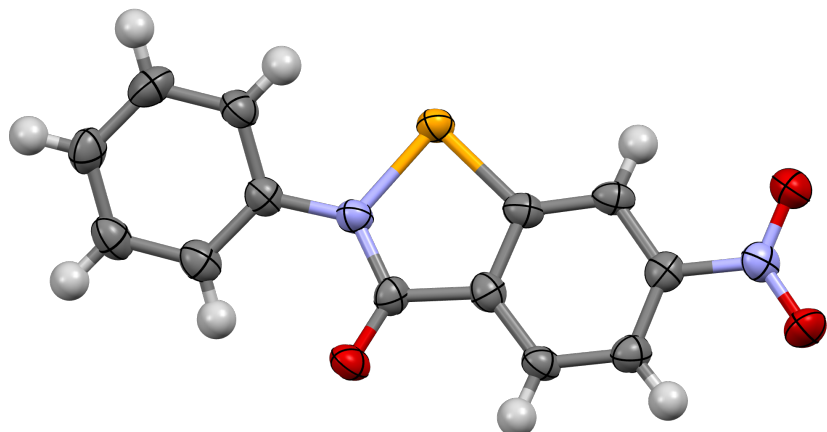
MS (ESI +ve) m/z 320.97720 ( $\text{MH}^+$ )  $\text{C}_{13}\text{H}_9\text{N}_2\text{O}_3\text{Se}^+$  requires 320.97729 ( $\Delta=-0.09$  mmu).

#### 10.6.1.7 Preparation of benzisoselenazolinone ??

Aqueous ammonia (30%, 637  $\mu\text{L}$ , 10 mmol) was dissolved in acetonitrile (5 mL), cooled to 0 ° C, and to this was added a solution of the selenyl chloride **6** (5 mmol) in a further 10 mL anhydrous acetonitrile. The mixture was stirred at room temperature for 30 minutes, then the solvent evaporated *in vacuo*, and the resulting solid washed with water (5 mL) to afford benzisoselenazolinone **25** as an off white solid (858.4 mg, 87%, m.p. XXX–XXX).

$^1\text{H}$  NMR (400 MHz,  $d_6$ -DMSO)  $\delta$  ppm .

$^{13}\text{C}$  NMR (100 MHz,  $d_6$ -DMSO)  $\delta$  ppm .

FIGURE 10.4: X-ray crystal structure of **22**.

$^{77}\text{Se}$  NMR (0 MHz,  $d_6$ -DMSO)  $\delta$  ppm .

MS (ESI +ve) m/z XXX ( $\text{MH}^+$ ) XXXX<sup>+</sup> requires XXXX ( $\Delta=0$  ppm).

#### 10.6.1.8 Preparation of 2-(4-amino-3-nitrophenyl)benzo[*d*][1,2]selenazol-3(2*H*)-one ??

Diselenide **5** (1.2025 g, 3.005 mmol) was dissolved in thionyl chloride (20 mL) and refluxed for 30 minutes, and the colour changed from purple to light yellow. Excess thionyl chloride was removed *in vacuo*, and the residue dissolved in anhydrous THF (50 mL). To this was added a solution of 2-nitro-1,4-phenylenediamine (991.9 mg, 6.477 mmol) and triethylamine (3 mL, dist. from  $\text{CaH}_2$ ) in anhydrous THF (50 mL). This mixture was stirred at room temperature for 18 h, then filtered, washing the precipitate with water, to afford 2-(4-amino-3-nitrophenyl)benzo[*d*][1,2]selenazol-3(2*H*)-one **26** as a brick red solid (940 mg, 61%, m.p. (DMF) 300.8–302.0 °C).

$^1\text{H}$  NMR (400 MHz,  $d_6$ -DMSO)  $\delta$  ppm 7.08 (d,  $J=9.00$  Hz, 1 H), 7.46 (t,  $J=7.43$  Hz, 1 H), 7.55 (s, 2 H), 7.59–7.70 (m, 2 H), 7.86 (d,  $J=7.43$  Hz, 1 H), 8.06 (d,  $J=7.83$  Hz, 1 H), 8.12 (d,  $J=1.96$  Hz, 1 H).

$^{13}\text{C}$  NMR (100 MHz,  $d_6$ -DMSO)  $\delta$  ppm 120.29 (s), 121.49 (s), 126.32 (s), 126.71 (s), 127.77 (s), 128.31 (s), 128.45 (s), 129.68 (s), 132.66 (s), 134.13 (s), 139.33 (s), 145.03 (s), 165.70 (s).

MS (ESI +ve) m/z 335.9882 ( $\text{MH}^+$ )  $\text{C}_{13}\text{H}_{10}\text{N}_3\text{O}_3\text{Se}^+$  requires 335.9881 ( $\Delta=0.298$  ppm).

### 10.6.1.9 Preparation of *N*-(2-nitro-4-(3-oxobenzo[*d*][1,2]selenazol-2(3*H*)-yl)phenyl)picolinamide ??

Picolinic acid (256.6 mg, 2.084 mmol) was dissolved in anhydrous THF (5 mL) and triethylamine (1 mL, dist. from CaH<sub>2</sub>), then trichlorobenzoyl chloride (325 uL) was added and the mixture stirred for 10 minutes. The nitroaniline **26** (242.8 mg, 0.956 mmol) was then added, and the mixture stirred under argon for 24 h, during which time the dark red colour faded to give a yellow solution. The mixture was tipped into water (100 mL) and filtered to afford a yellow precipitate, which was recrystallised from pyridine (50 mL) to give 2-(4-amino-3-nitrophenyl)benzo[*d*][1,2]selenazol-3(*H*)-one **27** as a yellow solid (93.2 mg, 20%, m.p. 342.7–343.7 ° C).

<sup>1</sup>H NMR (500 MHz, *d*<sub>6</sub>-DMSO) δ ppm 7.51 (t, *J*=7.40 Hz, 1 H) 7.66–7.83 (m, 1 H) 7.94 (d, *J*=7.63 Hz, 1 H) 8.04 (dd, *J*=9.00, 2.40 Hz, 1 H) 8.09–8.17 (m, 2 H) 8.23 (d, *J*=7.78 Hz, 1 H) 8.68 (d, *J*=2.44 Hz, 1 H) 8.73 (d, *J*=9.00 Hz, 1 H) 8.81 (d, *J*=4.43 Hz, 1 H) 12.22 (s, 1 H)

MS (ESI +ve) m/z 441.0100 (MH<sup>+</sup>) C<sub>19</sub>H<sub>13</sub>N<sub>4</sub>O<sub>4</sub>Se<sup>+</sup> requires 441.0096 (Δ=0.907 ppm).

### 10.6.1.10 Preparation of 2-iodobenzoic anhydride ??

2-Iodobenzoic acid (1.9957 g, 8.045 mmol) and DCC (0.8457 g, 4.098 mmol) were stirred in anhydrous diethyl ether (10 mL) for 18 h. The white precipitate was filtered off, washing with cold anhydrous ether (2×10 mL). The filtrate was concentrated *in vacuo* to afford 2-iodobenzoic anhydride **28** as an off-white solid (1.9623 g, 100%).

### 10.6.1.11 Preparation of *N*-(3,4-dinitrophenyl)-2-iodobenzamide ??<sup>Shivani2007</sup>

A neat mixture 2-iodobenzoic anhydride **28** (1.9226 g, 4.022 mmol), 3,4-dinitroaniline (0.7290 g, 3.981 mmol) and zinc iodide (0.2140 g, 0.673 mmol) was stirred at 80 ° C under an argon atmosphere. The melt was cooled to room temperature, dissolved in diethyl ether (40 mL), and the solution washed with 1 M HCl (20 mL), 0.8 M sodium bicarbonate solution (50 mL), then brine (50 mL). The organic phase was dried (MgSO<sub>4</sub>), then evaporated to afford a yellow oil. This was triturated with petroleum ether (5 mL) with a few drops of dichloromethane to afford *N*-(3,4-dinitrophenyl)-2-iodobenzamide **29** as an off white solid (0.926 g, 56%, m.p. XXX–XXX).

<sup>1</sup>H NMR (400 MHz, *d*<sub>6</sub>-DMSO) δ ppm 7.28 (td, *J*=7.20, 1.96 Hz, 1 H), 7.48–7.61 (m, 2 H), 7.97 (d, *J*=7.83 Hz, 1 H), 8.07 (dd, *J*=8.80, 1.37 Hz, 1 H), 8.30 (d, *J*=8.61 Hz, 1 H), 8.47 (d, *J*=1.17 Hz, 1 H), 11.40 (s, 1 H).

<sup>13</sup>C NMR (100 MHz, *d*<sub>6</sub>-DMSO) δ ppm 93.91 (s), 115.06 (s), 122.90 (s), 127.96 (s), 128.72 (s), 128.76 (s), 132.28 (s), 136.30 (s), 139.69 (s), 142.03 (s), 144.21 (s), 144.76 (s), 168.92 (s).

MS (ESI +ve) m/z ??? ( $\text{MH}^+$ )  $\text{C}_{13}\text{H}_9\text{IN}_3\text{O}_5^+$  requires 413.9581 ( $\Delta=0$  ppm).

**10.6.1.12 Preparation of 6-bromo-2-phenyl-1*H*-benzo[*d*]imidazole**

